Interrogating the Electronic Structure and Photochemistry of Molecules with Transient X-ray Absorption Spectroscopy

Benjamin Evert Van Kuiken

A dissertation
submitted in partial fulfillment of the
requirements for the degree of

Doctor of Philosophy

University of Washington

2014

Reading Committee:

Munira Khalil, Chair

Xiaosong Li

David J. Masiello

Program Authorized to Offer Degree:

Chemistry

University of Washington

Abstract

Interrogating the Electronic Structure and Photochemistry of Molecules with Transient X-ray Absorption Spectroscopy

Benjamin Evert Van Kuiken

Chair of Supervisory Committee:
Assistant Professor Munira Khalil
Chemistry Department

A detailed understanding of photochemical processes in molecules and materials is necessary for understanding natural phenomena and engineering new technologies. In this thesis, light-induced changes in spin states, rearrangements of electron densities, and proton transfer events are considered. X-ray absorption (XA) spectroscopy is used to investigate the electronic structure of molecules in electronic ground and excited states to reveal fundamental insights on the nature of photochemical events.

The photoinduced Fe^{II} spin crossover (SCO) reaction is investigated theoretically. Following photoexcitation, an Fe^{II} SCO molecule undergoes a conversion from a singlet ground state to a quintet excited state. Transition-potential density functional theory and time-dependent density functional theory (TDDFT) are used to simulate the transient Fe K-edge XA spectra. The spectral signature each spin state is identified in the near-edge and pre-edge regions of the XA spectra.

Ruthenium L-edge spectroscopy is used to investigate the electronic structure and photochemistry of solar cell dye molecules and transition metal mixed-valence complexes. The metal-to-ligand charge transfer (MLCT) chemistry is studied in the widely used "N3" dye ($[Ru(dcbpy)_2(NCS)_2]$) molecule. Ru L-edge XA spectroscopy shows that the formation of the MLCT state corresponds to a light-induced oxidation of the Ru atom from Ru^{II} to Ru^{III}. Moreover, charge transfer features in the show the important role of the NCS^- ligands in the photochemistry of N3. TDDFT is used to simulate Ru L_3-edge spectra of N3 and other Ru complexes. This validates its use as a predictive tool for simulating Ru L_3-edge spectroscopy. Finally, the Ru L_3-edge spectra of the mixed-valence metal complexes $[(NC)_5Fe^{II}CNRu^{III}(NH_3)_5]^-$ and $[(NC)_5Ru^{II}CNRu^{III}(NH_3)_5]^-$. Quantum chemical simulation using explicit water molecules are required to reproduce experimental spectra highlighting the role of the hydrogen bonding solvent in determining the properties of these complexes.

Finally, the photochemistry of 2-thiopyridine (2TP) is investigated. 2TP exists in solution in equilibrium with its tautomer 2-mercaptopyridine (2MP). The possibility of excited state proton transfer from 2TP to 2MP is considered. The transient S K-edge XA spectra are measured for 2TP in acetonitrile. The time-dependence of the transient absorption signal shows that multiple photoproducts are formed. This establishes transient S K-edge XA spectroscopy as a power for tool for studying photochemistry in organic and biological systems.

Table of Contents

References………………………………………………………………………….. 139

Chapter 5: Photochemistry of 2-Thiopyridine from Transient Sulfur K-edge X-ray Absorption Spectroscopy………………………………………………... 141

5.1 Introduction………………………………………………………………. 141

5.2 Methods…………………………………………………………………. 142

5.3 Results and Discussion……………………………………………………... 144

5.4 Summary,,,,,,,,,,,,,,,,,,,,…………………………………………………………… 147

References………………………………………………………………………. 149

List of Figures

List of Tables

GLOSSARY

DFT: Density functional theory

UV: Ultraviolet

VIS: Visible

MLCT: Metal-to-ligand charge transfer

XA: X-ray absorption

N3: cis-Bis(isothiocyanato)bis(2,2'-bipyridyl-4,4'-dicarboxylato)ruthenium(II)

TDDFT: Time-dependent density functional theory

TPDFT: Transition-potential density functional theory

GGA: Generalized gradient approximation

SCO: Spin cross-over

XANES: X-ray absorption near-edge structure

EXAFS: Extended X-ray absorption fine structure

LS: Low-spin

HS: High-spin

HSA: High-spin analogue

CT: Charge transfer

XC: Exchange—Correlation

2TP: 2-Thiopyridine

2MP: 2-Mercaptopyridine

ACN: Acetonitrile

ALS: Advanced Light Source

Acknowledgements

There is a long list of scientific mentors, teachers, friends and family that I am deeply indebted to as I complete my doctoral dissertation. I'm not really sure where to start when it comes to thanking people, so I'm going with the most obvious choice: Munira! Munira has been my advisor for the last six years, but with all the trust she has put in me, I've always felt like she was my collaborator as well. She put a lot of trust in me with all of the theoretical and computational work that I did during graduate school, and she trusted me to be the project lead on a bunch of beamtime experiments which tends to be the realm of postdocs. As a result, I feel a great deal of ownership over the work I've done in graduate school, and I feel that that I'm leaving UW as an independent scientist. I don't think I could have possibly had a better graduate school education.

In addition to Munira, I've been fortunate to have excellent mentors on the theoretical side of my work. While they aren't my official advisors, I learned a great deal from my interactions with Niri Govind, Xiaosong Li, and David Masiello. I spent a great summer in a horribly boring place to work with Niri. I learned a lot from him, and he has been a mentor, friend, and collaborator ever since. When I'm at UW, there are two doors on the third floor that are always open to me. Xiaosong and David have made me part of the theory community in the chemistry department. Xiaosong has involved me in research projects, and David has given his time teaching tutorials on various topics. I am indebted to them for these enriching interactions.

The UW chemistry department has a great community of graduate students that have enriched my scientific experience and made it hard for me to want to leave. I've had a great time working with the members of the Khalil group. I want to thank Mike and Matt for all help they have given me at the ALS. I also want to thank all the members of the theory suite. You have really made the department home for me the last few years.

I've got to thank all my beamtime pals. X-ray spectroscopy can be an exhausting endeavor. At beamline 6 the shifts run from 4 a.m. to 4 p.m. or vice versa. Actually having a successful beamtime typically means that you're working a lot more than those twelve hours, and you certainly aren't doing all that alone. I was very fortunate to work with a wonderful group of graduate students and postdocs from Bob Schoenlein's lab at LBNL. Hana Cho and Matt Strader are at the top of this list. They were present for each of my beamtimes, and they were great to work with even when we were stuck up all night doing miserable tasks like finding the one wire-guided jet that works. I also have to thank Nils who has always been a wonderful collaborator with whom I'm always excited to discuss science. In recent experiments I've also had the pleasure of working with Amy and Jae Hyuk. I was not expert in X-ray spectroscopy when I started going to ALS, and these experiments would never have been possible if it weren't for this fine group of people.

I would like to acknowledge some of the scientists and teachers that got me here. I had an excellent undergraduate research experience. I did an R.E.U. at Hope College where I work with Nicole Brinkmann and Bill Pollack. This introduced me to Linux and quantum chemistry, and I started building the skill set that I utilized so much in grad school. At University of Michigan, I worked with Barry Dunietz who introduced me doing science at a very high level. It was the research experience in his group that really prepared me for graduate level projects. Finally, I must thank John Dersch without whom I would never have been anywhere near science. I started college at GRCC in Grand Rapids. John Dersch taught calculus. It was the only class that challenged me. It was the class that made me actually do homework. It was the class that inspired me to take other science courses. At one point John asked me, "why is a foreign

language major, taking all these math classes?" I didn't have a good answer for him, so I applied to engineering school.

DEDICATION

to Evert and Doris

Chapter 1

Introduction

1.1 Molecular Photochemistry

Light energy is harvested by matter in in a broad range of photochemical processes. The most ubiquitous example of such a process is the conversion of light energy to chemical energy by photosynthesis.[1] While the complete photosynthetic process involves many individual chemical transformations, the cycle is initiated by the absorption of a photon by the magnesium porphyrin molecule called chlorophyll. Absorption of a photon generates an excited state and provides the energy required to oxidize a chlorophyll molecule initiating the next steps of photosynthesis. Similarly, the generation electrical energy by a dye sensitized solar cell begins with the absorption of a photon by a dye molecule which injects an electron into a nearby semiconductor.[2,3] Consequently, a complete understanding of these phenomena requires a detailed understanding of the underlying molecular photochemistry. This understanding involves being able to answer questions about how the atoms and electrons in a molecule rearrange themselves following a photochemical event. Obtaining this information requires having access to experimental tools that sensitive to the motions of atoms and electrons on ultrafast (100 fs - 10 ns) timescales. Moreover, these experiments must be complemented by interpretations derived from rigorous and predictive theoretical models. The goal of this thesis is to show how a detailed understanding of molecular photochemistry may be obtained from transient X-ray spectroscopy.

An example of a common photocycle found in organic and inorganic molecules is pictured in Figure 1.1a. Absorption of visible light causes a transition from a singlet ground state

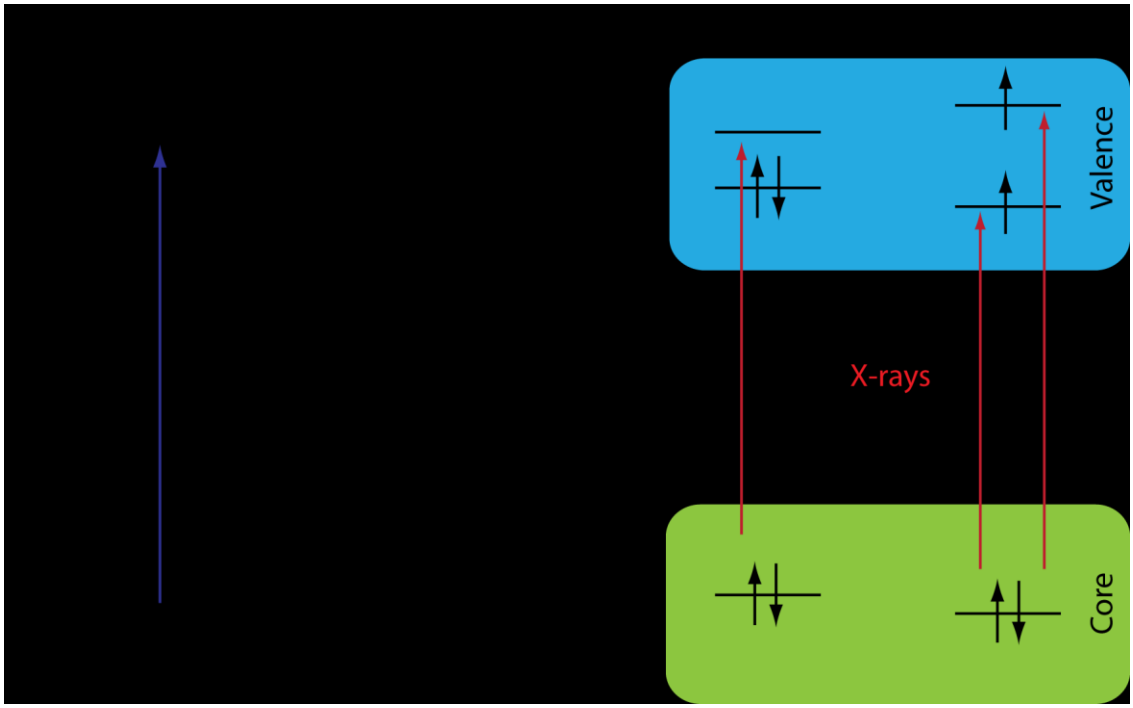

Figure 1.1. (a) An example a common photocycle for an organic or inorganic molecule exhibiting a long-lived state (T_1) that is populated by intersystem crossing. The initial excited state (S_1) decays on timescale (< 100 fs) that is difficult to access by experimental means while the triplet state may be probed by a range of ultrafast spectroscopies. (b) The energetics of the core and valence orbitals are affected by transition from the S_0 ground state to the T_1 excited state. X-ray spectroscopy may be used to probe the changes in the character and energetics of these orbitals.

(S_0) to a bright singlet excited state (S_1). This state is typically short lived, and it decays to the ground state or a long-lived excited state. In this example, there is a fast (~100 fs) intersystem crossing (ISC) event leading to the formation of a triplet state. In many cases the photochemistry is reversible, and the system will relax to the ground state via phosphorescence or non-radiative processes. However, this triplet state typically has a nanosecond lifetime. Understanding the photophysics of such a system requires an knowledge of the properties of the states involved and the timescales upon which they interconvert. Ultrafast spectroscopy provides the ideal set of tools for understanding these dynamics. In particular, this work makes use of transient X-ray Absorption (XA) spectroscopy where a visible laser is used to initiate some photochemical event

and X-rays are used to probe the nonequilibrium states created by laser excitation.[4-8] This technique provides time resolution of ~70 ps, which allows for comparison of the S_0 and T_1 state in Figure 1.1a. One way to think about the changes in the molecule is to consider how electronic levels shift as a result of the conversion from S_0 to T_1. Figure 1.1b shows a possible rearrangement of core and valence electronic levels and the electronic configuration that accompanies the $S_1 \rightarrow T_1$ conversion. X-ray spectroscopy is sensitive to this rearrangement because it makes use of the core electrons of molecules to probe the unoccupied valence orbitals. This work shows how the rearrangement of electrons and atoms after photoexcitation is encoded in the transient XA spectra.

In this thesis I examine several systems that exhibit the photochemistry that may be described by diagrams akin to what is pictured in Figure 1.1a. First the photoinduced spin crossover reaction taking place in an Fe(II) molecule is examined.[9,10] Upon excitation of a metal-to-ligand charge transfer (MLCT) transition, this Fe complex is converted from its singlet ground state to a quintet excited state. The change in spin state is accompanied by a large geometric distortion as the metal—ligand bond lengths dilate by ~0.2 Å. Secondly, I consider the characteristics of the intramolecular CT in a Ru solar cell dye molecule, cis-Bis(isothiocyanato)bis(2,2'-bipyridyl-4,4'-dicarboxylato)ruthenium(II) termed N3. Upon excitation a long-lived ^{3}MLCT state is formed in which the Ru(II) ground state has been photo-oxidized to Ru(III). Lastly, photochemistry of 2-thiopyridine (2TP) is studied. Photoexcitation of (2TP) leads to the formation of a triplet state. However, the excited state of 2TP is a reactive species and previous studies have reported the that that excited state proton transfer may take place in this system leading to the formation of 2-mercaptopyridine (2MP). For each of these

systems it is shown that the XA spectroscopy provides a detailed picture of the photochemistry that may be tied to predictive theoretical models based in quantum chemistry.

1.2 X-ray Absorption Spectroscopy

For molecular systems the most commonly used electronic spectroscopies involve excitations of valence electrons by radiation in or near the visible region of the electromagnetic spectrum. X-ray spectroscopy differentiates itself from other spectroscopic techniques because it is concerned with the excitations of the core electrons of atoms. While a broad range of X-ray techniques exist including absorption, emission, and photoelectron spectroscopies, each technique takes advantage of the atomic specificity of core electronic levels. The core electrons of atoms in molecules reside in orbitals that are only weakly perturbed by the surrounding chemical environment. Consequently, excitations of particular core electrons occur at

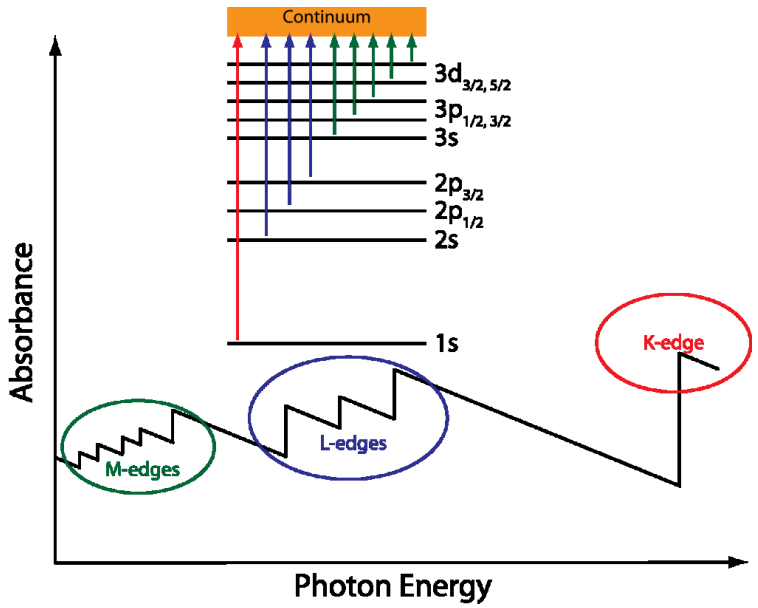

Figure 1.2. Schematic core level spectrum of an atom showing individual "edges" arising from excitations of different core orbitals.

characteristic energies. For example, the binding energies of the 1s electrons of O, S, and Fe are 543.1, 2472, and 7112 eV, respectively.[11] This energy specificity imparts X-ray spectra with an atomic selectivity. Consequently, spectra may be collected that report on the local electronic and geometric structure around the absorbing atom.

This work focuses on XA spectroscopy in which an X-ray photon excites a core electron to a final state that may be a bound valence orbital or a continuum state above the ionization potential.[12,13] Figure 1.2 shows a schematic of a XA spectrum for a typical transition metal atom where there is a spectral feature corresponding to excitations for each core electron. For each core orbital there is a unique spectral feature referred to as an "edge." The edges are denoted K, $L_{1/2/3}$, $M_{1/2/3/4/5}$, etc. labeling excitations of core electrons with increasing principle quantum number. Multiple edges also arise from core electrons with different angular momentum quantum numbers. The L_1, L_2, and L_3 edges correspond to excitations out of the 2s, $2p_{1/2}$, and $2p_{3/2}$ orbitals, respectively. The chemical information that is contained in each edge is governed by the nature of the atomic and valence orbitals of the surrounding atom. Due to the atomic nature of X-ray absorption spectroscopy, the transitions at each edge are given by the standard selection rule of atomic spectroscopy ($\Delta l = \pm 1$). Consequently, the K-edge of a 3d transition metal is dominated by 1s → 4p transitions, but the L_2 and L_3-edges consist of transitions from the 2p orbitals to the unoccupied 3d orbitals.

It is often useful to discuss the XA spectra by considering the different energy regions of a spectrum. Figure 1.3 shows a cartoon of a typical K-edge XA spectrum for a 3d metal such as iron. The spectrum is divided into regions that contain unique molecular information. The first 40-70 eV of the XA spectrum beginning with the absorption edge is referred to as the X-ray absorption near edge structure (XANES). This region of the spectrum contains features arising

from multiple varieties of core-excited states. First, the pre-edge region has been highlighted. This feature arises from quadrupole allowed transitions from the 1s orbital to unoccupied 3d orbitals. This region is sensitive to the ligand field environment, spin state, and oxidation number of the metal atom. The remainder of the XANES region (at and above the absorption edge) is dominated by dipole allowed transitions that measure the unoccupied p-projected density of states. This includes transitions to unoccupied bound states as well as low-lying state in the continuum. XANES spectroscopy contains information about the oxidation state of the central ion and its coordination environment. Finally, the XA spectrum exhibits oscillations at energies high above the absorption edge. This region of the spectrum is called the extended X-ray absorption fine structure (EXAFS). These oscillations in the EXAFS spectrum can be viewed as the interference pattern generated by a photoelectron scattering off atoms surrounding the absorbing atom. Fourier analysis of this region may be used to extract bond distances between the absorbing atom and the surrounding coordination shells.

The XANES region is the focus of this thesis. In particular, the XANES region of the Ru

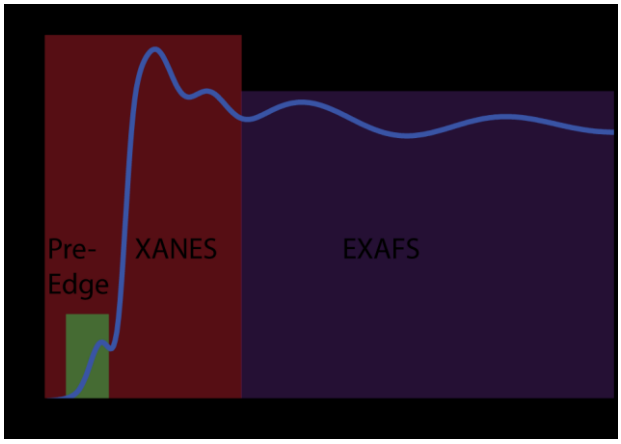

Figure 2.1 Cartoon of a metal K-edge XA spectrum showing the different regions of the XA spectrum. The region within 40-70 eV of the absorption edge is referred to as the XANES region and reports on the electronic properties of the metal. The EXAFS region extends hundreds of eV above the edge.

L_2- and L_3-edges contains detailed information about the electronic structure of Ru complexes. These edges consist of 2p → 4d dipole allowed transitions that report directly on the local electronic structure and metal—ligand bonding in Ru complexes. The L_3 and L_2 edges are located at ~2830 eV and ~2960 eV, respectively. The 130 eV splitting between these features corresponds to the spin—orbit splitting dividing the $2p_{3/2}$ and $2p_{1/2}$ orbitals. For L-edge spectra involving spin—orbit coupling (SOC), the Δl selection rule introduced above is replaced by a $\Delta j = 0, \pm 1$ selection rule. In octahedral symmetry, transitions at the L_3-edge are allowed from the $2p_{3/2}$ orbital to the $4d_{5/2}$ and $4d_{3/2}$, while only $2p_{1/2} \rightarrow 4d_{3/2}$ transitions are allowed at the L_2-edge. For this reason, a broader range of valence states are accessed by Ru L_3-edge XA spectroscopy. By directly accessing the 4d orbitals, this spectroscopy is sensitive to the oxidation state, spin configuration, and ligand field strength in Ru complexes. Additionally, L-edge spectra contain features arising from metal—ligand covalency that are termed charge transfer peaks. The intensity of these features reports directly on the degree of metal—ligand interaction. These properties make this spectroscopy an ideal probe of the photochemistry Ru solar cell dyes.

This work employs transient XA spectroscopy for studying excited state electronic and molecular structure. This novel technique combines X-ray radiation generated by a synchrotron or X-ray free-electron laser (XFEL) with visible or ultraviolet light from an ultrafast laser system. The optical excitation from the laser system is used to initiate a photochemical event, while the X-rays are used to probe the sample. The X-ray and laser systems are synchronized so that the time delay between laser and X-ray pulses may be controlled to investigate excited state dynamics. Experimental data is presented as differences spectra. A differences spectrum shows the change in XA absorbance resulting from laser excitation. Consequently, the excited state XA spectrum for a molecular system is encoded in this spectrum. The experiments presented in this

thesis were performed at the Ultrafast Hard X-ray Beamline (6.0.1) at the Advanced Light Source (ALS) at Lawrence Berkeley National Laboratory. This facility provides X-ray pulses with a time resolution of 70 ps, which allows for the investigation of dynamics on timescales hundreds of picoseconds to tens of nanoseconds. This provides ample time resolution for characterizing long-lived excited states.

1.3 Simulating X-ray Absorption Spectroscopy

The interpretation of XA spectroscopy is reliant upon simulating experimentally measured spectra. The interaction of matter with X-rays may be described by the Golden Rule.[13] The transition probability between an initial state Φ_i and a final state Φ_f is given by

$$W_{fi} = \frac{2\pi}{\hbar}\left|\langle\Phi_f|\hat{T}|\Phi_i\rangle\right|^2 \delta(E_f - E_i - \hbar\omega).$$

$\hat{T}$ is the transition operator, and the δ-function provides the resonance condition for X-rays with incident energy $\hbar\omega$. Examination of the transition operator shows that the dominant contribution to X-ray spectra is given by the electric dipole operator ($\hat{r}$). As discussed above, electric quadrupole transitions are relevant to some spectra, and this is discussed in detail in Chapter 2. There have been numerous techniques developed in the fields of chemistry and physics for the simulation of XA spectra. The most commonly utilized approaches are multiple scattering techniques,[14,15] semi-empirical calculations based on the ligand field theory,[13,16,17] and calculations that make use of quantum chemical tools such as density functional theory (DFT).[18-23] Each of these methods has an ideal range of applicability. For example, multiple scattering approaches are used extensively to analyze EXAFS spectra. While theoretically rigorous, implementations typically employ simple model potentials that lack the chemical detail required to accurately reproduce near-edge features that depend on specific orbital occupations.

Consequently, it is desirable to employ predictive theoretical tools that can be directly related to quantum chemical techniques used to characterize molecular electronic structure.

In this thesis quantum chemical methods have been used extensively. For X-ray spectra, these methods may be divided into two categories. The first category is where a single-particle approximation has been made, and Koopman-style excitations are used to describe the XA spectrum.[12,24] In this approximation, the excitation energies are given by the orbital energy differences between the core orbital of interest and each orbital of the virtual space. A more rigorous approach is based in time-dependent DFT (TDDFT) where the linear-response formalism of this theory may be used to compute core-level excitations.[18,19,22,25] These are two predictive techniques that have been successful in computing XA spectra for a many systems.

1.4 Thesis Outline

The work collected here in this thesis establishes suitability of XA spectroscopy to probe molecular photochemistry in a range of chemical systems. Chapter 2 presents a comparative study of methods based on DFT for simulating the transient XA spectra of an Fe(II) spin crossover complex. The XANES region of the spectrum is simulated with single-particle approximations, and the pre-edge region is modeled with TDDFT. Both approaches are shown to accurately reproduce experimental spectra. While previous studies had employed multiple scattering methods that used model potentials, this study connects spectra with theoretical models that contain more chemical detail. Chapter 3 establishes the validity of simulating Ru L_3-edge XA spectroscopy with TDDFT. XA spectra are calculated for a series of Ru(II) and Ru(III) compounds, and the simulated spectra are shown to be in excellent agreement with experiment. The importance of simulation parameters such as the choice of exchange--correlation functional

is discussed. Finally, the Ru L-edge spectra of the mixed-valence metal complexes $[(CN)_5FeCNRu(NH_3)_5]^{1-}$ and $[(CN)_5RuCNRu(NH_3)_5]^{1-}$ are investigated. It is shown that DFT simulations employing explicit water molecules are required to reproduce the experimentally determined valencies on these molecules. This highlights the role of that the hydrogen bonding environment in has on the electronic structure of these molecules. In Chapter 4 the results of transient Ru L-edge XA experiments on the N3 solar cell dye molecule are presented. The XA spectrum is monitored following the excitation of the MLCT band that results in the photooxidation of the Ru center. This study tracks the rearrangement of electron density in this molecule following photoexcitation, and it highlights the important role of the NCS ligands in the photochemistry of N3. Finally, Chapter 5 presents some preliminary results on the transient S K-edge X-ray spectroscopy of 2-Thiopyridine (2TP). Photoexcitation of 2TP lead to the formation of a triplet state within the 70 ps time resolution of the experiment. Formation of an addition photoproduct is observed on a ~400 ps timescale. The possibility of excited state proton transfer in this complex is discussed.

References

(1) Voet, D.; Voet, J. G. *Biochemistry*; John Wiley & Sons: Hoboken, NJ, 2004.

(2) Nazeeruddin, M. K.; Gratzel, M.; Kalyanasundaram, K.; Girling, R. B.; Hester, R. E. *J. Chem. Soc., Dalton Trans.* **1993**, 323.

(3) Grätzel, M. *Acc. Chem. Res.* **2009**, *42*, 1788.

(4) Saes, M.; Bressler, C.; Abela, R.; Grolimund, D.; Johnson, S. L.; Heimann, P. A.; Chergui, M. *Phys. Rev. Lett.* **2003**, *90*, 047403/1.

(5) Bressler, C.; Chergui, M. *Chem Rev* **2004**, *104*, 1781.

(6) Bressler, C.; Chergui, M. *Actual. Chim.* **2008**, *317*, 59.

(7) Bressler, C.; Chergui, M. *Annu. Rev. Phys. Chem.* **2010**, *61*, 263.

(8) Chen, L. X. *Annu. Rev. Phys. Chem.* **2005**, *56*, 221.

(9) Khalil, M.; Marcus, M. A.; Smeigh, A. L.; McCusker, J. K.; Chong, H. H. W.; Schoenlein, R. W. *J. Phys. Chem. A* **2006**, *110*, 38.

(10) Bressler, C.; Milne, C.; Pham, V. T.; ElNahhas, A.; van der Veen, R. M.; Gawelda, W.; Johnson, S.; Beaud, P.; Grolimund, D.; Kaiser, M.; Borca, C. N.; Ingold, G.; Abela, R.; Chergui, M. *Science* **2009**, *323*, 489.

(11) Thompson, A. C.; Attwood, D. T.; Gullikson, E. M.; Howells, M. R.; Kortright, J. B.; Robinson, A. L.; Underwood, J. H.; Kim, K.; Kirz, J.; Lindau, I.; Pianetta, P.; Winick, H.; Williams, G. P.; Schofield, J. H. *X-ray Data Booklet*; Lawrence Berkeley National Lab: Berkeley, CA, 2001.

(12) Stöhr, J. *NEXAFS Spectroscopy*; Springer: Berlin, 2003.

(13) de Groot, F.; Kotani, A. *Core Level Spectroscopy of Solids*; CRC Press: Boca Raton, 2008.

(14) Ankudinov, A. L.; Ravel, B.; Rehr, J. J.; Conradson, S. D. *Phys. Rev. B* **1998**, *58*, 7565.

(15) Benfatto, M.; Congiu-Castellano, A.; Daniele, A.; Della Longa, S. *J. Synchrotron Radiat.* **2001**, *8*, 267.

(16) de Groot, F. M. F. *Coord. Chem. Rev.* **2005**, *249*, 31.

(17) Stavitski, E.; de Groot, F. M. F. *Micron* **2010**, *41*, 687.

(18) DeBeer George, S.; Petrenko, T.; Neese, F. *J. Phys. Chem. A* **2008**, *112*, 12936.

(19) DeBeer George, S.; Petrenko, T.; Neese, F. *Inorg. Chim. Acta* **2008**, *361*, 965.

(20) Van Kuiken, B. E.; Khalil, M. *J. Phys. Chem. A* **2011**, *115*, 10749.

(21) Lopata, K.; Van Kuiken, B. E.; Khalil, M.; Govind, N. *J. Chem. Theory Comput.* **2012**.

(22) Van Kuiken, B. E.; Valiev, M.; Daifuku, S. L.; Bannan, C.; Strader, M. L.; Cho, H.; Huse, N.; Schoenlein, R. W.; Govind, N.; Khalil, M. *J. Phys. Chem. A* **2013**, *117*, 4444.

(23) Campbell, L.; Mukamel, S. *J. Chem. Phys.* **2004**, *121*, 12323.

(24) Triguero, L.; Pettersson, L. G. M.; Ågren, H. *Phys. Rev. B* **1998**, *58*, 8097.

(25) Lopata, K.; Van Kuiken, B. E.; Khalil, M.; Govind, N. *J. Chem. Theory Comput.* **2012**, *8*, 3284.

Chapter 2

Simulating Picosecond Iron K-edge X-ray Absorption Spectra by *Ab Initio* Methods to Study Photoinduced Changes in the Electronic Structure of Fe(II) Spin Crossover Complexes

The work presented in this chapter has been previously published in the following article:

Van Kuiken, B. E.; Khalil, M. "Simulating Picosecond Iron K-edge X-ray Absorption Spectra by *Ab Initio* Methods to Study Photoinduced Changes in the Electronic Structure of Fe(II) Spin Crossover Complexes," *J. Phys. Chem. A* **2011**, *115*, 10749.

Recent time-resolved X-ray absorption experiments probing the low-spin to high-spin photo conversion in Fe(II) complexes have monitored the complex interplay between electronic and structural degrees of freedom on an ultrafast timescale. In this study, we use transition potential (TP) and time-dependent (TD) DFT to simulate the picosecond time-resolved iron K-edge X-ray absorption spectrum of the spin crossover (SCO) complex, $[Fe(tren(py)_3)]^{2+}$. This is achieved by simulating the X-ray absorption spectrum of $[Fe(tren(py)_3)]^{2+}$ in its low-spin (LS), $^1A_1$, ground state and its high-spin (HS), $^5T_2$, excited state. These results are compared with the X-ray absorption spectrum of the high spin analogue (HSA), $[Fe(tren(6\text{-}Me\text{-}py)_3)]^{2+}$, which has a $^5T_2$ ground state. We show that the TPDFT methodology can simulate a 40 eV range of the iron K-edge XANES spectrum reproducing all of the major features observed in the static and transient spectra of the LS, HS, and HSA complexes. The pre-edge region of the K-edge spectrum,

simulated by TDDFT, is shown to be highly sensitive to metal-ligand bonding. Changes in the intensity of the pre-edge region are shown to be sensitive to both symmetry and π-backbonding by analysis of relative electric dipole and quadrupole contributions to the transition moments. We generate a spectroscopic map of the iron 3d orbitals from our TDDFT results and determine ligand field splitting energies of 1.55 and 1.35 eV for the HS and HSA complexes, respectively. We investigate the use of different functionals finding that hybrid functionals (such as PBE0) produce the best results. Finally, we provide a detailed comparison of our results with theoretical methods that have been previously used to interpret Fe K-edge spectroscopy of equilibrium and time-resolved SCO complexes.

2.1 Introduction

An important objective in studies of ultrafast photochemical reactions in the condensed phase is to understand in detail the coupling of electronic and nuclear motion following the absorption of a photon in the system of interest. The ultrafast photochemistry of transition metal complexes is of particular interest for studying how structural and vibrational relaxation on electronic excited states affects charge transfer and separation. This is crucial for developing materials and devices for converting solar energy into chemical, electrical or mechanical energy. Femtosecond UV, optical and IR spectroscopies has been used successfully to probe photoinduced charge transfer processes in transition metal complexes.[1] With the advent of intense, short-pulse, table-top and synchrotron X-ray sources, the methods of ultrafast spectroscopy for studying transition metal complexes in solution have been extended to the X-ray regime with pico- to femtosecond time resolution.[2-5] Transient X-ray absorption spectroscopy is developing as a powerful tool for probing changes in the molecular and electronic structure surrounding the transition metal atom

of interest in disordered media following optical/UV excitation.[6-10] Ultrafast transient X-ray absorption experiments have revealed information about metal-to-ligand charge transfer (MLCT) in transition metals systems, excited state bond strengthening in dinuclear transition metal systems, axial ligand dynamics in metalloporphyrins and electronic and structural changes associated with the photoinduced spin cross-over (SCO) in Fe(II) complexes.[11-27]

In this study, we use *ab initio* methods to simulate the picosecond K-edge transient X-ray absorption spectra of an Fe(II) complex undergoing photoinduced SCO as reported by Khalil *et al.* in Reference 17. We use transition-potential DFT (TPDFT) to simulate the near-edge spectral features of the X-ray absorption spectrum at the Fe K-edge and time-dependent DFT (TDDFT) to simulate the pre-edge spectral features of the SCO complexes. Various spectral regions of the Fe K-edge of SCO complexes have been previously calculated using real-space multiple scattering codes, atomic multiplet codes and a DFT based method.[12,17,28-30] This study is motivated by the desire to use molecular-orbital (MO) based approaches to interpret transient X-ray absorption spectra. We focus on assessing the ability of the simulations to reproduce the observed spectral changes at the Fe K-edge using two different DFT based approaches.

The Fe K-edge X-ray absorption spectrum consists of excitations from Fe 1s orbitals to unoccupied bound states and continuum states. The K-edge spectrum consists of the XANES (X-ray absorption near edge structure) spectral region, spanning −10eV to 50 eV relative to the edge jump and the EXAFS (extended X-ray absorption fine structure) spectral region at energies ~30 – 500 eV higher than the edge jump.[31] The XANES region includes the pre-edge region containing electric quadrupole allowed 1s $\rightarrow$ 3d transitions, which report on the iron-ligand bonding interactions and coordination geometry. The EXAFS oscillations encode information about the molecular structure in terms of bond lengths and bond angles between the iron atom

and its coordination shells. In this study we will focus on simulating the XANES spectra of Fe(II) spin crossover complexes.

The SCO phenomenon is widely studied for its importance in understanding basic spin physics and for potential applications in building optical switching and memory devices.[32] Typically, it refers to a reaction in which a transition metal complex goes from a low- to high-spin configuration induced by changes in temperature, pressure, or the absorption of light. In octahedral Fe(II) systems, the photoinduced SCO reaction involves interconversion between a $^1A_1$ low-spin and $^5T_2$ high-spin state on a sub-picosecond timescale. The dynamics of the SCO process following photoexcitation have been probed using optical, IR and X-ray fields in several different Fe(II) complexes and it continues to be a rich field of experimental and theoretical study.[11,12,15-17,30,33-40]

In this study we employ TP- and TDDFT to model and study the spectral changes associated with the photoinduced spin crossover at the Fe K-edge at ~7.1 keV in the low-spin (LS) Fe(II) complex, $[Fe(tren(py)_3)](PF_6)_2$ as reported in Reference 17. Upon excitation of the metal-to-ligand charge-transfer (MLCT) transition with a 400 nm femtosecond pulse, the molecule undergoes a transition to the transient high-spin (HS) $^5T_2$ state on a timescale of sub–300 fs.[33,38] Transient X-ray absorption spectra obtained at 330 ps following MLCT excitation measured an increase in Fe–N bond length by 0.21 Å in the photoexcited HS complex. In the experimental study the transient X-ray spectrum was compared to the static X-ray spectrum of a high-spin analogue (HSA) complex, $[Fe(tren(6\text{-}Me\text{-}py)_3)](PF_6)_2$. We simulate the XANES region of the Fe K-edge X-ray absorption spectrum using TP-DFT and pre-edge region using TDDFT for the LS, HS and HSA cationic complexes. The X-ray absorption spectrum for the transient HS complex is simulated by optimizing the structure of the lowest quintet state of $[Fe(tren(py)_3)](PF_6)_2$. We

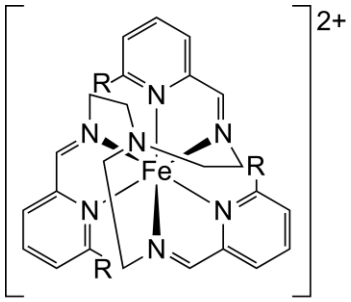

Figure 2.1 The chemical structure of the cation in $[Fe(tren(py)_3)](PF_6)_2$ where $(tren(py)_3 \equiv$ tris(N-(2-pyridylmethyl)-2-iminoethyl)-amine). This compound has a low-spin (LS) ground state. The addition of the methyl groups ($R=CH_3$) results in the analogous high-spin compound (HSA), $[Fe(tren(6\text{-}Me\text{-}py)_3)](PF_6)_2$ in the electronic ground state at room temperature.

find that the TP-DFT methodology can simulate a 40 eV range of the iron K-edge XANES spectrum reproducing all of the major features observed in the static and transient spectra of the LS, HS, and HSA complexes. The pre-edge region of the X-ray absorption simulated by TDDFT provides a spectroscopic map of the iron 3d orbitals. We show how changes in the intensity of the pre-edge spectral features are sensitive to both the molecular symmetry and π-backbonding around the Fe atom by analysis of relative electric dipole and quadrupole contributions to the transition moments. Finally, we provide a detailed comparison of these results with theoretical methods that have been previously used to interpret equilibrium and time-resolved XAS of Fe(II) SCO complexes.

2.2 Computational Methods

The structures of the LS, HS, and HSA cationic complexes were optimized using the PBE0 functional and the 6-31G(d,p) valence double zeta basis set with polarization functions.[41-43] Previous studies have shown that PBE0 gives accurate predictions of bond lengths in SCO complexes.[44,45] Frequencies were calculated and verified to be real to confirm that each

optimized structure corresponded to a minimum on its potential energy surface. The HS structure is the lowest energy quintet state of the $[Fe(tren(py)_3)]^{2+}$ complex and corresponds to the transient HS structure.[17] All structure optimization calculations were performed using a polarizable continuum model to simulate the effects of the acetonitrile solvent (ε=35.69) using the Gaussian 09 suite of quantum chemistry programs.[46,47]

We utilized the TPDFT method to simulate the Fe K-edge X-ray absorption spectra of the LS, HS and HSA complexes as implemented in the StoBe-deMon package.[48,49] This method is based on Slater's transition-state approach for calculating transition energies for excitations between single particle orbitals.[50] In Slater's method, transition energies between two states are given by the difference in orbital eigenvalues for a state optimized with both hole and particle orbitals having an occupation number equal to 0.5. The idea of this approach is to calculate excitation energies from a reference state that balances the ground and excited state character. The TPDFT approach is an approximation to Slater's transition-state method that is valid for calculating X-ray absorption spectra. TPDFT assumes that the major perturbation to the electron density comes from the absence of an electron in the core orbital, while the presence of an electron in a valence, Rydberg, or continuum state creates only a small perturbation to the electron density. Therefore, the half electron in the excited state can be neglected, and one can obtain an entire X-ray absorption spectrum from the single optimization of an electronic state with the occupation number of the core orbital set to 0.5.

All TPDFT calculations were performed at the level of the generalized gradient approximation (GGA) using the BP86 exchange-correlation functional.[51,52] The iron atom was described by the Wachter's basis set,[53] the nitrogen and carbon atoms were described using a (7111/411/1) basis set and the hydrogen atoms were described by the (41/1*) basis set from the

deMon library. In the StoBe-deMon package, the charge density is expanded in an auxiliary basis, and the Coulomb and exchange-correlation contributions to the energy are evaluated in this auxiliary basis to speed up the calculations. We used an A2 type auxiliary basis set generated internally from the orbital basis sets. One of the advantages of the TPDFT approach for calculating X-ray absorption spectra is that a large number of excited states can be calculated from a single converged wave function. To take advantage of this feature, the basis set is augmented after wave function convergence with a large diffuse basis set so that Rydberg states and continuum states can be accurately modeled in a finite basis set.[54] We have investigated several different augmentation basis sets and will discuss them in detail in the next section.

The pre-edge region of the X-ray absorption spectra at the Fe K-edge for the LS, HS and HSA complexes were also calculated using the linear response formulation of time-dependent DFT (TDDFT) utilizing the Tamm-Dancoff approximation within the ORCA quantum chemistry package.[55] The approach for treating core excitations follows the protocol developed in recent publications.[56,57] In most implementations of TDDFT, one would have to solve a prohibitively large eigenvalue equation because all lower energy excitations would have to be calculated prior to the core excitations. To circumvent this problem, we only allow excitations from the iron 1s orbitals to calculate Fe K-edge spectra. This approximation is justified because the large energetic separation between the iron core and the other electronic levels means that excitations from the iron 1s orbital will not couple to excitations from other orbitals.

The TDDFT calculations are preformed using two different density functionals. The first is the GGA BP86 functional used in the TPDFT calculations, and the second is the hybrid PBE0 functional used for structure optimization. In the TDDFT calculations, we use basis sets that have previously given good agreement with experimental X-ray absorption spectra of Fe

complexes. For hydrogen, carbon and nitrogen atoms, we employ the def2-TZVP basis of Ahlrichs and coworkers.[58] The iron atom is described by the CP(PPP) basis set devised by Neese for the accurate description of core properties.[59] We also use the RIJ and RIJCOSX approximations for TDDFT calculations with the BP86 and PBE0 functionals, respectively.[60] Within the TDDFT framework, we assessed the effect of the solvent using a conductor-like screening model (COSMO),[61] and we saw no changes with the PBE0 functional and insignificant changes with the BP86 functional. In this paper we focus on the gas phase results from our calculations.

An accurate calculation of the Fe K-edge X-ray absorption includes contributions from the electric dipole, electric quadrupole and magnetic moments of the molecule interacting with the X-ray field. When the wavelength of the perturbing electromagnetic field is much larger than the dimension of the molecule, the long-wavelength or electric dipole approximation holds and only the calculation of the electric dipole moment is necessary to compute absorption spectra. While this is valid for most cases encountered in UV/VIS spectroscopy, the short wavelengths associated with X-ray radiation gives rise to non-zero contributions from the electric quadrupole and magnetic moments to the X-ray absorption spectrum. It has been shown that there are significant electric quadrupole contribution in the pre-edge region of the Fe K-edge XAS. Therefore it is necessary to include these terms in our calculation. The calculation of the magnetic dipole and electric quadrupole matrix elements is complicated by the fact that these contributions depend on the choice of the origin in the molecular frame. The authors of the ORCA package have devised a way of minimizing the impact of this effect by adjusting the origin to ensure the speedy convergence of the Taylor expansion of the transition moment.[57] Upon convergence of the TD calculation the origin is adjusted for each transition. This has the

effect of maximizing the transition density at the new origin which is typically centered on the absorbing atom. We include the electric quadrupole contribution using the origin shifting procedure in all of the TDDFT calculations.

The electric quadrupole contributions in the TPDFT calculations using the StoBe-deMon code do not include an origin adjustment procedure, but we have taken steps to minimize the origin dependence of the transition moments. The TPDFT spectra are calculated using the standard orientation from the Gaussian 09 structure optimization which places the origin at the center of mass of the molecule. This ensures that the iron center is very near the origin and since the electron is being excited from the iron core, there should be a significant transition density at the origin. X-ray transitions to the continuum are strongly dipole allowed, and there are no noticeable effects due to the inclusion of electric quadrupole contributions in that region. Contributions to the X-ray spectrum from magnetic dipole terms are expected to be small at the Fe K-edge and are not included in these calculations.

2.3 Results and Discussion

A. Structures and Energetics

The key geometric parameters for the LS, HS and HSA complexes calculated using DFT are given in Table 2.1. The quality of the calculated structures is assessed by comparing them with their crystal structure and data from X-ray absorption experiments. We focus our discussion on the iron-nitrogen bond distances. The molecules reported in this study have three nitrogen atoms that are members of the pyridine rings, and three that are part of the imine functional groups as shown in Figure 2.1. Table 2.1 lists the average Fe–N bond lengths for the pyridine ($Fe–N_{pyr}$)

Table 2.1 Structural parameters for the Fe(II) SCO complexes

	$Fe–N_{pyr}$ (Å)	$Fe–N_{im}$ (Å)	$Fe–N_{avg}$ (Å)	Reference
LS	1.981	1.957	1.969	this study
HS	2.264	2.140	2.202	this study
HSA	2.321	2.153	2.237	this study
LS crystal	1.981	1.950	1.965	62
HSA crystal	2.282	2.143	2.213	63
LS in ACN			1.96	17
HS in ACN			2.17	17
HSA in ACN			2.19	17

and imine ($Fe–N_{im}$) nitrogens and the total average Fe-N bond distance ($Fe–N_{avg}$). We note that the calculated $Fe–N_{pyr}$ bond length is greater than the $Fe–N_{im}$ bond length for all three SCO complexes. The difference in the two types of Fe–N bond lengths is 0.024 Å, 0.124 Å and 0.168 Å for the LS, HS and HSA optimized complexes respectively. These numbers indicate that there is a large structural distortion in going from the low-spin to the high-spin state in this series of SCO complexes. Another relevant geometric parameter is angular distortion around the nitrogen atom that is not coordinated to the iron center. The magnitude of this distortion is reflected in the dihedral angle between planes defined by this nitrogen atom and the three surrounding carbon atoms. In the LS structure the four atoms nearly lie in a plane with a dihedral value of 177.5º. In the HS and HSA cases the dihedral is 132.9º and 148.5º, respectively. It is likely that the planar nature of the nitrogen and surrounding carbon atoms in the LS complex is due to strain generated

by the short Fe–N bonds. The elongation of the Fe–N bond lengths in the high spin complexes, reduces the strain resulting in a smaller dihedral angle and a pyramidal structure around the uncoordinated nitrogen atom.

The calculated DFT structures are in good agreement with the available experimental data as seen from Table 2.1. The optimized structure for the LS complex differs in the $Fe–N_{im}$ bond distance from the crystal structure by only 0.007 Å and agrees exactly with the $Fe–N_{pyr}$ distance.[62] Additionally, the $Fe–N_{avg}$ theoretical bond lengths agree with the experiment for the LS complex dissolved in acetonitrile (ACN) to within 0.01 Å.[17] The dihedral angle between the planes defined by the nitrogen atom not coordinated to the iron center and the three surrounding carbon atoms is 177.1º in the LS crystal structure in Reference 62 and agrees quite well with the calculated value of 177.5º. The calculated structure for the HSA complex also agrees well with the crystal structure.[63,64] The $Fe–N_{pyr}$ bond distance is 0.039 Å longer for the calculated HSA structure than for the crystal structure, while the $Fe–N_{pyr}$ bond distance is 0.010 Å longer than the HSA crystal structure. The $Fe–N_{avg}$ bond distance for the calculated HSA structure differs by 0.02 Å from the experimentally determined value determined with the complex dissolved in acetonitrile. We expect that the methyl groups present in the HSA have hydrogen bonding interactions with the solvent which results in the modification of the structure in solution. The HS complex is a transient species and there is no crystal structure available to compare with the calculated structure. Picosecond X-ray absorption experiments measure a $Fe–N_{avg}$ bond distance of 2.17 Å for the transient HS species dissolved in acetonitrile.[17] The calculated $Fe–N_{avg}$ bond distance of 2.202 Å agrees well with the experimental value. The experimental $Fe–N_{avg}$ bond distance was extracted from the experimental data assuming a symmetric dilation of all the iron-

nitrogen bonds. We note that the calculations predict an asymmetric bond dilation mirroring the changes observed in the crystals structures of the ground state LS and HSA complexes. The next sections explore how these geometrical changes along with the electronic structural changes manifest themselves in the X-ray absorption spectra of the SCO complexes.

B. Experimental X-ray *Absorption Spectra of the SCO complexes*

The experimental X-ray absorption near edge spectra (XANES) of the SCO complexes dissolved in acetonitrile at room temperature from Reference 17 are shown in Figure 2.2. Figure 2.2a shows the static XANES spectra for the ground state LS and HSA complexes. The XANES

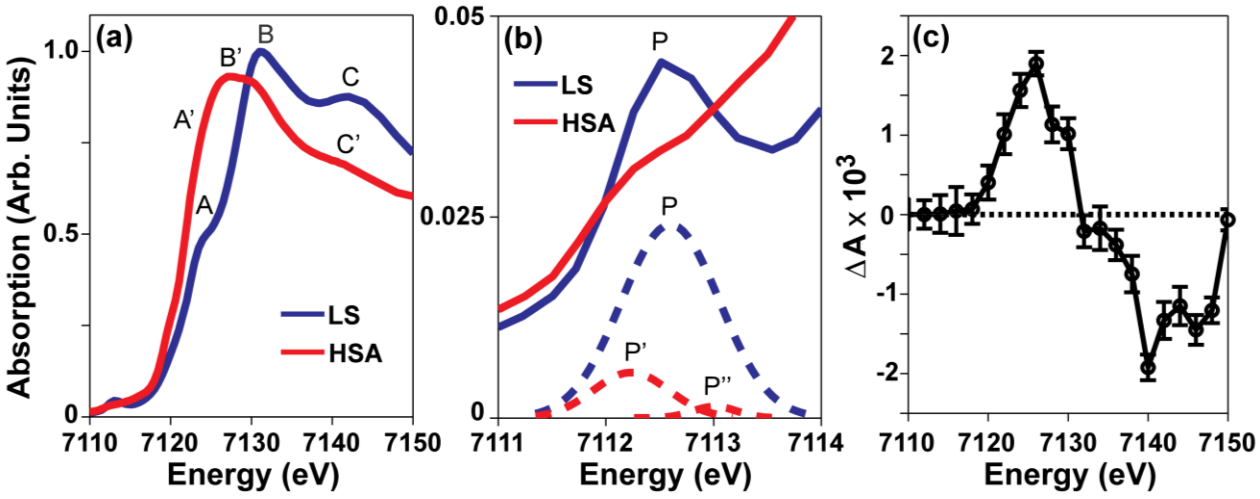

Figure 2.2 Experimental X-ray absorption spectra of the low-spin, transient high-spin and high-spin analogue complexes dissolved in CH_3CN at the Fe K-edge. (a) Static XANES spectra of the low-spin and the high-spin analogue complexes. (b) Expanded view of the pre-edge region of the low-spin and high-spin analogue complexes shown in (a). The dotted lines are Gaussian lineshapes fitted to the weak spectral features in the pre-edge region following a subtraction of a polynomial fit to the rising K-edge. (c) Transient difference X-ray absorption spectrum recorded 330 ps after pumping the $^1A_1 \rightarrow {}^1MLCT$ excitation of the LS complex at 400 nm. The difference spectrum contains the spectral signatures of the transient high-spin quintet state of the LS complex. Reprinted with permission from {J. Phys. Chem. A, 2006, 110 (1), pp 38–44}. Copyright {2006} American Chemical Society.

spectrum of the LS complex exhibits three major features labeled A, B and C following the notation used in Reference 17. Spectral features A (7124 eV) and B (7131 eV) are located near the Fe K-edge and are assigned to 1s $\rightarrow$ 4p transitions. The absorption feature labeled C above the edge at 7142 eV is attributed to multiple scattering effects. The corresponding spectral features in the HSA XANES region are labeled A', B' and C'. The spectral features near the K-edge in the HSA complex are significantly red-shifted with respect to the LS K-edge. The near edge feature, denoted as A', is located at 7120 eV, and the main edge peak, B', is found at 7128 eV. The red shifts and changes in amplitude of the spectral features are attributed to the modifications in the electronic structure resulting from less overlap between the metal 4p and ligand $2\pi^*$ orbitals due to lengthening of the Fe-N bond in the HSA complex. The structural changes between the LS and HSA complexes also affect the multiple scattering feature C' found at 7141 eV.

The pre-edge region in XANES spectra is extremely sensitive to the changes in the electronic structure near the absorbing atom. At the Fe K-edge, pre-edge features are assigned to 1s $\rightarrow$ 3d dipole-forbidden and quadrupole-allowed excitation. Figure 2.2b provides a detailed view of the pre-edge region of the LS and HSA static XANES spectra. The LS complex has a sharp intense pre-edge feature (P) at 7113.2 eV with a FWHM of 2.1 eV. The HSA complex has two pre edge features P' and P'' located at 7112.5 and 7114.0 eV, respectively with FWHM of 1.7 and 1.0 eV. The ratio of the peak areas of P'/P'' is 7:1. We note that although there seems to be a significant decrease in intensity in going from the low to high-spin complex, the overall area of the pre-edge features is strongly dependent on the choice of the polynomial background subtracted prior to Gaussian fitting of the lineshapes. The TDDFT calculations performed in this study allow us to interpret the pre-edge spectral features using a molecular orbital picture as discussed below.

Figure 2.2c shows the difference XANES spectrum of the photoexcited HS species collected at 330 ps following MLCT excitation of the low-spin complex with a femtosecond 400 nm pump pulse. The positive feature in the difference spectrum indicates an increase in the spectral intensity of feature B and a red shift of the K-edge upon a photoinduced SCO process in the LS complex. The negative spectral feature in the difference spectrum results from a decrease in intensity of the C and D features in the transient HS complex relative to the LS complex. The transient X-ray absorption reveals that the changes in the XANES region for the photoexcited HS complex, mirror the static XANES spectrum of the HSA complex.

C. Calculated Near Edge X-ray *Absorption Spectra of SCO Complexes Using Transition Potential DFT*

The TPDFT simulations of the XANES region in the X-ray absorption spectrum of the LS, HS and HSA complexes are shown in Figure 2.3. The TP calculation yields a large discrete set of transitions across a 40 eV window as shown for the LS complex in Figure 2.3. The amplitude of these transitions is given by the sum of electric dipole and electric quadrupole contributions. The discrete spectral transitions are convoluted with Gaussian lineshapes to yield the spectral envelopes plotted in Figure 2.3. The Gaussian linewidths are determined by adjusting the widths of the spectral transitions in the pre-edge region to agree with the experimental results shown in Figure 2.2b. This results in a FWHM of 1.5 eV for the individual spectral transitions the pre-edge region. The linewidths of the transitions above the pre-edge region is determined by linearly increasing the value of the FWHM from 1.5 eV to a final width of 10 eV spanning a 15 eV spectral window. This convolution procedure has been widely used in the literature and it accounts for experimental spectral resolution, broadening of spectral resonances involving final

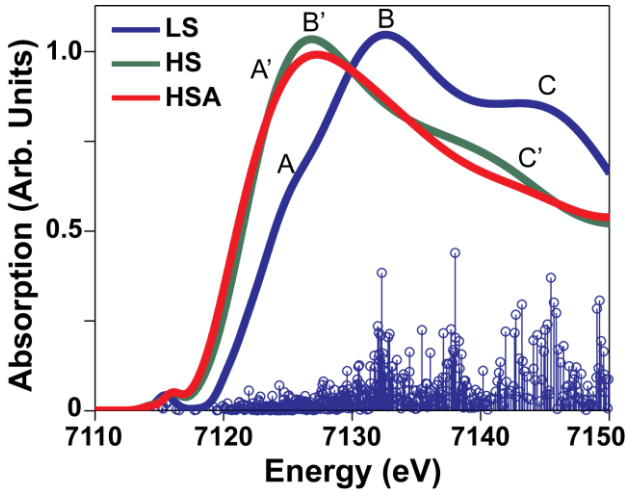

Figure 2.3 XANES spectra at the Fe K-edge of the LS, transient HS and HSA complexes calculated using TP-DFT. The individual transitions for the LS complex are plotted as stick spectra (blue open circles). The LS spectrum is normalized to its maximum value. The same normalization factor is applied to the HS and HSA spectra.

states in the continuum, and averaging out spurious basis set effects.[65] We note that DFT fails to predict the correct energy of the absorption edge due to deficiencies in DFT functionals and neglect of relativistic effects.[56] Each of the calculated X-ray absorption spectra is shifted by +62.3 eV to align the LS Fe K-edge with the experimental result. An advantage of the TPDFT approach for simulating XAS is the ability to calculate many excited states. There are ~600 discrete transitions shown in Figure 3 and over 1300 excitations were computed in the TPDFT calculation. The TPDFT methodology accurately models the X-ray absorption spectra 10–20 eV above the edge because the large number of possible transitions is able to approximate a continuum of states.

The calculated spectra of the LS, HS and HSA complexes in Figure 2.3 exhibit all the near edge spectral features (A(A')-C(C')) present in the experimental spectra shown in Figure 2.3a. For the LS case, the TP-DFT calculation shows a spectral feature (A) prior to the edge jump at 7125 eV, the K-edge peaks at 7133 eV and there is a post-edge feature (C) at 7145 eV. The XAS

of the HSA complex also shows all of the features present in the corresponding experimental spectrum. The calculated spectrum shows an increase in spectral intensity in the near-edge region labeled A'. The greater intensity in this spectral region gives rise to a broader main spectral feature in the HSA spectrum, and the near edge feature A' at 7120 eV is not as pronounced as in the spectrum of LS complex. The main spectral feature (B') peaks at 7127 eV and C' is found at 7145 eV. The calculated Fe K-edge spectrum for the transient HS complex is qualitatively very similar to the spectrum of the HSA complex. The main XAS peak (B') of the HS complex is red-shifted by 5 eV with respect to the LS spectrum and there is a post-edge feature C' at 7141 eV.

In order to evaluate the ability of the TPDFT methodology to simulate the XANES region of Fe K-edge of SCO complexes, we compare the difference spectra from both static and transient

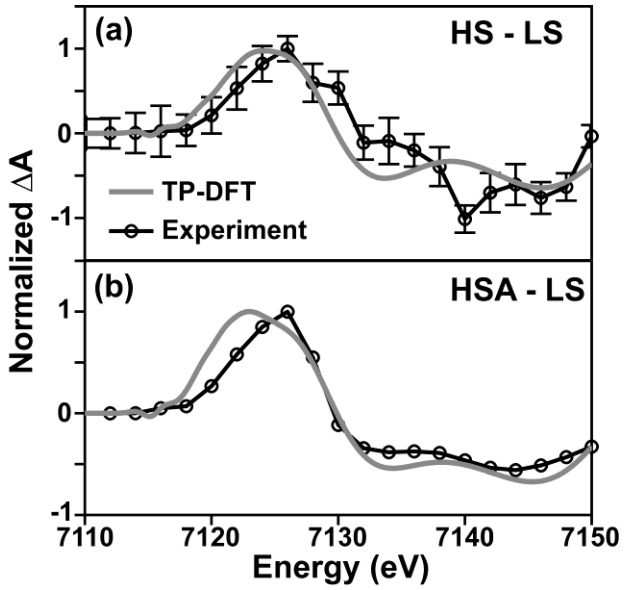

Figure 2.4 (a) The difference absorption spectra of the transient HS and the LS complex. The experimental spectrum (black line) recorded 330 ps following MLCT excitation of the LS complex and the difference spectrum computed using TP-DFT (gray line). (b) Difference absorption spectrum between the experimental static XAS spectra of the HSA and the LS complex (black line) and the corresponding calculated difference spectrum (gray line). Each difference spectrum is normalized to its positive maximum value.

XAS experiments to the difference spectra calculated from the TPDFT results in Figure 2.4. This reveals that the calculations of the Fe K-edge XANES region of SCO complexes using TPDFT are in good agreement with the experiment. The XANES difference spectra shown in Figure 2.4 are dominated by a large positive feature between 7121 and 7130 eV. This is due to the red shift in the absorption edge in the high-spin complexes following the rearrangement of the 3d electrons and the subsequent geometrical changes in the molecule. The two negative features at 7134 and 7146 eV in the calculated difference spectra result from a decrease in the spectral intensity of the high-spin complexes relative to the LS complex. These negative features are well correlated with the negative peaks in the experimental difference spectra as seen in Figure 2.4.

The greatest difference between the TPDFT results and the experiment are in the energy shifts of the X-ray spectra of the low- and high-spin complexes. The positive peak in the experimental difference spectra is located at 7125 eV, while it peaks at 7123 eV in the calculated difference

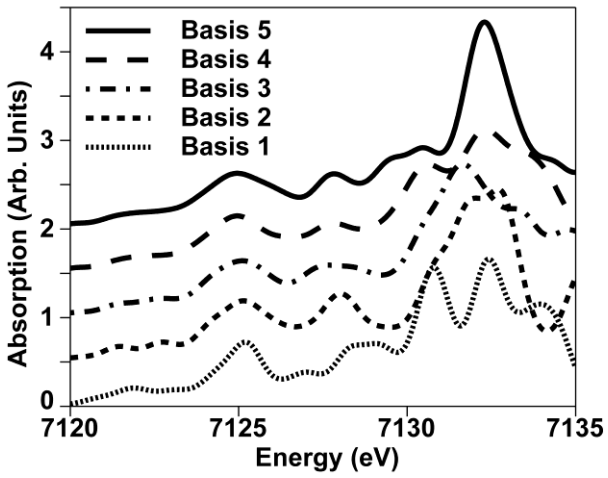

Figure 2.5 The effect of the augmentation basis set on the calculation of X-ray absorption spectra at the Fe K-edge for the LS complex using TPDFT. Basis 1 – 5 refer to sets with no augmentation (1), Fe augmentation (2), Fe plus 2 nitrogen atoms (3), Fe plus 4 nitrogen atoms (4), and Fe plus 6 nitrogen atoms augmented. Each spectrum is offset vertically by 0.5 units for clarity.

Table 2.2 XANES transitions and their oscillator strengths for the SCO complexes calculated using the PBE0 functional in TD-DFT. The contributions of the electric dipole and the electric quadrupole to the oscillator strength are listed.

Complex	Energy (eV)	Oscillator Strength (x 10^2)	Electric Dipole Contribution (x 10^2)	Electric Quadrupole Contribution (x 10^2)
LS	7113.2	8.3	2.5	5.8
	7113.2	8.6	2.5	6.1
HS	7112.3	6.7	2.7	4.0
	7112.7	4.1	1.8	2.3
	7113.7	8.0	5.4	2.6
	7114.4	11.7	8.8	2.9
HSA	7112.3	5.3	1.7	3.6
	7112.6	3.5	0.6	2.9
	7113.7	8.1	5.5	2.5
	7114.4	8.7	6.6	2.1

spectrum. This is not a surprise given that a finite basis set, approximate exchange-correlation functionals, and empirical broadening are being employed to calculate excitations to continuum states.

We have used a finite basis set to simulate the K-edge spectra, but energies above the absorption edge represent transitions to a continuum of electronic states. This is problematic, since it is not possible to strictly represent a continuum of states in a finite atom-centered

Gaussian basis. To aid in the representation of the continuum states, we augment the initial basis set with a large diffuse basis set after optimizing the TP state. After augmentation, the orbitals are orthogonalized and basis functions resulting in linear dependencies are removed. Five augmentation basis sets have been tested and the results are displayed in Figure 2.5. In the first case, no augmentation is used and in the remaining four cases, a large augmentation set of 25s, 25p, and 25d functions is placed on the Fe center. The convergence of the set is tested by augmenting the surrounding nitrogen atoms with sets of 19s, 19p, and 19d functions. In the second set only the iron is augmented, and in the next three sets, we have augmented two, four, and six nitrogen atoms, respectively. The basis sets were placed on pairs of nitrogens on opposite sides of the iron center to make the basis set as symmetric as possible.

In Figure 2.5, all discrete transitions have been convoluted with a Gaussian peak of 1.0 eV FWHM. This broadening has been chosen because it makes differences between the basis sets more obvious. Note that the pre-edge region is not shown in Figure 2.5. We observe a 0.1 eV red shift of the pre-edge feature due to the presence of the augmentation basis on the iron atom and note that this perturbation is invariant to the size of the augmentation set. In this study we employed standard augmentation sets from the StoBe basis set library, but it may be necessary to develop transition metal specific augmentation basis sets. Unlike the pre-edge region, the continuum shown in the main area of Figure 2.5 is highly sensitive to the augmentation set used. Each larger augmentation set is vertically offset with the basis size increasing from bottom to top. In the bottom curve, there are oscillations in the spectrum between 7120 and 7124 eV. These oscillations are damped as the basis set size is increased, and the spectrum becomes smoother in this spectral region. We note that the TP-DFT calculations become very basis set dependent at high energies. For this reason, we focus on simulating a 40 eV spectral window of

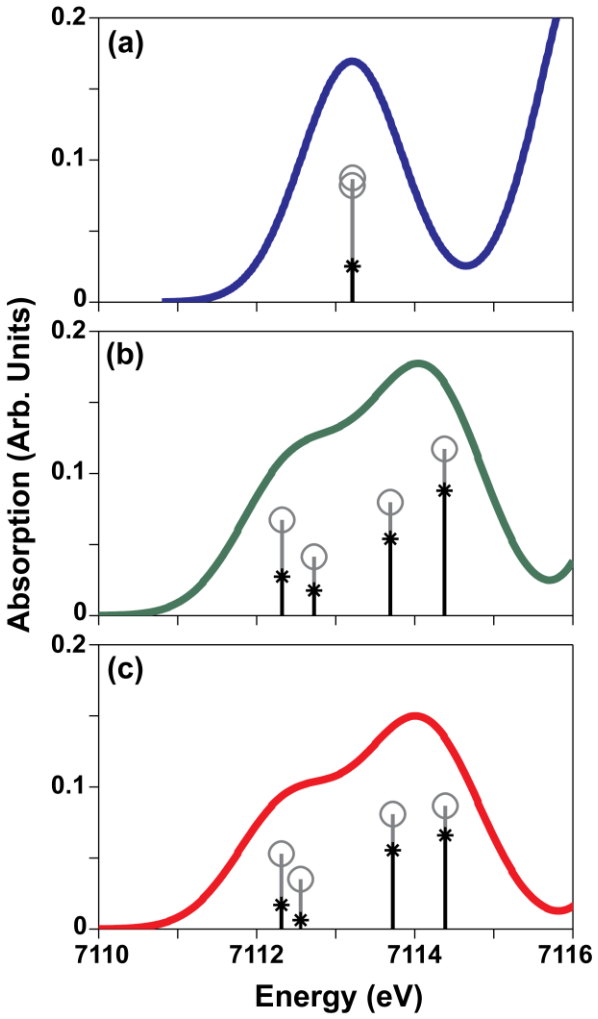

Figure 2.6. XANES pre-edge region computed with TDDFT using the PBE0 functional for the LS (a) HS (b), and HSA (c) complexes. Grey circles represent the oscillator strength that includes electric dipole, and electric quadrupole contributions, while the black asterisks include only the electric dipole contribution. Each transition has been convoluted with a Gaussian peak of 1.5 eV FWHM to generate the spectral envelope.

the XANES spectrum. Since the spectral features in the calculated X-ray spectra are smoothed upon increasing the size of the augmentation basis, we conclude that it would be best to augment all of the surrounding nitrogen atoms because this would maximize the symmetry in the basis set. The basis set that is used in all comparisons with experiment includes diffuse functions centered

on the iron center and the six adjacent nitrogens. A similar augmentation scheme has been used to reproduce the XAS of water.[66]

D. Calculated Pre-Edge X-ray Absorption Spectra of SCO Complexes Using Time-dependent DFT

Calculated X-ray spectra of the pre-edge region of the Fe K-edge of the LS, HS and HSA complexes using TDDFT with the PBE0 functional are shown in Figure 2.6. The spectral envelopes are created by convoluting the individual transitions with Gaussian peaks of 1.5 eV FWHM similar to the broadening used in the TPDFT simulations. The TDDFT spectra are shifted by +144.8 eV to match the experimental pre-edge region. The electric dipole contribution to the overall amplitude is shown by black asterisks for each individual transition. The grey circles represent the summation of the electric dipole and electric quadrupole contributions to the oscillator strength. Table 2.2 lists all the transitions shown in Figure 2.6 along with the total oscillator strengths and the electric dipole and quadrupole contributions.

The calculated spectra agree well with the experimental spectra shown in Figure 2.2b. There is a single feature in the LS spectrum and two features in the high-spin spectra. The calculated pre-edge region for the LS complex displayed in Figure 6a is composed of two nearly degenerate transitions appearing at 7113.2 eV. These transitions from the Fe 1s orbitals to the Fe 3d orbitals would be degenerate in the limit of a truly octahedral complex forming the ^{2}E peak predicted by ligand field theory.[29] The structure of the LS complex is not octahedral as discussed in Section 2.3a and this break of symmetry is evidenced by the slightly higher intensity of one of the two transitions in Figure 2.6a. These 1s $\rightarrow$ 3d transitions derive the majority of their oscillator strength from electric quadruple transitions and are composed of $\sim$ 30% electric dipole

contributions as listed in Table 2.2. The excited state orbitals contributing to the peaks in the LS pre-edge region are the vacant e_g orbitals. These can be seen in Figure 2.7 where the positive difference in electron densities between the ground and core excited state (the negative difference is located at the iron core for each transition) is plotted using Molekel.[67] For the LS case, the excited states are centered on the iron atom and oriented along the bonding axes. Thus, they exhibit anti-bonding character as expected for e_g orbitals in octahedral symmetry.

The calculated pre-edge spectra of the transient HS and the HSA complexes are shown in Figure 2.6b and 2.6c respectively. The spectra exhibit very similar characteristics. In both complexes, there are four transitions from the Fe 1s orbital that contribute to the pre-edge region. The transition energies and oscillator strengths are listed in Table 2.2. For the HS spectrum, the first two transitions have electric dipole contributions of 40 and 44% of the total oscillator strength. The two higher energy transitions have stronger dipole components of 68 and 75% of the transition strength. The excited state difference densities are shown in Figure 2.7 for each of the four transitions. For the two lower energy transitions the increase in electron density takes the shape of non-bonding orbitals oriented between the bonds. We assign these transitions as excitations to the t_{2g} orbitals vacated in the SCO transition from low- to high-spin. The two higher energy states in both high-spin complexes have very similar character to the excited states of the LS complex. These states are identified as excitations to the e_g orbitals. We note that the transient experimental difference spectrum shown in Figure 2.2c does not show any differences in the pre-edge region. We believe that this is due low signal-to-noise and insufficient spectral resolution (2.5 eV). A recent transient x-ray absorption experiment probing the SCO process in a similar Fe(II) complex reports on changes in the pre-edge region as predicted by our simulation.[25]

In the HSA pre-edge spectrum the transitions appear at nearly identical energies as those in the HS spectrum and are listed in Table 2.2. These four transitions result in two pre-edge peaks reproducing the features in the experimental spectrum of HSA complex (Figure 2.2b). The energy splitting in the experimental HSA spectrum is 1.5 eV for the two fitted peaks. Fitting two Gaussian peaks to the calculated spectrum shown in Figure 2.6c yields a splitting of 1.6 eV, so the calculated spectrum correlates well with the experimental results. The amplitudes of the peaks in the simulated HSA spectrum are larger than those in the experimental spectrum. As we pointed out previously, the intensities of the pre-edge features depend strongly on the polynomial

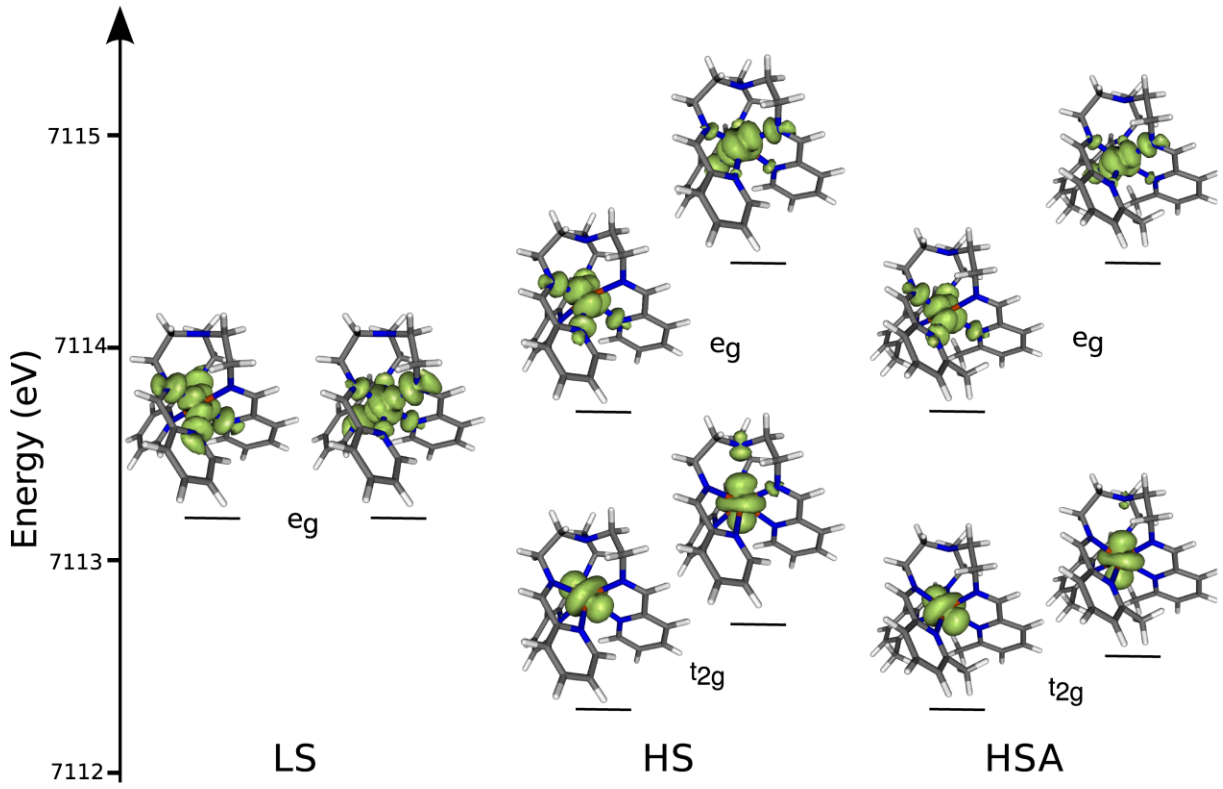

Figure 2.7 Energetic map of Fe 3d orbitals of LS, HS, and HSA complexes constructed from TDDFT simulations of the pre-edge regions of the X-ray absorption spectra. Each surface shows the positive part of the difference in the electron density (P) upon core excitation as defined by $\Delta = P_{ex} - P_0$. These difference densities show the distribution of the electron excited from the iron core. The negative parts of difference densities are not visible because they are concentrated at the small region occupied by the Fe 1s electrons. All surfaces are generated with the Molekel program (Ref . 67).

background subtracted prior to fitting the experimental features. The two lower energy transitions in the simulated HSA spectrum have electric dipole contributions of 32 and 17% while the higher energy transitions are 68 and 76% electric dipole allowed. The character of the excited state densities shown in Figure 2.7 allows the same assignments for the transitions as in the HS case.

While these complexes are not perfectly octahedral, assuming octahedral symmetry allows us to correlate our *ab initio* results with the ligand field model. The assignment of the various transitions in the pre-edge region of the Fe K-edge absorption spectra of the LS, HS and HSA complexes allows us to map out the energetics of the iron 3d orbitals involved in the SCO process as shown in Figure 2.7. Looking at the excited state electron densities for the high spin complexes shown in the center and right columns of Figure 2.7, we notice a break in degeneracy of the t_{2g} and e_g states. This can be attributed to a combination of large decrease in molecular symmetry in going from the LS to the HS complex, as well as, multiplet effects. As noted earlier, the Fe–N_{pyr} bond lengths are ~0.1 Å greater than the Fe–N_{im} bond lengths in the HS complex, but these values differ by only 0.02 Å in the LS complex. This results in a nearly degenerate set of e_g states for the LS complex.

By taking the difference between the average t_{2g} and e_g transition energies we are able to extract 10Dq values of 1.55 and 1.35 eV for the HS and HSA complexes, respectively. These values are well correlated with the splitting of 1.5 eV observed in the HSA spectrum in Figure 2.2b. Our calculated results also agree with the estimates by Wilson *et al.* of 1.41 eV measured from the optical absorption spectra of the HSA complex.[68] Additionally, these results are in good agreement with transient X-ray experiments at the Fe L-edge of the LS complex, which predict the 10Dq value to be ~1 eV for the transient HS complex.[16] Our results show that there is

an increase in the effective ligand field splitting because the energies of the 3d orbitals spread out as the symmetry decreases as shown in Figure 2.7. Moreover, the TDDFT calculations of the pre-edge region shows that the experimentally observed splitting of the two peaks in the HSA complex can be directly related to the 10Dq ligand field parameter. This provides a spectroscopic handle for monitoring time-dependent changes in the electronic structure of Fe(II) complexes undergoing spin state changes.

In the photoinduced low-spin to high-spin SCO process, the Fe-N bond lengthens decreasing the overlap between the metal and ligand orbitals. Figure 2.7 clearly shows the decrease in the overlap of the metal and ligand orbitals as the bond lengths increase in going from the LS to the HS complex. In the LS complex, the e_g excited states have a significant amount of density delocalized onto the nitrogen atoms of the ligands (left panel, Figure 2.7). The e_g states in the HS complex have significantly less electron density on the nitrogen as shown in the center panel of Figure 2.7. This is clear evidence of a decrease in π-backbonding (mixing of unoccupied ligand π* states with iron d-orbitals) associated with the low-to-high spin transition. The further decrease in metal-ligand overlap is evident in going from the HS to HSA complex. In particular, the higher energy t_{2g} excited state has a significant amount of electron density on the seventh nitrogen that does not directly coordinate the iron atom, but in the HSA complex there is very little electron density away from the iron center. This observation can be put on a quantitative footing by considering the Mayer bond orders (MBO) of the LS, HS and HSA complexes.[69] The average MBO for the six Fe-N bonds in the LS, HS and HSA complexes is 0.67, 0.41, and 0.36, respectively. There is a large decrease in bond order in going from low- to high-spin, and there is a further decrease in the HSA complex as compared to the HS complex. While these numbers should not be taken as a direct measure of the amount of π-backbonding because the bond orders

will include σ-bonding as well, they show a clear decrease in overlap of metal and ligand orbitals.

A comparison of the calculated pre-edge intensities for the low-spin and high-spin complexes in Figure 2.6 and shows that the amplitude of pre-edge features in the LS spectrum are comparable to features in the high-spin spectra. The traditional interpretation of pre-edge features in iron K-edge XAS would predict that the high-spin species would have greater intensity than the LS complex because they have lower symmetry resulting in greater mixing of the Fe 3d-4p orbitals. We have examined the Mulliken populations of the orbitals contributing to the excited states in the pre-edge region and have not observed a clear correlation between the strength of the pre-edge transition and the amount of iron 4p character predicted by population analysis. While the orbitals contributing to transitions in the high-spin case do have slightly increased 4p character (< 0.5% in most cases), the low-spin orbitals have no 4p contribution, yet there is still a sizable dipole contribution to the pre-edge transitions in the LS complex. We also observe a number of dipole allowed transitions to ligand π* orbitals with transition energies lying a few eV above the pre-edge region. We postulate that the overlap between the metal and ligand orbitals provides a dipole intensity mechanism for 1s→3d transitions, since there is ~40% dipole character contributing to the intensity of the pre-edge transitions. This explains why the LS complex has similar pre-edge intensity despite being much more symmetric, and it also explains the decrease in the intensity of the pre-edge region in going from the HS to the HSA complex. Consequently, the intensity of the pre-edge features is a function of both the symmetry of the molecule and the degree of π-backbonding to the metal center.

We have tested the effect of the choice of functional used in the TDDFT calculations of the pre-edge region of the SCO complexes. Figure 2.8 displays the results of the pre-edge region of

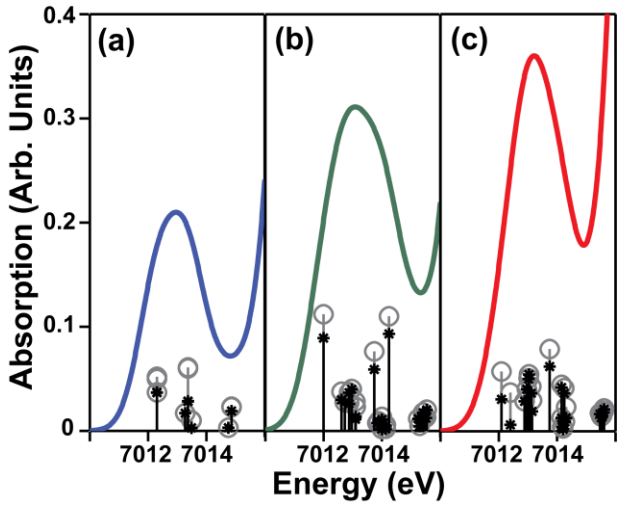

Figure 2.8 XANES pre-edge region computed with TDDFT using the BP86 functional for the LS (a), HS (b), and HSA (c) complexes. Grey circles represent the oscillator strength that includes electric dipole and electric quadrupole contributions while the black asterisks give only the electric dipole strength. Each transition has been convoluted with a Gaussian peak of 1.5 eV FWHM to generate the spectral envelope.

the Fe K-edge spectra for the LS, HS and HSA complexes simulated with TDDFT at the BP86 level of theory. These spectra are very different from the results shown in Figure 2.6 obtained using the hybrid PBE0 functional. In each of the spectra calculated with the BP86 functional, there are many peaks contributing to each of the pre-edge features. An analysis of the transitions in Figure 2.8 shows that they are transitions from the Fe 1s orbital to both the iron 3d orbitals and the ligand π^* orbitals centered on the pyridine rings. The transitions in Figure 2.8 that have significant quadrupole character are predominately iron 3d orbitals. The clusters of dipole allowed transitions in Figure 2.8b and c are predominately to ligand orbitals. The presence of transitions to the ligand orbitals changes the shapes of the spectra. While the LS spectrum produces a single peak, it is an asymmetric feature contrary to the experimental spectrum (Figure 2.2b). In the case of the high-spin species, the two peaks that were clearly visible for the hybrid

functional results and seen in the experiment have coalesced into a single feature. We note that the transitions predicted by the GGA functional heavily mix the metal and ligand orbitals. Consequently, it is difficult to extract chemical information about the metal-ligand bonding from these results. It is well-known that TD-DFT underestimates the energies of charge transfer transitions.[70] This problem is particularly bad with pure functionals like BP86. Due to the presence of Hartree-Fock exchange, hybrid functionals provide better estimations of charge transfer energies. In our PBE0 results we observe that the MLCT transitions to the ligand π^* orbitals appear at higher energies than the 3d excited states. In the BP86 results the transitions 3d transitions and MLCT states appear at the same energy generating much different, and likely incorrect, pre-edge spectra.

In order to test the superiority of the hybrid functional for this application, we calculated the optical absorption spectra with the def2-TZVP basis on all atoms and find that the hybrid functional performs much better in all cases. For the LS case the BP86 functional predicts a strong MLCT transition at 893 nm whereas the PBE0 value is predicted to be 528 nm. The hybrid functional agrees quite well with the maximum of the lowest energy MLCT feature determined by experiment at 560 nm. MLCT transitions for the high-spin compounds are estimated by the BP86 functional to be 1015 and 969 nm for the HS and HSA compounds, respectively. The corresponding values predicted by the PBE0 functional are 533 and 481 nm. The lowest energy MLCT band in the UV-Vis spectrum appears at 490 nm for HSA complex. Thus, the BP86 functional consistently underestimates the energy of MLCT transitions. This analysis confirms that the PBE0 functional provides the better description of the pre-edge region of the XANES spectrum.

The TDDFT results presented above show that the electronic structure of the iron atom is revealed by the pre-edge features of iron K-edge XAS spectra. The low-spin complex gives rise to a single feature while two peaks are clearly discernable for high-spin species. Moreover, this approach allows us to map out the energetics of the d-orbitals and predict values for ligand-field splitting energies. We have found that the relative contribution of electric dipole and quadrupole report on the character of the excited states. Finally, it is shown that choosing a functional that gives a reasonable description of charge transfer effects is necessary for complexes with low-lying MLCT states.

E. Comparison of the results from the TP- and TDDFT calculations

From a comparison of Figs 2.3 and 2.8 where the simulations are performed with the same functional, it is evident that there are some significant differences in the XANES spectra calculated by the TP- and TDDFT methods used in this study. The biggest advantage of the TP methodology is the ability to simulate a ~ 40 eV spectral range in the XANES region of the Fe K-edge spectra of SCO complexes. In the case of the TDDFT calculations, the results focused on simulating a narrow (~6 eV) pre-edge region of the Fe K-edge. While it is theoretically possible to simulate the regions above the pre-edge region with TDDFT, one would have to solve the TDDFT eigenvalue problem in the large diffuse basis set used for TP calculation. This proves to be a computationally intractable problem. The TP methodology, allows one to calculate hundreds of transitions in a computationally efficient manner.

Another significant difference between the TP- and TDDFT approaches is that the TP includes orbital relaxation. This is clearly seen in the energy required to shift the spectra to align them with theoretical predictions. The TPDFT results are shifted by +62.3 eV while the TDDFT

results calculated with the same functional are shifted by +182 eV. While a portion of this difference could be attributed to differences in basis sets, orbital relaxation is a much larger contribution. Moreover, it is interesting to consider how orbital relaxation effects different MO's. The transition potential strongly stabilizes the iron-centered orbitals relative to the ligand orbitals due to the increased effective nuclear charge on the metal due to the presence of the half occupied core hole. Despite having concerns about the pre-edge features from the TPDFT calculations, we point out that the pre-edge regions of the high-spin spectra shown in Figure 2.3 clearly exhibit two features each, but there is just a single feature in both Figure 2.8b and c. We attribute the splitting of the pre-edge in the TPDFT calculations to the stabilization of the t_{2g} orbitals by the transition potential. Consequently, methods that include orbital relaxation may be necessary to produce qualitatively correct spectra if transitions to ligand orbitals overlap energetically with transitions to 3d orbitals. Based on our discussion earlier of preferring a hybrid functional to simulate the pre-edge region, it would be useful to calculate the Fe K-edge spectra with TPDFT using a hybrid functional.

F. Comparison with Previous Studies

Theoretical calculations of Fe K-edge X-ray absorption spectra of equilibrium and transient low and high spin Fe(II) complexes have been previously reported using multiple scattering calculations, atomic multiplet calculations and a DFT based method. A number of studies have utilized full multiple scattering calculations to interpret the Fe K-edge XAS of SCO complexes.[11,12,17,28,71] Real space *ab initio* based full multiple scattering calculations have been used within the dipole approximation to calculate the X-ray absorption cross-section using codes such as FEFF and MXAN.[72,73] These codes have proven to be very effective in reproducing

static experimental Fe K-edge spectra and they provide a reliable method for extracting structural information from the EXAFS spectrum and interpretations of the near-edge features in terms of multiple scattering effects from several coordination shells around the Fe atom. We note that the major differences in the analysis of XANES spectra using multiple scattering and MO based approaches such as TPDFT, arise in the language used to discuss the results and in the implementations of the theories.

One feature of particular interest, is the near edge feature that we have labeled B/B' in our experimental and calculated spectra (see Figure 2.2a and Figure 2.3). The traditional MO interpretation of this feature assigns this to 1s $\rightarrow$ 4p transitions in the metal atom. The red shift of this spectral feature accompanying the SCO transition suggests that the increase in the Fe-N bond length decreases the overlap of the ligand σ-antibonding orbitals with the iron 4p orbitals. This results in a stabilization of the iron 4p states that appears as a red shift in the X-ray absorption spectrum. These MO interpretations of the energy shifts in the LS and HS molecules used in this study was confirmed by Khalil *et al.*, who simulated the transient XAS spectra using FEFF 8.0, and were able to correlate the shift in the absorption edge with an increase in the p-projected density of states.[17] Additionally, Chergui and co workers have directly correlated the amplitude of this feature with the iron-nitrogen bond distance using femtosecond and picosecond XANES and FMS simulations in a similar Fe(II) complex.[11,12] This is a particularly powerful insight, since it directly correlates electronic energy levels with a specific atomic motion.

Our TP-DFT results show that the HS and HSA complexes exhibit a similar red-shift in the B/B’ spectral features as seen experimentally and modeled by the full multiple scattering calculations. We note that the overall intensity near the B' and C' features is less in the HSA complex than in the HS even though the Fe-N bond lengths are longer in the HSA complex than

in the transient HS complex. This is contrary to our expectations, because we would expect the 1s $\rightarrow$ 4p contributions to gain greater amplitude in the HSA complex. This suggests that the Fe–N bond length is simply one of the several parameters that impact the amplitude of the near edge features in the Fe K-edge spectra. In the SCO complex used in this study, we have identified that there is a large decrease in symmetry and the dihedral angle defining the geometry around the non-coordinating nitrogen atom. These changes provide additional structural coordinates that will affect the XANES region. Additionally, the TPDFT calculations reproduce the multiple scattering feature D in the spectra yielding results comparable to multiple scattering calculations. The main advantage of the TPDFT calculations employed in this study is that they overcome the lack of chemical detail present in the multiple scattering methods. Full multiple scattering codes generally employ muffin-tin potentials that can give little information about the relationship between the electronic structure of the molecule and the spectral features.[74] For instance, the scattering potential knows nothing of the spin state of the molecule and all of the changes in the XANES spectrum arise from the changes in structure as the Fe(II) molecule goes from low- to high-spin. The DFT-based approaches we employ for simulating the XAS spectra clearly show that the pre-edge region of the spectrum is sensitive to the electronic configuration of the metal center. The advantage of TPDFT is the possibility that it can simultaneously report on the structural and electronic changes in molecules. As shown above, TDDFT cannot access a large energy range of the X-ray absorption, but can provide detailed information about the electronic structure of molecules by simulating the pre-edge region in a rigorous fashion.

The pre-edge features in iron K-edge X-ray absorption spectra have been calculated using a ligand field multiplet analysis approach.[29] In this model, ligand field theory is used to determine the many electron excited states accessed by 1s $\rightarrow$ 3d excitations. A large number of iron

compounds were analyzed in this work, and it was determined that pre-edge features in octahedral complexes arise solely from an electric quadrupole mechanism. The ligand field model predicts a single ^2E excited state for octahedral low-spin d^6 complexes and three ^4T excited states for the HS case. We have similarly identified a single degenerate transition to iron 3d orbitals in the LS spectra from our TD-DFT calculations, and our results for the high-spin complexes show four transitions to the iron 3d orbitals. It seems that the single particle calculations carried out in this study reproduce the many-electron states predicted by a multiplet analysis. This is to be expected since it is well documented that many-electron effects are weak for the pre-edge features of transition metal K-edges.[75] In our study, the oscillator strength for the various pre-edge spectral features had contributions from both the electric dipole and electric quadrupole mechanisms as discussed in the earlier section. In compounds that deviated from octahedral symmetry, the increased pre-edge intensity was attributed to 3d-4p mixing of the metal orbitals in the multiplet analysis. We have examined the Mulliken populations of the orbitals contributing to the excited states and observe no strong correlation between the strength of the spectral transition and the amount of 4p character predicted by the population analysis. In section D we discuss the possibility of the pre-edge transitions gaining intensity from the overlap with the π^* orbitals of the ligands. The complex intensity pattern of the pre-edge features in these molecules highlights the advantages of using *ab initio* methods to describe in detail the molecule specific electronic structural information encoded in the pre-edge features in Fe K-edge XAS.

In previous work by George *et al.* the BP86 functional has been used to simulate the pre-edge region of iron K-edge spectra of several low and high-spin octahedral complexes using TDDFT and there was good agreement between theory and experiment.[56] A range of functionals were

tested in this work and a wide range of functionals were also tested in the simulation of sulfur K-edge spectroscopy.[76] While the energy shifts required to align the theoretical and experimental spectra depend on the choice of functional, the authors report no change in the qualitative nature of the pre-edge spectra. In our work, there is a large difference between results obtained with the hybrid PBE0 and the GGA functional as shown in Figures 2.6 and 2.8. This study has identified the importance of using functionals that provide reasonable descriptions of metal-to-ligand charge transfer states to simulate the pre-edge region of X-ray absorption spectra when ligand π^* orbitals are close in energy to the metal 3d orbitals.

Mukamel and coworkers have developed a method for simulating time-resolved XANES spectra involving valence excited states.[77] In brief, this method relies on a factorization of the core and valence parts of the molecular Hamiltonian. The core excited wave function is obtained by using a Z+1 approximation and TDDFT is used to generate the valence excited states. This method has simulated picosecond transient X-ray absorption spectra for the valence excited states of transition metal complexes such as the MLCT state of $[Ru(bpy)_3]^{2+}$. This method was also used to study the LS and transient HS of the SCO complex used in the present study.[30] The authors largely focused on simulating the Fe K-edge XANES spectra of optically excited states with holes in the valence shell, and found that most transitions were to orbitals of iron 4s, 4p, and nitrogen 2p character. The absence of transitions to the 3d states in this study is partially due to the neglect of electric quadrupole transitions. Our study shows that the iron 3d orbitals play a big role in determining the structure of the pre-edge region, and we observed a negligible contribution from the iron 4s and 4p orbitals in the pre-edge region. Our TPDFT results suggest that large basis sets are required to accurately simulate the near edge regions of the spectrum and our direct application of TDDFT highlights the importance of including quadrupole transitions

for simulating the pre-edge features of Fe(II) SCO complexes. We note that all of the complexes studied here contain no valence excited states. The transient HS molecule is accessible by our calculations because it is the lowest energy quintet state.

Recently, Nozawa *et al.* performed a time-resolved XAS measurement on $[Fe(II)(phen)_3]^{2+}$ revealing simultaneous changes in the pre-edge, near edge and EXAFS regions of the spectrum.[25] Static spectra of the pre-edge region of $[Fe(II)(phen)_3]^{2+}$ and $[Fe(II)(2\text{-}CH_3\text{-}phen)_3]^{2+}$ closely resemble the pre-edge features shown in Figure 2.2b. The transient spectrum revealed a bleach in the pre-edge region centered at the energy of the peak in the low-spin ground state of $[Fe(II)(phen)_3]^{2+}$ Nozawa *et al.* analyzed the pre-edge region of their spectra using ligand field theory. Our results above show that *ab initio* DFT calculations provide a tool to extract information about the spin state and symmetry of the molecule in the excited state and we show that there may be significant deviations from the ligand field picture of the pre-edge region when the complexes are not perfectly octahedral. The work by Nozawa confirms that time-resolved iron K-edge XAS measurements should focus on the pre-edge region, in addition to, the XANES and EXAFS regions to probe simultaneously electronic and nuclear degrees of freedom.

Our study has focused on extracting information about electronic structural changes in equilibrium and transient spin cross-over complexes using the Fe K-edge. A more direct spectroscopic approach to probe the vacant 3d orbitals or iron complexes is via iron L-edge XAS. Huse *et al.* have used time-resolved picosecond and femtosecond iron L-edge XAS to probe the low- to high-spin conversion in $[Fe(tren(py)_3)](PF_6)_2$.[15,16] They were able to determine the ligand field splitting energies for the LS and transient HS complexes, and identify a decrease in π-backbonding using a charge-transfer multiplet model to interpret their time-resolved data.

The empirical multiplet analysis assumes an octahedral symmetry for the molecule. Our calculations have shown that there is a significant distortion in the octahedral symmetry of the molecule during the SCO process. While there are a number of studies where *ab initio* methods have been used to simulate transition metal L-edge spectroscopies,[78,79] these methods are not commonly available in electronic structure codes. Our study of the Fe K-edge highlights the need for *ab initio* approaches to simulating time-resolved L-edge spectra of Fe(II) compounds.

As advances are made in experimental techniques in X-ray science, it will be possible to perform experiments with higher time resolution (sub 10 fs) across the soft and hard X-ray region. In order to simulate these experiments, techniques must be developed that can simulate the X-ray absorption spectra of dynamic molecular systems. In the case of photoinduced charge transfer processes, several *ab initio* methods have been developed to generate localized diabatic states to describe charge transfer reactions.[80,81] For example, Van Voorhis and co-workers have developed the constrained DFT (C-DFT) methodology which allows them to compute an optimized wave function for a charge transfer state.[81] It would be possible to use either TP- or TDDFT to simulate the X-ray absorption of a charge transfer state prepared by C-DFT. An alternative approach would be to use explicitly time dependent techniques to simulate interactions of molecules with electrical fields in real-time. Recently, it was shown that real-time approaches to density functional theory can model doubly excited electronic states.[82] Presumably, one could use such an approach to model simultaneously excited valence and core states while also including the effects of nuclear dynamics.

Summary

We have simulated the X-ray absorption spectra of a family of ground and excited state Fe(II) SCO complexes using two different approaches based on density functional theory. We have

extended the TPDFT methodology to simulate the K-edge X-ray absorption of transition metal complexes. This method has yielded promising results, and shows that there is an MO based approach that can be used to simulate the XANES region of transition-metal K-edge X-ray absorption spectra. This method was able to simulate pre-edge, near edge, and multiple scattering features. Thus, it provides an approach that is sensitive to both the geometric and electronic configuration of the molecule. We believe that, with further calibration, this method could be generally applicable to transition metal K-edges. We also used TDDFT to simulate the pre-edge region of the spectrum where we focused on the electronic structural information contained in the individual transitions contributing to the pre-edge features.

This study identifies some important aspects of the photoinduced SCO process in $[Fe(tren(py)_3]^{2+}$. Firstly, it is accompanied by a large asymmetric lengthening of the metal-ligand bonds. The geometric change is coupled to changes in the electronic structure that are evident in the pre- and near-edge regions of the spectrum. The change in spin state is evident in the pre-edge region of the X-ray absorption where the single feature present in the LS case is replaced by two peaks in the HS spectrum. The dipole contribution to the pre-edge spectrum of the LS complex provides evidence of π-backbonding. In the HS spectra there is less π-backbonding, but decreases in symmetry provide dipole strength to transitions to the e_g orbitals. TD-DFT simulations have revealed a decrease in π backbonding with the SCO transition. Lastly, the TD-DFT simulations allowed us to estimate the ligand field splitting in the high-spin complexes.

Despite our simulations identifying a significant change in the pre-edge region, this was not observed in the transient X-ray experiment of Khalil *et al*. due to low X-ray photon flux and poor spectral resolution. The recent experiment of Nozawa *et al.* shows that changes in the pre-edge region can be resolved in time-resolved XAS measurements of SCO complexes. Further

technological advances in time-resolved X-ray experimental set-ups combined with the development of new fourth generation X-ray light sources will be able to detect small changes across the entire X-ray absorption spectrum. We anticipate that time-resolved XAS coupled with *ab initio* simulations will reveal detailed molecular information about the ultrafast coupled motion of electrons and nuclei in solution.

References

(1)McCusker, J. *Accounts Chem. Res.* **2000**, *36*, 876.

(2)Schoenlein, R. W.; Chattopadhyay, S.; Chong, H. H. W.; Glover, T. E.; Heimann, P. A.; Shank, C. V.; Zholents, A. A.; Zolotorev, M. S. *Science* **2000**, *287*, 2237.

(3)Saes, M.; Bressler, C.; van Mourik, F.; Gawelda, W.; Kaiser, M.; Chergui, M.; Bressler, C.; Grolimund, D.; Abela, R.; Glover, T. E.; Heimann, P. A.; Schoenlein, R. W.; Johnson, S. L.; Lindenberg, A. M.; Falcone, R. W. *Rev. Sci. Instrum.* **2004**, *75*, 24.

(4)Benesch, F.; Lee, T. W.; Jiang, Y.; Rose-Petruck, C. G. *Opt. Lett.* **2004**, *29*, 1028.

(5)Chen, L. X. *J. Electron Spectrosc.* **2001**, *119*, 161.

(6)Bressler, C.; Chergui, M. *Chem.l Rev.* **2004**, *104*, 1781.

(7)Bressler, C.; Chergui, M. *Annu. Rev. Phys. Chem.* **2010**, *61*, 263.

(8)Chen, L. X. *Angew. Chem. Int. Edit.* **2004**, *43*, 2886.

(9)Chen, L. X. *Annu. Rev. Phys. Chem.* **2005**, *56*, 221.

(10) Chen, L. X.; Zhang, X.; Lockard, J. V.; Stickrath, A. B.; Attenkofer, K.; Jennings, G.; Liu, D. J. *Acta Crystallogr. A* **2010**, *A66*, 240.

(11) Bressler, C.; Milne, C.; Pham, V. T.; ElNahhas, A.; van der Veen, R. M.; Gawelda, W.; Johnson, S.; Beaud, P.; Grolimund, D.; Kaiser, M.; Borca, C. N.; Ingold, G.; Abela, R.; Chergui, M. *Science* **2009**, *323*, 489.

(12) Gawelda, W.; Pham, V.-T.; Benfatto, M.; Zaushitsyn, Y.; Kaiser, M.; Grolimund, D.; Johnson, S. L.; Abela, R.; Hauser, A.; Bressler, C.; Chergui, M. *Phys. Rev. Lett.* **2007**, *98*, 057401/1.

(13) Saes, M.; Bressler, C.; Abela, R.; Grolimund, D.; Johnson, S.; Heimann, P.; Chergui, M. *Phys. Rev. Lett.* **2003**, *90*.

(14) van der Veen, R. M.; Milne, C. J.; El Nahhas, A.; Lima, F. A.; Pham, V.-T.; Best, J.; Weinstein, J. A.; Borca, A. N.; Abela, R.; Bressler, C.; Chergui, M. *Angew. Chem., Int. Ed.* **2009**, *48*, 2711.

(15) Huse, N.; Cho, H.; Hong, K.; Jamula, L.; de Groot, F. M. F.; Kim, T. K.; McCusker, J. K.; Schoenlein, R. W. *J. Phys. Chem. Lett.* **2011**, *2*, 880.

(16) Huse, N.; Kim, T. K.; Jamula, L.; McCusker, J. K.; de Groot, F. M. F.; Schoenlein, R. W. *J. Am. Chem. Soc.* **2010**, *132*, 6809.

(17) Khalil, M.; Marcus, M. A.; Smeigh, A. L.; McCusker, J. K.; Chong, H. H. W.; Schoenlein, R. W. *J. Phys. Chem. A* **2006**, *110*, 38.

(18) Chen, L. X.; Jaeger, W. J. H.; Jennings, G.; Gosztola, D. J. *Science* **2001**, *292*, 262.

(19) Chen, L. X.; Jennings, G.; Liu, T.; Gosztola, D. J.; Hessler, J. P.; Scaltrito, D. V.; Meyer, G. J. *J. Am. Chem. Soc.* **2002**, *124*, 10861.

(20) Chen, L. X.; Shaw, G. B.; Novozhilova, I.; Liu, T.; Jennings, G.; Attenkofer, K.; Meyer, G. J.; Coppens, P. *J. Am. Chem. Soc.* **2003**, *125*, 7022.

(21) Chen, L. X.; Zhang, X.; Wasinger, E. C.; Attenkofer, K.; Jennings, G.; Muresan, A. Z.; Lindsey, J. S. *J. Am. Chem. Soc.* **2007**, *129*, 9616.

(22) Zhang, X.-Y.; Smolentsev, G.; Guo, J.-C.; Attenkofer, K.; Kurtz, C.; Jennings, G.; Lockard, J. V.; Stickrath, A. B.; Chen, L.-X. *J. Phys. Chem. Lett.* **2011**, *2*, 628.

(23) Lee, T.; Jiang, Y.; Rose-Petruck, C. G.; Benesch, F. *J. Chem. Phys.* **2005**, *122*, 084506/1.

(24) Ahr, B.; Chollet, M.; Adams, B.; Lunny, E. M.; Laperle, C. M.; Rose-Petruck, C. *Phys. Chem. Chem. Phys.* **2011**, *13*, 5590.

(25) Nozawa, S.; Sato, T.; Chollet, M.; Ichiyanagi, K.; Tomita, A.; Fujii, H.; Adachi, S.-i.; Koshihara, S.-y. *J. Am. Chem. Soc.* **2010**, *132*, 61.

(26) Chen, J.; Zhang, H.; Tomov, I. V.; Ding, X.; Rentzepis, P. M. *Proc. Natl. Acad. Sci. U. S. A.* **2008**, *105*, 15235.

(27) Hillyard, P. W.; Kuchibhatla, S.; Glover, T. E.; Hertlein, M. P.; Huse, N.; Nachimuthu, P.; Saraf, L. V.; Thevuthasan, S.; Gaffney, K. J. *Phys. Rev. B* **2009**, *80*.

(28) Briois, V.; Sainctavit, P.; Long, G. J.; Grandjean, F. *Inorg. Chem.* **2001**, *40*, 912.

(29) Westre, T. E.; Kennepohl, P.; DeWitt, J. G.; Hedman, B.; Hodgson, K. O.; Solomon, E. I. *J. Am. Chem. Soc.* **1997**, *119*, 6297.

(30) Pandey, R. K.; Mukamel, S. J. *Phys. Chem. A* **2007**, *111*, 805.

(31) Koningsberger, D. C.; Prins, R. *X-ray Absorption: Principles, Applications, Techniques of EXAFS, SEXAFS and XANES*; John Wiley & Sons: New York, 1988; Vol. 92.

(32) Gütlich, P.; Goodwin, H. A. *Spin Crossover In Transition Metal Compounds. 1-III*; New York: Berlin, 2004.

(33) Monat, J. E.; McCusker, J. K. *J. Am. Chem. Soc.* **2000**, *122*, 4092.

(34) Cannizzo, A.; Milne, C. J.; Consani, C.; Gawelda, W.; Bressler, C.; van Mourik, F.; Chergui, M. *Coord. Chem. Rev.* **2010**, *254*, 2677.

(35) Wolf, M. M. N.; Groß, R.; Schumann, C.; Wolny, J. A.; Schünemann, V.; Døssing, A.; Paulsen, H.; McGarvey, J. J.; Diller, R. *Phys. Chem. Chem. Phys.* **2008**, *10*, 4264.

(36) Lawson Daku, L. M.; Hauser, A. *J. Phys. Chem. Lett.* **2010**, *1*, 1830.

(37) Huse, N.; Khalil, M.; Kim, T. K.; Smeigh, A. L.; Jamula, L.; McCusker, J. K.; Schoenlein, R. W. *J. Phys.: Conf. Ser.* **2009**, *148*.

(38) Smeigh, A. L.; Creelman, M.; Mathies, R. A.; McCusker, J. K. *J. Am. Chem. Soc.* **2008**, *130*, 14105.

(39) Gutlich, P.; Goodwin, H. A. Spin crossover - An overall perspective. In *Spin Crossover In Transition Metal Compounds I*; Springer-Verlag Berlin: Berlin, 2004; Vol. 233; pp 1.

(40) Brady, C.; Callaghan, P. L.; Ciunik, Z.; Coates, C. G.; Dossing, A.; Hazell, A.; McGarvey, J. J.; Schenker, S.; Toftlund, H.; Trautwein, A. X.; Winkler, H.; Wolny, J. A. *Inorg. Chem.* **2004**, *43*, 4289.

(41) Adamo, C.; Barone, V. *J. Chem. Phys.* **1999**, *110*, 6158.

(42) Hehre, W. J.; Ditchfield, R.; Pople, J. A. *J. Chem. Phys.* **1972**, *56*, 2257.

(43) Rassolov, V. A.; Pople, J. A.; Ratner, M. A.; Windus, T. L. *J. Chem. Phys.* **1998**, *109*, 1223.

(44) Pierloot, K.; Vancoillie, S. *J. Chem. Phys.* **2006**, *125*, 124303.

(45) Pierloot, K.; Vancoillie, S. *J. Chem. Phys.* **2008**, *128*, 034104.

(46) Tomasi, J.; Mennucci, B.; Cammi, R. *Chem. Rev.* **2005**, *105*, 2999.

(47) M. J. Frisch; G. W. Trucks; H. B. Schlegel; G. E. Scuseria; M. A. Robb; J. R. Cheeseman; G. Scalmani; V. Barone; B. Mennucci; G. A. Petersson; H. Nakatsuji; M. Caricato; X. Li; H. P. Hratchian; A. F. Izmaylov; J. Bloino; G. Zheng; J. L. Sonnenberg; M. Hada; M. Ehara; K. Toyota; R. Fukuda; J. Hasegawa; M. Ishida; T. Nakajima; Y. Honda; O. Kitao; H. Nakai; T. Vreven; J. A. Montgomery, J.; J. E. Peralta; F. Ogliaro; M. Bearpark; J. J. Heyd; E. Brothers; K. N. Kudin; V. N. Staroverov; R. Kobayashi; J. Normand; K. Raghavachari; A. Rendell; J. C. Burant; S. S. Iyengar; J. Tomasi; M. Cossi; N. Rega; J. M. Millam; M. Klene; J. E. Knox; J. B. Cross; V. Bakken; C. Adamo; J. Jaramillo; R. Gomperts; R. E. Stratmann; O. Yazyev; A. J. Austin; R. Cammi; C. Pomelli; J. W. Ochterski; R. L. Martin; K. Morokuma; V. G.

Zakrzewski; G. A. Voth; P. Salvador; J. J. Dannenberg; S. Dapprich; A. D. Daniels; Ö. Farkas; J. B. Foresman; J. V. Ortiz; J. Cioslowski; Fox, D. J. *Gaussian 09, Revision A.1,* ; Gaussian, Inc.: Wallingford, CT, 2009.

(48) Triguero, L.; Pettersson, L.; Ågren, H. *Phys. Rev. B* **1998**; *58*; 8097.

(49) K. Hermann; L.G.M. Pettersson; M.E. Casida; C. Daul; A. Goursot; A. Koester; E. Proynov; A. St-Amant; Salahub., D. R. StoBe-deMon version 3.0, 2009.

(50) Slater, J. C. *Adv. Quantum Chem.*; **1972**; *6*; 1.

(51) Becke, A. D. *Phys. Rev. A* **1988**, *38*, 3098.

(52) Perdew, J. P. *Phys. Rev. B* **1986**, *33*, 8822.

(53) Wachters, A. J. H. *J. Chem. Phys.* **1970**, *52*, 1033.

(54) Ågren, H.; Carravetta, V.; Vahtras, O.; Pettersson, L. G. M. *Chem. Phys. Lett.* **1994**, *222*, 75.

(55) Hirata, S.; Head-gordon, M. *Chem. Phys. Lett.* **1999**, 291.

(56) DeBeer George, S.; Petrenko, T.; Neese, F. *J. Phys. Chem. A* **2008**, *112*, 12936.

(57) DeBeer George, S.; Petrenko, T.; Neese, F. *Inorg. Chim. Acta* **2008**, *361*, 965.

(58) Weigend, F.; Ahlrichs, R. *Phys. Chem. Chem. Phys.* **2005**, *7*, 3297.

(59) Neese, F. *Inorg. Chim. Acta* **2002**, *337*, 181.

(60) Neese, F.; Wennmohs, F.; Hansen, A.; Becker, U. *Chem. Phys.* **2009**, *356*, 98.

(61) Klamt, A.; Schueuermann, G. *J. Chem. Soc., Perkin Trans. 2* **1993**, 799.

(62) Boubekeur, K.; Deroche, A.; Lambert, F.; Morgensternbadarau, I. *Acta Crystallogr. C* **1995**, *51*, 2244.

(63) Hoselton, M. A.; Wilson, L. J.; Drago, R. S. *J. Am. Chem. Soc.* **1975**, *97*, 1722.

(64) Delker, G. L. Temperature Dependent Studies on Structural and Electronic Effects in Single Crystals, University of Illinois, 1976.

(65) Risberg, E. D.; Jalilehvand, F.; Leung, B. O.; Pettersson, L. G. M.; Sandstrom, M. *Dalton T.* **2009**, 3542.

(66) Leetmaa, M.; Ljungberg, M. P.; Lyubartsev, A.; Nilsson, A.; Pettersson, L. G. M. *J. Electron Spectrosc.* **2010**, *177*, 135.

(67) Varetto, U. MOLEKEL 5.4 Swiss National Supercomputing Centre: Manno (Switzerland).

(68) Wilson, L. J.; Georges, D.; Hoselton, M. A. *Inorg. Chem.* **1975**, *14*, 2968.

(69) Mayer, I. *Chem. Phys. Lett.* **1983**, *97*, 270.

(70) Dreuw, A.; Head-Gordon, M. *Chem. Rev.* **2005**, *105*, 4009.

(71) Briois, V.; Moulin, C. C. D.; Sainctavit, P.; Brouder, C.; Flank, A. M. *J. Am. Chem. Soc.* **1995**, *117*, 1019.

(72) Ankudinov, A. L.; Ravel, B.; Rehr, J. J.; Conradson, S. D. *Phys. Rev. B* **1998**, *58*, 7565.

(73) Benfatto, M.; Congiu-Castellano, A.; Daniele, A.; Della Longa, S. *J. Synchrotron Radiat.* **2001**, *8*, 267.

(74) Rehr, J. J.; Ankudinov, A. L. *Coord. Chem. Rev.* **2005**, *249*, 131.

(75) de Groot, F. M. F. *Coord. Chem. Rev.* **2005**, *249*, 31.

(76) Debeer George, S.; Neese, F. *Inorg. Chem.* **2010**, *49*, 1849.

(77) Campbell, L.; Mukamel, S. *J. Chem. Phys.* **2004**, *121*, 12323.

(78) Kruger, P.; Natoli, C. R. *Phys. Rev. B* **2004**, *70*, 245120.

(79) Ikeno, H.; Mizoguchi, T.; Tanaka, I. *Phys. Rev. B* **2011**, *83*, 155107.

(80) Subotnik, J. E.; Yeganeh, S.; Cave, R. J.; Ratner, M. A. *J. Chem. Phys.* **2008**, *129*, 244101/1.

(81) Van Voorhis, T.; Kowalczyk, T.; Kaduk, B.; Wang, L.-P.; Cheng, C.-L.; Wu, Q. *Annu. Rev. Phys. Chem.* **2010**, *61*, 149.

(82) Isborn, C. M.; Li, X. *J. Chem. Phys.* **2008**, *129*, 204107/1.

Chapter 3

Simulating Ru L_3-edge X-ray Absorption Spectroscopy with Time-Dependent Density Functional Theory: Model Complexes and Electron Localization in Mixed-Valence Metal Dimers

This work has previously been published in the following article:

Van Kuiken, B. E.; Valiev, M.; Daifuku, S. L.; Bannan, C.; Strader, M. L.; Cho, H.; Huse, N.; Schoenlein, R. W.; Govind, N.; Khalil, M. "Simulating Ru L_3-edge X-ray Absorption Spectroscopy with Time-Dependent Density Functional Theory: Model Complexes and Electron Localization in Mixed-Valence Metal Dimers," *J. Phys. Chem. A* **2013**, *117,* 4444.

Ruthenium L_3-edge X-ray absorption (XA) spectroscopy probes unoccupied 4d orbitals of the metal atom and is increasingly being used to interrogate the local electronic structure in ground and excited electronic states of Ru complexes. The simultaneous development of computational tools for simulating Ru L_3-edge spectra is crucial for interpreting the spectral features at a molecular level. This study demonstrates that time-dependent density functional theory (TDDFT) is a viable and predictive tool for simulating Ruthenium L_3-edge XA spectroscopy. We systematically investigate the effects of exchange correlation functional and implicit and explicit solvent interactions on a series of Ru^{II} and Ru^{III} complexes in their ground and electronic excited states. The TDDFT simulations reproduce all the experimentally observed features in Ru L_3-edge XA spectra within the experimental resolution (0.4 eV). Our simulations identify

ligand- specific charge transfer features in complicated Ru L_3-edge spectra of $[Ru(CN)_6]^{4-}$ and Ru^{II} polypyridyl complexes illustrating the advantage of using TDDFT in complex systems. We conclude that the B3LYP functional most accurately predicts the transition energies of charge transfer features in these systems. We use our TDDFT approach to simulate experimental Ru L_3-edge XA spectra of transition metal mixed-valence dimers of the form $[(NC)_5M^{II}\text{-}CN\text{-}Ru^{III}(NH_3)_5]^-$ (where M = Fe or Ru) dissolved in water. Our study determines the spectral signatures of electron delocalization in Ru L_3-edge XA spectra. We find that the inclusion of explicit solvent molecules is necessary for reproducing the spectral features and the correct valencies in these mixed-valence complexes. This study validates the use of TDDFT for simulating Ru 2p excitations using popular quantum chemistry codes and providing a powerful interpretive tool for equilibrium and ultrafast Ru L_3-edge x-ray spectroscopy.

3.1. Introduction

The structure, bonding, redox and excited state properties of Ruthenium complexes have been widely studied in recent years due to their applications as dye molecules for solar energy conversion and catalysts for efficient water splitting.[1-3] In each of these energy conversion applications it has been shown that the electronic structure of the Ru complex critically influences its function. It has become increasingly important to develop experimental probes capable of tracking the rearrangements of 4d electrons with high spatial and temporal resolution in the ground and excited electronic states of Ru complexes. Ru L-edge X-ray absorption (XA) spectroscopy is dominated by excitations from Ru 2p orbitals to unoccupied orbitals with Ru 4d character and is a sensitive tool for understanding the detailed electronic structure of Ru compounds in disordered media. Recent equilibrium Ru L-edge XA measurements have investigated the electronic structure of water oxidation catalysts and enzyme mimics in the

ground electronic state.[4,5] Picosecond Ru L-edge XA spectroscopy has been used to characterize the transient excited states of Ru^{II} polypyridine complexes relevant to solar energy conversion.[6-8]

The interpretation of Ru L-edge XA spectra at a molecular level requires detailed simulations which relate the observed spectral features to the molecular electronic structure around the Ru atom. The most widely used approach for simulating the L-edges of molecular and solid state systems has been the semi-empirical charge transfer multiplet (CTM) method developed by de Groot and coworkers and distributed as the CTM4XAS software package.[9] For Ru, this approach would treat only the 2p and 4d electrons explicitly by forming $2p^6 4d^N$ ground states and $2p^5 4d^{N+1}$ core-excited states from ligand field theory. The effects of covalent metal–ligand interactions that give rise to charge transfer (CT) features in L-edge XA spectra are accounted for by considering $4d^{N-1}L^1$ and $4d^{N+1}L^{-1}$ configurations in the valence space. These simulations require user input of ligand field parameters (such as Δ_0 for O_h symmetry), scaling factors by which Slater integrals and spin–orbit coupling differ from atomic values, and charge transfer energies for each system. Moreover, CTM calculations become quite complicated for low symmetry molecules where many ligand field and charge transfer parameters would be required. While these calculations provide great insight and offer a direct connection to ligand field models widely used in inorganic chemistry, they fail to be predictive because a new set of parameters is needed for each molecule. Consequently, it is desirable to have first principles quantum chemical tools that can interpret and predict L-edge XA spectroscopy.

Several recent papers have successfully simulated the Ru $L_{2,3}$-edge spectra of Ru complexes in solution by employing a molecular orbital approximation for core excitations.[4,10] The orbitals used to determine the excitation energies and transition dipole moments are ground state relativistic spinor orbitals. This approximation has been quite successful in simulating the

spectra of $[Ru(NH_3)_6]^{3+}$ and *cis,cis*-$[Ru_2O(OH_2)_2(bpy)_4]^{4+}$ called the "blue dimer." The disadvantage of this method is that it completely ignores final state effects, and relies on the orbital energy differences to give the excitation energies. The Z+1 approximation has been used with spin-free orbitals to simulate the L-edge spectra of $[Ru(bpy)_3]^{2+}$.[11] While this approach includes final state effects, it has been shown to worsen agreement with experiment in some cases.[10] Finally, we note that there are a number of other methods rooted in relativistic quantum chemistry that could potentially be used to simulate Ru L-edge XA spectra. These include the 4-component static exchange (STEX) approximation,[12] the *ab initio* multiplet method,[13] and relativistic TDDFT.[14-16] The disadvantages of these approaches may include the complexity and computational cost of 4-component calculations, reliance on HF theory, or implementations that are limited to closed-shell systems. Consequently, it is desirable to have a computational tool that is predictive and widely available.

In several recent works time-dependent density functional theory (TDDFT) has been employed to simulate Ru L_3-edge XA spectroscopy and has successfully reproduced all spectral features observed experimentally.[7,10,17] However, a comprehensive study of how various simulation parameters affect the spectral features in the computed spectra is lacking. The goal of the present work is to provide a detailed characterization of applying TDDFT to simulate Ru L_3-edge XA spectroscopy. We begin by explaining that the effects of spin-orbit coupling (SOC) on the L_3-edges of Ru complexes are small compared to natural and experimental line broadening, which justifies the use of our spin-free (no SOC) TDDFT-based protocol for simulating Ru L_3-edge XA spectroscopy. We find that our computed spectra for a series of Ru^{II} and Ru^{III} complexes predict the experimental peak positions with a typical deviation of 0.26 eV. From these results, recommended simulation parameters are discussed and the importance of choosing

an appropriate exchange–correlation (XC) functional for the prediction of CT features is emphasized. In the context of this work, we adopt the language of transition metal L-edge spectroscopy where spectral features arising from the overlap of metal and ligand orbitals are termed CT features. Finally, the measured and simulated Ru L_3-edge XA spectra of mixed-valence transition metal complexes of the form, $[(NC)_5M^{II}\text{-}CN\text{-}Ru^{III}(NH_3)_5]^-$ where M = Fe and Ru (denoted $Fe^{II}Ru^{III}$ and $Ru^{II}Ru^{III}$), are presented. The XA spectra are consistent with localized charges on the metals. We discuss the importance of solvent models for understanding properties of transition metal complexes in solution, and we use explicit solvent models to show that the hydrogen bonding environment strongly stabilizes the $Fe^{II}Ru^{III}$ and $Ru^{II}Ru^{III}$ oxidations states. The mixed valence simulations highlight the predictive power of our approach for cases involving multiple metal centers and deviations from ideal symmetry.

3.2. Experimental Methods

$Ru(NH_3)_6Cl_3$ and $K_4Ru(CN)_6$ were purchased from Sigma Aldrich and used without further purification. $Fe^{II}Ru^{III}$ and $Ru^{II}Ru^{III}$ were prepared as their sodium salts according to literature methods and purified using a BioGel P2 column to remove starting materials from samples.[18] Samples for XA measurements were prepared by dissolving the molecules in water.

The XA measurements of $Ru(NH_3)_6Cl_3$, $K_4Ru(CN)_6$, $NaFe^{II}Ru^{III}$, and $NaRu^{II}Ru^{III}$ were performed on beamline 6.0.1 at the Advanced Light Source at Lawrence Berkeley National Laboratory. This beamline is equipped with a double crystal (Si) monochromator delivering monochromatic X-rays with ~0.4 eV resolution at the Ru L_3-edge (2840 eV). XA measurements were performed by monitoring the transmission of the X-rays through a ~100 μm film of the sample produced by the wire-guided jet in a helium atmosphere. This allowed the sample to be

flowed continuously preventing X-ray damage. The monochromator energy was calibrated using the published data for $Ru(bpy)_3Cl_2$.[6]

3.3. Computational Methods

Geometry optimizations for all single valence molecules was performed with the ORCA quantum chemistry package.[19] Molecular geometries were optimized using the B3LYP functional.[20,21] The def2-SV(P) basis set was used for the ligands and the def2-SVP basis was used for Ru with the associated ECP.[22] The conductor-like screening model (COSMO) was used to model the solvent (ε = 80.4 and n = 1.33) environment and stabilize the anions.[23] The geometries of the $N3^{4-}$ dye were taken from our previous work.[7]

In the mixed quantum and molecular mechanical (QM/MM) simulations, the mixed-valence complexes comprised the QM region, and the solvent made up the MM region. The PBE0 functional was used for optimizations in the QM region.[24] It is noted that the use of PBE0 instead of B3LYP should not introduce significant systematic differences as both give reasonable geometric parameters for transition metal complexes. The 6-31G* basis set ligand atoms, and the Stuttgart/Dresden ECPs were used for Ru and Fe in conjunction with the standard double zeta basis sets.[25] $Fe^{II}Ru^{III}$ and $Ru^{II}Ru^{III}$ complexes were placed in 3 nm cubic solvent boxes with periodic boundary conditions and the SPC/E water model was used.[26] Following the initial solvation of the complexes, the MM region was optimized, and then the solvent was equilibrated for 100 ps. A constant temperature ensemble at 298.15 K was employed with a Berendsen thermostat.[27] The cutoff for electrostatic interactions was 1.5 nm. During the equilibration step, the QM solute was fixed and represented by a set of atom-centered point charges determined by fitting the electrostatic potential of the solute. The final configuration from the equilibration was taken, and a QM/MM optimization was performed. The latter

involves relaxation of both quantum and classical regions. The optimized geometry was used to calculate the X-ray spectra of the mixed-valence species. Within harmonic approximation of solute—solvent fluctuations such an approach typically provides reasonable values for the maxima of the absorption bands. More accurate calculation would involve full sampling of the entire system at finite temperature, but would be computationally prohibitive at this point. All QM/MM calculations were performed with NWChem.[28]

Linear-response TDDFT calculations were performed to model the Ru L_3-edge XA spectra by only looking for solutions to the TDDFT eigenvalue problem which involved single particle excitations from molecular orbitals with Ru 2p character. Scalar relativistic effects were accounted for by the second order Douglass-Kroll-Hess (DKH) Hamiltonian as implemented in ORCA.[29] The COSMO was used in all TDDFT calculations performed with ORCA. We note that effect of the continuum solvent on the excitation energies was insignificant. For XA calculations the def2-SV(P) was used for ligand atoms, and the def2-TZVP basis set was used for Fe. The SARC variant of these basis sets was used.[30] The all-electron Sapporo-DK-TZP basis was used for the Ru atom,[31] but the *g* functions were removed from this basis greatly increasing the stability of the SCF iterations. All of these basis sets have been optimized for use with relativistic Hamiltonians. The impact of XC functional on Ru L_3-edge XA spectra will be discussed in detail below. For the purposes of this study we have investigated the pure DFT functional BP.[32,33] In addition, we investigated the TPSSh,[34] O3LYP,[35] B3LYP, and PBE0 functionals, which contain 10, 11.6, 20, and 25% HF exchange, respectively. TDDFT calculations were also performed using the QM/MM framework by including all classical point charges, and the restricted energy window (REW) approach recently implemented in NWChem.[17] These calculations employed the zeroth-order regular approximation (ZORA) to

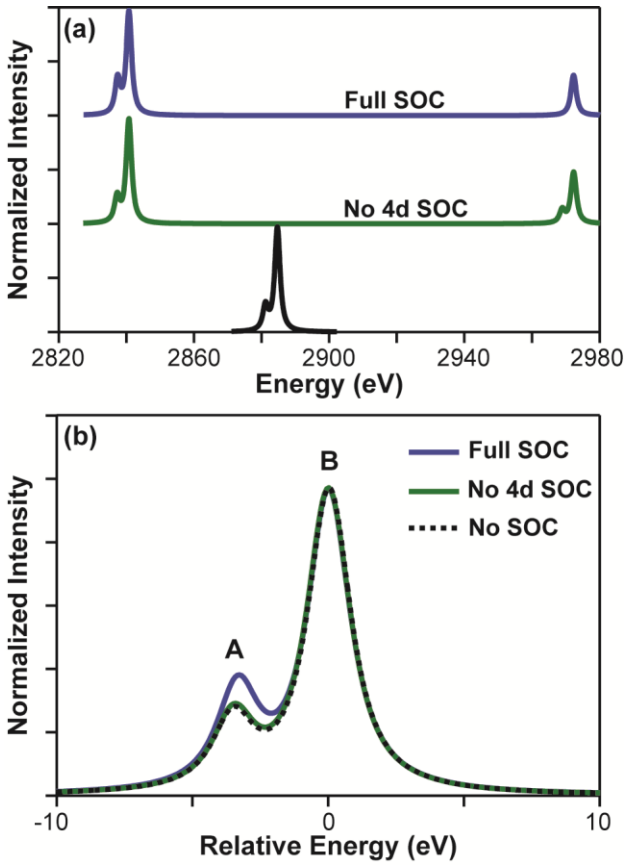

Figure 3.1. Ligand field multiplet calculations for an octahedral Ru^{III} complex with $\Delta_0 = 3.5$ eV. The Slater integrals have been reduced to 25% of their atomic values. Spectra are shown for the L-edges arising from excitations from the 2p orbitals for three cases: full atomic SOC in the 2p and 4d orbitals (blue curves), no 4d SOC (green curves), and complete neglect of SOC (black curves). Figure 3.1(a) shows complete spectra while 3.1(b) compares the lineshapes of the L_3-edges for each of the cases described above where feature B is centered at 0 eV. All spectra have been normalized to the intensity of the largest feature.

account for scalar relativistic effects.[36,37] We note that the same basis sets and energy shifts (listed in Table 3.3) are applied for ZORA results. Spectral profiles for all simulated spectra are generated by convoluting the discrete excitations with Voigt profiles with natural (Lorentzian) and instrument (Gaussian) widths of 1.75 eV and 0.4 eV, respectively.

3.4. Results and Discussion

3.4.1 L-edge spectroscopy of Ru complexes: spin–orbit and multiplet effects

Figure 3.1 demonstrates the effects of SOC on Ru $L_{2,3}$-edge spectra. It shows three ligand field multiplet simulations of Ru L_3-edge spectra for an octahedral Ru^{III} (d^5) complex with $\Delta_0 = 3.5$ eV. The three cases considered are: (i) inclusion of the atomic values of 2p and 4d SOC (blue traces), (ii) neglect of 4d SOC (green traces), and (iii) complete neglect of all SOC (solid and dotted black lines). Figure 3.1a shows the full L-edge spectrum arising from excitations involving the 2p orbitals. In the cases with 2p SOC included (blue and green), there are features near 2840 and 2970 eV defined as the L_3- and L_2-edges. These features arise from $2p_{3/2} \rightarrow$ 4d and $2p_{1/2} \rightarrow$ 4d transitions, respectively. In the case of no SOC there is only a single feature arising from the Ru 2p → 4d transitions.

Figure 3.1b compares the L_3-edge spectra for the cases including 2p SOC with the spin-free simulation. This absorption edge contains two features labeled A and B. Since this is an octahedral complex, the Ru 4d orbitals will be split into t_{2g} end e_g orbitals by the ligand field with a low-spin $(t_{2g})^5(e_g)^0$ configuration. The allowed transitions at the Ru L_3-edge become $2p_{3/2} \rightarrow t_{2g}$ and $2p_{3/2} \rightarrow e_g$ for features A and B, respectively. The neglect of only 4*d* SOC results in a shift of –0.2 eV and a decrease in the relative intensity of the A feature arising from $2p_{3/2} \rightarrow t_{2g}$ transition. This has also been predicted for the Ru L-edge spectra of $[Ru(NH_3)_6]^{3+}$.[38] It is noted that the atomic SOC value has a greater magnitude than the ~0.1 eV extracted from experimental data.[39] The spin-free spectrum is nearly indistinguishable from the case where only 4d SOC has been neglected. The similarity between the spin-free spectrum and the L_3-edges of spectra that include 2p SOC can be understood in terms of the selection rules of atomic spectroscopy. In the presence of SOC, one can consider the 4d orbitals to have either $4d_{5/2}$ (t_{2g}) or $4d_{3/2}$ (e_g) character. Transitions from the $2p_{3/2}$ level are allowed to each of the d orbitals by a $\Delta J = 0, \pm 1$ dipole

selection rule.[39] In the case where SOC and configuration interaction are ignored, this reduces to the familiar $\Delta l = \pm 1$ dipole selection rule where $p \rightarrow d$ transitions are allowed. It should be noted that the effects of SOC are more pronounced at the L_2-edge. It is well documented that $2p_{1/2} \rightarrow t_{2g}$ ($4d_{5/2}$) transitions are dipole forbidden in octahedral complexes.[38,39] This is evident in Figure 3.1a where the L_2-edge contains a single feature when 4d SOC is included (blue curve), but two features are present when 4d SOC is ignored (green curve). Additionally, the intensity branching ratios of the L-edges (defined as the ratio of the L_3-edge intensity to the total L-edge intensity) depend strongly on SOC and many-electron effects.[40] While we don't suggest that the L_2-edge should be ignored, we argue that much of the chemically relevant information contained in Ru L-edge XA spectroscopy can be extracted from the L_3-edge.

It is also important to consider the magnitude of multiplet effects in Ru L-edge XA spectroscopy. The overlap of 2p and valence d electrons show strong exchange interactions between ground and core-excited wave functions in transition metal complexes. As a result satellite features appear in L-edge spectra, and this phenomenon has been termed the multiplet effect. While multiplet effects typically dominate the 2p spectra of 3d transition metal complexes, the overlap of 2p and 4d orbital in Ru is small which diminishes these effects in Ru L-edge XA spectra.[41] Moreover, the 2p SOC in Ru complexes is large preventing the mixing of L_3- and L_2-edges. Recent single particle calculations discussed in Section 3.4.6 suggest that final state effects are relatively weak in Ru L_3-edge spectroscopy.[4] Based on the above discussion, we expect spin-free TDDFT to duplicate all of the experimentally resolved fine structure in Ru L_3-edge XA spectroscopy and provide a molecular level description of the various spectral features. These assumptions should also hold for other 4d metals and molecules that deviate from octahedral symmetry.

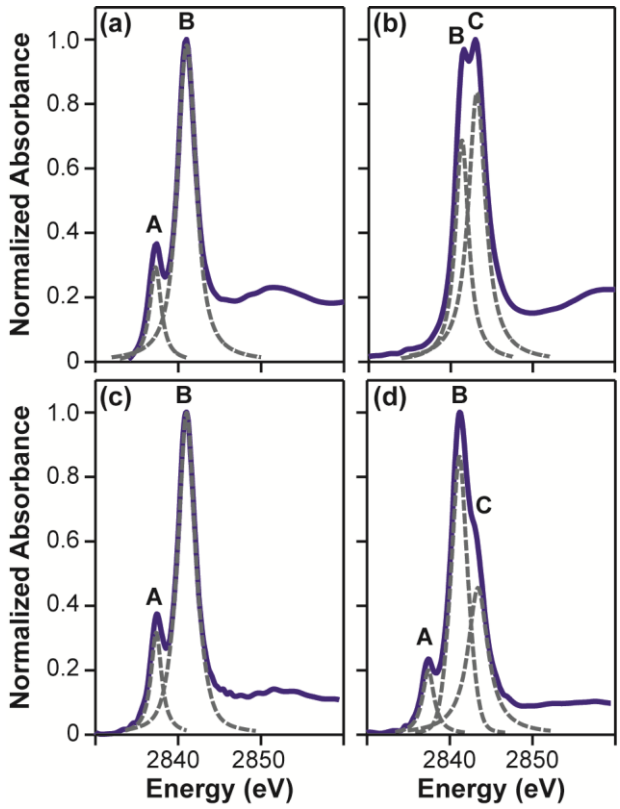

Figure 3.2. The experimental Ru L_3-edge XA spectra of aqueous solutions of (a) $Ru(NH_3)_6Cl_3$, (b) $K_4Ru(CN)_6$, (c) $Fe^{II}Ru^{III}$, and (d) $Ru^{II}Ru^{III}$. The maxima of the spectra have been normalized to unity. Near-edge features in the spectra are labeled A-C, and the positions have been determined by fitting Voigt profiles to the experimental data, which are shown as dashed grey curves. The positions of these features are reported in Tables 3.1 and 3.2.

3.4.2 Experimental spectra of Ru^{II} and Ru^{III} complexes

The aqueous Ru L_3-edge XA spectra of $[Ru(NH_3)_6]^{3+}$, $[Ru(CN)_6]^{4-}$, $Fe^{II}Ru^{III}$, and $Ru^{II}Ru^{III}$ are presented in Figure 3.2a-d. The labeled spectral features have been determined by fitting Voigt profiles to the data, and their positions are listed in Table 3.1 and Table 3.2. For the Ru^{III} complex, $[Ru(NH_3)_6]^{3+}$ shown in Figure 3.2a there are two spectral features labeled A (2837.7 eV) and B (2840.0 eV). With the Ru^{II} complex ($[Ru(CN)_6]^{4-}$) in Figure 3.2b, we identify two features in the pre-edge region of the XA spectrum labeled B (2841.4 eV) and C (2843.2 eV).

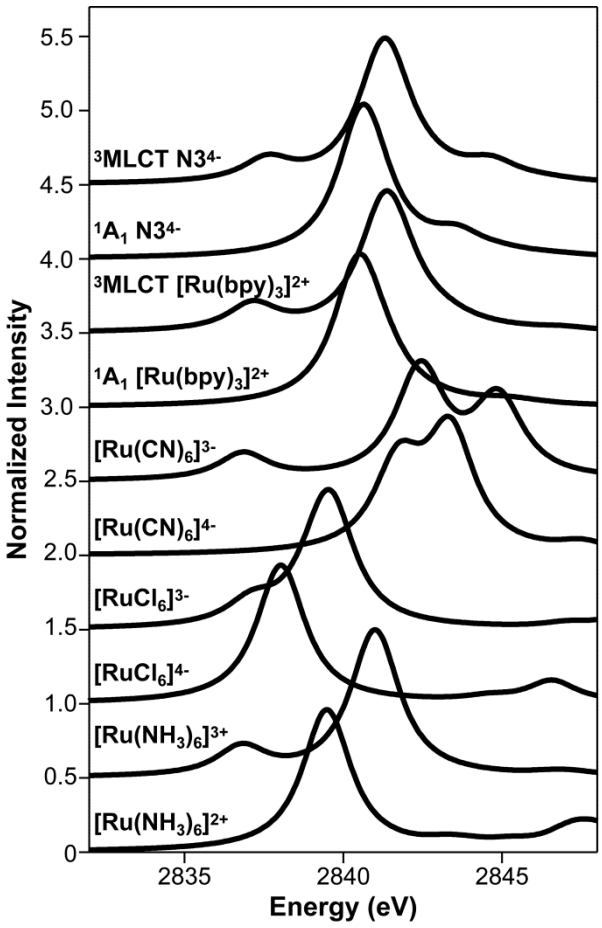

Figure 3.3. TDDFTspectra of the Ru complexes calculated with the B3LYP functional. The spectral profiles are generated by convoluting the discrete transitions with Voigt profiles of 0.4 eV Gaussian and 1.75 eV Lorentzian widths. The intensity of each spectrum is normalized to the most intense feature and it is vertically offset by 0.5 eV from the preceding spectrum. The spectral positions are listed in Table 3.1.

Figure 3.2c shows the spectrum of the $Fe^{II}Ru^{III}$ dimer, which resembles the $[Ru(NH_3)_6]^{3+}$ spectrum with features A and B. The spectrum of $Ru^{II}Ru^{III}$ is shown in Figure 3.2d and contains A, B and C features. Discussion of the XA spectra and chemistry of the mixed-valence complexes will be addressed in section 3.4.5. Here, we focus our attention on the spectra of $[Ru(NH_3)_6]^{3+}$ and $[Ru(CN)_6]^{4-}$, which represent typical Ru^{III} and Ru^{II} compounds. The L_3-edge

Table 3.1. Positions of spectral features A, B and C (in eV) from experimental measurements and B3LYP simulations of the Ru L_3-edge XA spectra shown in Figures 3.2 and 3.3. A -2.49 eV shift is applied to the calculated spectra.[e]

Molecule	**A**		**B**		**C**	
	Calc.	Exp.	Calc.	Exp.	Calc.	Exp.
$[Ru(NH_3)_6]^{2+}$	-	-	2839.5	-	-	-
$[Ru(NH_3)_6]^{3+}$	2836.8	2837.3 [a]	2841.0	2841.0 [a]	-	-
$[RuCl_6]^{4-}$	-	-	2380	-	-	-
$[RuCl_6]^{3-}$	2837.1	2838.2 [b]	2839.5	2840.2 [b]	-	-
$[Ru(CN)_6]^{4-}$	-	-	2841.7	2841.4 [a]	2843.4	2843.2 [a]
$[Ru(CN)_6]^{3-}$	2836.8	-	2842.4	-	2844.9	-
$^1A_1$ $[Ru(bpy)_3]^{2+}$	-	-	2840.6	2840.5 [c]	-	-
^{3}MLCT $[Ru(bpy)_3]^{2+}$	2837.1	2837.6 [c]	2841.4	2841.4 [c]	-	-
$^1A_1$ $N3^{4-}$	-	-	2840.6	2840.3 [d]	2843.6	2843.5 [d]
^{3}MLCT $N3^{4-}$	2837.6	2837.5 [d]	2841.3	2841.3 [d]	2844.7	2844.9 [d]

[a] This work.

[b] Reference 46.

[c] Reference 6.

[d] Reference 7.

[e] The peak positions are determined by fitting Voigt profiles to the XA lineshapes.

spectra of these molecules contain features representative of a broad range of Ru complexes as we discuss below.

As previously discussed, ligand field theory is commonly used to assign features in L-edge X-ray absorption spectroscopy. In O_h symmetry, the Ru 4d orbitals are split by the ligand field into two sets of orbitals where the triply degenerate t_{2g} set is stabilized below the doubly degenerate e_g orbitals by the ligand field splitting energy, Δ_0. For Ru^{II} complexes, there are six 4d electrons

occupying a low-spin configuration, $(t_{2g})^6(e_g)^0$. In contrast, the Ru^{III} oxidation state has a $(t_{2g})^5(e_g)^0$ configuration. With this in mind, feature A in the Ru L_3-edge spectrum of $[Ru(NH_3)_6]^{3+}$ has been assigned to $2p_{3/2} \rightarrow t_{2g}$ transitions, and feature B is assigned to $2p_{3/2} \rightarrow e_g$ transitions. In a static orbital picture, the A-B splitting of 3.3 eV reports directly on the Δ_0 value. In the case of $[Ru(CN)_6]^{4-}$, one might expect transitions to only the vacant e_g orbitals (feature B), but we clearly see another strong spectral feature, labeled C in Figure 3.2b. We attribute the C feature to Ru $2p_{3/2} \rightarrow CN^-$ π^* transitions and will discuss in detail below how TDDFT is instrumental in identifying and assigning these charge-transfer excitations. Solomon and coworkers have assigned higher energy spectral features in the Fe $L_{2,3}$-edge XA spectra of $[Fe^{II/III}(CN)_6]^{4-/3-}$ to charge transfer satellites arising from strong interactions with the CN^- π orbitals using ligand-field theory.[42]

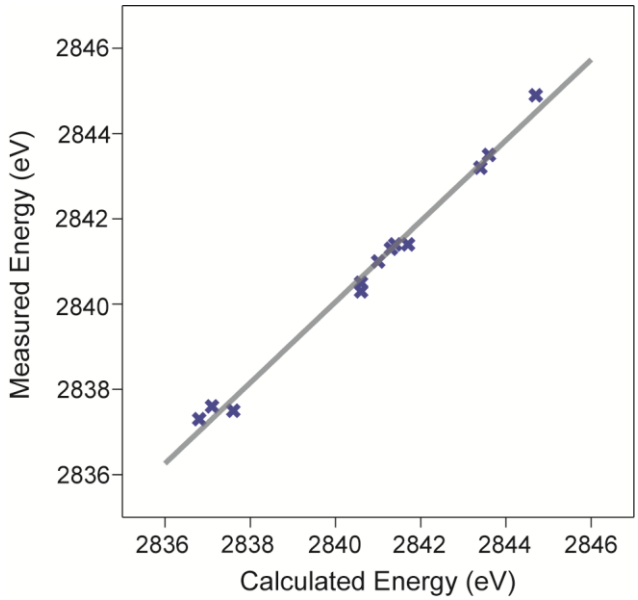

Figure 3.4. Comparison of the energies of fitted spectral features in calculated (after shift is applied) and measured Ru L_3-edge XA spectra for $[Ru(NH_3)_6]^{3+}$, $[Ru(CN)_6]^{4-}$, $[Ru(bpy)_3]^{2+}$, and $[Ru(dcbpy)_2(NCS)_2]^{4-}$($N3^{4-}$). The linear regression is shown as a dark grey line, and the correlation coefficient is 0.991. The RMSD for the data is 0.26 eV.

3.4.3 TDDFT simulations of Ru L_3-edge XA spectra of model complexes: oxidation state and ligand field effects

The Ru L_3-edge X-ray absorption spectra of $[Ru(NH_3)_6]^{2+/3+}$, $[RuCl_6]^{4-/3-}$, $[Ru(CN)]^{4-/3-}$, $^1A_1$ and ^{3}MLCT states of $[Ru(bpy)_3]^{2+}$, and $^1A_1$ and ^{3}MLCT states of $[Ru(dcbpy)_2(NCS)_2]^{4-}$ ($N3^{4-}$) are simulated with the B3LYP functional and shown in Figure 3.3. The positions of spectral features have been determined by fitting the sum of a Gaussian and Lorentzian function to each of the peaks in the spectrum, and their positions are listed in Table 3.1. We have applied a functional specific shift listed in Table 3.3 to each of the calculated spectra. The shift is determined by aligning the B feature in each calculated $[Ru(NH_3)_6]^{3+}$ spectrum to the position of the experimental peak labeled B in Figure 3.2a. The B feature of $[Ru(NH_3)_6]^{3+}$ was chosen for calibration because the simulated spectra do not change qualitatively with the functional choice for $[Ru(NH_3)_6]^{3+}$ (see Figure 3.6). We note that due to deficiencies in the XC functionals and neglect of SOC, un-shifted energies are not expected to agree with experiment, and a constant energy shift is routinely applied in XA simulations.[43-45] The shifts in Table 3.3 provide a calibration energy for each functional. We do not discuss spectral features above the edge jump such as the feature near 2847 eV shown in the simulated $[RuCl_6]^{4-}$ spectrum in Figure 3.3. This is because these features appear at energies that are near or above the absorption edge, and are likely artifacts of the finite basis set employed in our calculations.

For a qualitative interpretation of the spectral features shown in Figure 3.3, we plot the positive part of the difference density for a transition giving rise to a particular spectral feature in the Ru L_3-edge XA spectrum in Figure 3A.1 of the appendix. The difference density is defined as the electron density of the excited state less the ground state density. It is a useful way to visualize

core excitations when no single valence orbital characterizes the final state. The difference densities confirm that the TDDFT interpretations of the spectra agree with the ligand field description discussed in Section 3.4.2, and the labels A, B, and C are used throughout this work to describe transitions of $2p \rightarrow t_{2g}$, $2p \rightarrow e_g$, and $2p \rightarrow$ ligand π^* character, respectively.

The B3LYP functional does an excellent job of reproducing the experimentally observed energy splitting between spectral features and shifts in the spectra (see Table I). Following the -2.49 eV shift, experimental peak positions are plotted against calculated values in Figure 3.4. The linear fit of these data yields a correlation coefficient of 0.991, and the root-mean-square deviation for the data is 0.26 eV, which is significantly less than the lifetime (1.75 eV) and instrument (0.4 eV) widths at the Ru L_3-edge. We note that we have chosen to exclude the $[RuCl_6]^{3-}$ data from Figure3.4.[46] For the case of $[RuCl_6]^{3-}$, the A feature deviates by +1.1 eV

Table 3.2. Positions of experimental and calculated spectral features (in eV) found in Ru L_3-edge XA spectra of the mixed-valence metal dimers, $Fe^{II}Ru^{III}$ and $Ru^{II}Ru^{III}$. [b]

	A	B	C
$Fe^{II}Ru^{III}$			
Experiment	2837.3	2841.0	
Vacuum		2839.7	
COSMO		2840.0	
Shell	2836.8	2841.1	
QM/MM	2836.9	2841.0	
$Ru^{II}Ru^{III}$			
Experiment	2837.4	2841.2	2843.2
Vacuum	2836.8	2839.7	2842.9
COSMO	2837.1	2840.8 (2842.5)[a]	2844.0
Shell	2836.8	2841.3	2843.5
QM/MM	3837.0	2841.2	2843.6

[a] An additional feature was fit to the COSMO spectrum of $Ru^{II}Ru^{III}$ where the spectrum contains four distinguishable features

[b] The peak positions are determined by fitting Voigt profiles to the XA lineshapes.

from the experimental value and the B feature deviates by +0.7 eV, which is significantly greater than the RMSD of 0.26 eV. We consider $[RuCl_6]^{3-}$ to be a clear outlier, and this is likely due to the fact that the experiment used a separate energy calibration from the spectra that we have measured. However, we note that including the $[RuCl_6]^{3-}$ data in the theory—experiment comparison still yields a reasonable correlation coefficient of 0.97. Most importantly, the result in Figure 3.4 clearly shows that TDDFT calculations employing the B3LYP functional are capable of reproducing each of the major features observed in the experimental Ru L_3-edge spectra for all the Ru complexes considered in this study.

Having calibrated our calculations, several clear trends can be observed from the computed spectra in Figure 3.3. As mentioned above, the presence of the A feature in the spectra is a clear indication of an unfilled t_{2g} band and, in the series of complexes studied here, a Ru^{III} oxidation state of the metal. In addition to the appearance of the A feature; there is a shift of the B feature to higher energy for the Ru^{III} complexes. This increase in the transition energy is largely the result of the energetic shifts of the Ru 2p orbitals upon oxidation. The average of the 2p orbital energy shifts by -4.0, -2.5, and -3.2 eV for the ammine, cyanide, and chloride complexes

Table 3.3. Energy shifts for each functional required to align the B feature of calculated spectra with the B peak in the experimental $[Ru(NH_3)_6]^{3+}$ Ru L_3-edge XA spectrum. The functionals are arranged in increasing order of HF content.

Functional	Energy shift (eV)
BP	17.19
O3LYP	3.03
TPSSh	5.93
B3LYP	-2.49
PBE0	-6.27

respectively upon oxidation of the Ru metal. The 2p orbital energies of $[Ru(bpy)_3]$ and $N3^{4-}$ shift by -2.0 and -1.5 eV upon formation of the ^{3}MLCT state. In the case of $[Ru(bpy)_3]$ and $N3^{4-}$ the calculated shifts of the 2p orbital energies agree well with the experimental changes of the ionization potentials of -1.8 and -2.0 eV, respectively.[6,7] Our results emphasize the importance of accounting for shifts in the core orbitals when interpreting changes in Ru L-edge XA spectroscopy. Finally, we note that ligand field strengths are also evident in the spectra shown in Figure 3.3. In the case of the Ru^{III} complexes, the energy difference between the A and B features (E_{BA}), gives the ligand field energy within a single particle approximation. Our B3LYP calculations predict an increasing E_{BA} of 2.3, 3.4 and 5.6 for the Cl^-, NH_3 and CN^- ligands respectively.

3.4.4 Charge Transfer Transitions and Functional Choice in Ru L-edge XA spectroscopy

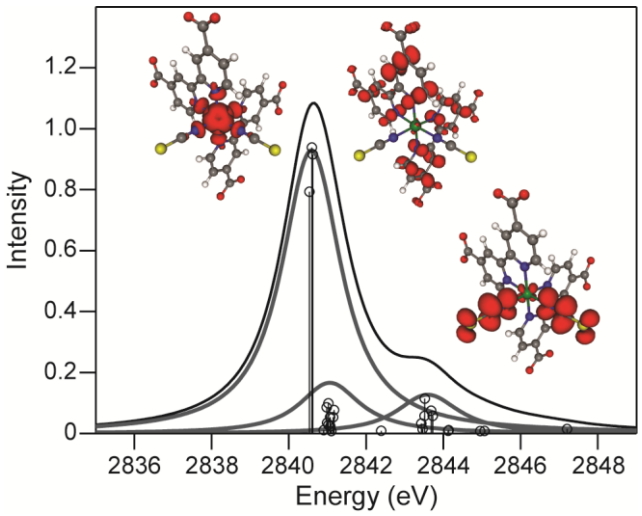

Figure 3.5. TDDFT B3LYP spectrum of the Ru L_3-edge of the $^1A_1$ of $[Ru(dcbpy)_2(NCS)_2]^{4-}$ ($N3^{4-}$). The total spectrum is shown as a black solid line while contributions from transitions of 2p → Ru e_g, 2p → bpy, and 2p → NCS^- π^* character are shown as grey curves. Difference densities representative of the features are shown with an isovalue of 0.002.

One advantage of using quantum chemical methods to simulate XA spectroscopy is that they include all the chemical details of the molecules. While a strong CT feature was easily identified in the spectrum of $[Ru(CN)_6]^{4-}$, weak CT features vary greatly in intensity and may be ligand specific. Figure 3.5 shows the simulated Ru 2p spectrum of the $^1A_1$ state of the $N3^{4-}$ molecule that contains both bpy and NCS^- ligands. In this case, there are spectral features arising from transitions involving the Ru 2p orbitals to valence orbitals of Ru e_g, bpy π^*, and NCS^- π^* character with the two apparent features (B and C) being attributed to the Ru e_g and NCS^- π^* character respectively. Excitations to the Ru e_g, bpy π^*, and NCS^- π^* orbitals represent 75%, 14%, and 11% of the total integrated area of the Ru L_3-edge spectrum. The e_g and NCS^- features are centered at 2840.6 and 2843.6 eV and are shifted less than 0.1 eV from the positions of the B

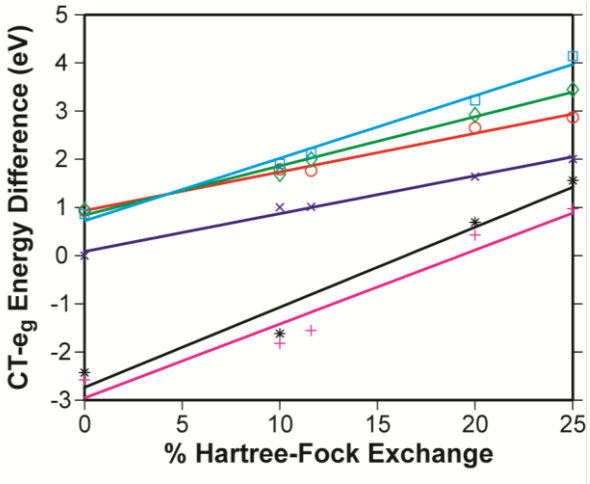

Figure 3.7. The difference between the energy of the most intense CT transition and most intense e_g transition is shown as a function of the HF exchange contribution to the functional. Data is shown for the CN^- peak of $[Ru(CN)_6]^{4-}$ (blue crosses) and $[Ru(CN)_6]^{3-}$ (red circles), the NCS^- peak of $^1A_1$ $N3^{4-}$ (green diamonds) and ^{3}MLCT $N3^{4-}$ (cyan squares), and the bpy peak of $[Ru(bpy)]^{2+}$ (black asterisks) and $^1A_1$ $N3^{4-}$ (magenta plus symbol). Linear fits to the data provide a visual guide.

and C features that were determined by fitting two features to the spectral envelope. Table I lists the positions of the experimental and computed spectral features in the L_3-edge XA spectrum of $N3^{4-}$. The photochemistry and Ru L_3-edge XA spectroscopy of this complex has been discussed in detail in our previous work.[7] We include the $N3^{4-}$ example here to highlight the ability of TDDFT to reproduce spectral features and identify contributions from different ligands in low symmetry complexes. The simulated Ru L_3-edge spectrum of the $^1A_1$ state of $[Ru(bpy)_3]^{2+}$ (plotted in Fig. 3.3) also exhibits a 14% intensity contribution from Ru 2p $\rightarrow$ bpy π^* transitions.

Figure 3.6 shows the Ru L_3-edge spectra of $[Ru(NH_3)_6]^{3+}$ and $[Ru(CN)_6]^{4-}$ calculated with BP, TPSSh, B3LYP, and PBE0 XC functionals. The experimental spectra are shown in the lower panels for comparison. In the case of $[Ru(NH_3)_6]^{3+}$ the spectra show little variation with change of functional. The most significant difference is in the energy splitting between the A and B features (E_{BA}). In particular, the BP functional underestimates the experimental E_{BA} value of 3.7

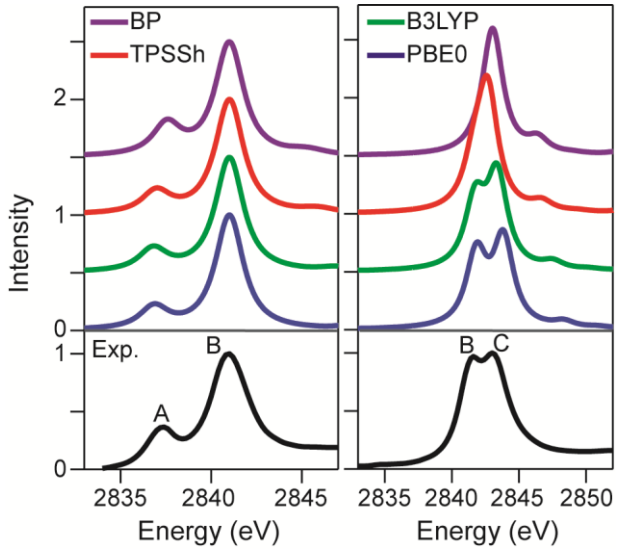

Figure 3.6. TDDFT spectra of the Ru L_3-edge of $[Ru^{III}(NH_3)_6]^{3+}$ (left) and $[Ru^{II}(CN)_6]^{4-}$ (right) calculated with BP, TPSSh, B3LYP, and PBE0 functionals. The bottom panel shows the experimental spectra for comparison.

eV by 0.3 eV. All global hybrid functionals overestimate the E_{BA} experimental value resulting in calculated E_{BA} values of 4.0, 4.2, and 4.1 eV for TPSSh, B3LYP, and PBE0, respectively. In the case of $[RuCl_6]^{3-}$ the calculated E_{BA} is 1.5 and 2.3 eV for the BP and B3LYP functionals, respectively. The experimental E_{BA} value of $[RuCl_6]^{3-}$ is measured to be 2.0 eV which suggests that the global hybrid functionals are better at predicting the spin-free properties of these simple octahedral complexes, since an overestimation of E_{BA} is expected when SOC is not included.

In the case of $[Ru(CN)_6]^{4-}$ shown in Figure 3.6 (right column), the effect of HF exchange present in global hybrid functionals is much more apparent due to the presence of the CT feature, C. With no HF exchange contribution (the BP case) the B and C features have coalesced into a single peak and no charge transfer feature is visible. With 10% HF exchange, the spectrum begins to show two features and fitting the spectrum yields an energy difference between the B and C features of 1.0 eV. B3LYP and PBE0 give an energy difference between the B and C features of 1.7 eV and 2.0 eV, respectively and are in good agreement with the experimental value of 1.8 eV.

To further assess the effect of HF exchange across a range of transitions, we consider the CT features present due to π^* orbitals of CN^- in $[Ru(CN)_6]^{3-/4-}$, NCS^- in $N3^{4-}$, and bpy in $[Ru(bpy)_3]^{2+}$ and $N3^{4-}$. We focus on the relative CT energy defined as the energy difference between the most intense CT transition and the most intense e_g transition and plot it against the percent of HF exchange in Figure 3.7. In all cases the relative CT energy increases with the HF exchange content. Transitions arising from CN^- π^* orbitals (blue crosses and red circles) have the weakest dependence on HF exchange while the features arising from bpy ligands (black asterisks and magenta plus signs) have the strongest dependence. The strong dependence of the bpy CT states on the HF exchange content is expected due to the diffuse nature of bpy π^* orbitals

involved in these excitations as shown in the difference densities plotted in Figure 3.5. Use of a pure DFT functional like BP produces a feature that is > 2.0 eV below the e_g feature yielding a low energy peak in the XA spectrum that is not observed experimentally. The weak dependence of the CN^- π^* transitions on the functional choice results from the larger metal character in the CT state due to strong metal–ligand interactions.

Based on the above observations, it appears that the B3LYP and PBE0 functionals are able to predict the energies of CT features in Ru L-edge spectroscopy. However, PBE0 consistently overestimates the energy of CT features, and the RMSD for the difference between experiment and theory is 0.44 eV, which is significantly greater than the RMSD of 0.26 eV for B3LYP. If the linear regressions in Figure 3.7 are used to determine the optimal values of HF exchange, it is predicted that 22%, 21%, and 22% would produce the experimentally observed CT energies for $[Ru(CN)_6]^{4-}$, $^1A_1$ $N3^{4-}$, and ^{3}MLCT $N3^{4-}$, respectively. Thus, we conclude that B3LYP with 20% HF exchange provides the best choice for XC functional among the set of commonly used functionals that we have investigated. The importance of using global hybrid functionals for TDDFT simulations of XA spectra has been previously discussed for the pre-edge region of transition metal K-edge spectroscopy. We observed that use of the BP functional leads to underestimation of Fe 1s $\rightarrow$ ligand π^* transition energies in an Fe^{II} spin crossover complex.[47] In the recent work of Roemelt *et al.* a functional with 22% HF exchange was recommended for reproducing the pre-edge spectra of Mn complexes where Mn 1s $\rightarrow$ 3d transitions and Mn 1s $\rightarrow$ π^* CT transitions are important.[48] These studies are in agreement with our present results and provide additional evidence that B3LYP is a reliable functional for TDDFT simulations of core-level spectroscopies in these systems. The above discussion suggests that the observed CT features are not long range excitations. Consequently, sophisticated range-separated hybrid

functionals are not required to reproduce energies of the CT features in Ru L-edge XA spectroscopy.

3.4.5 Ru L-edge XA spectroscopy of cyanide bridged mixed-valence metal dimers

The spectroscopy of transition metal mixed-valence complexes has garnered much interest because they provide ideal systems for understanding coupled electronic and nuclear motions during ultrafast photoinduced metal-to-metal charge transfer (MMCT).[49-54] We study cyanide-bridged dimer systems of the form, $\left[(NC)_5M^{II}-CN-Ru^{III}(NH_3)_5\right]^-$, where M= Fe or Ru. One

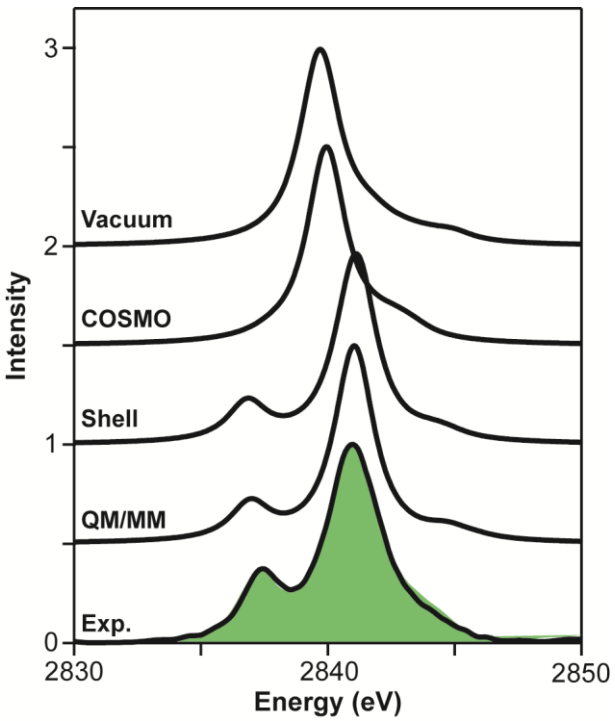

Figure 3.8. Experimental and simulated Ru L_3-edge spectra of $Fe^{II}Ru^{III}$. The experimental spectrum is shown following subtraction of the edge jump. The green shaded region represents the $[Ru(NH_3)_6]^{3+}$ spectrum. Simulated spectra are shown for vacuum (gas phase), COSMO, shell, and QM/MM treatments of the solvent environment as described in the main text. The maximum of each spectrum has been normalized to 1.0.

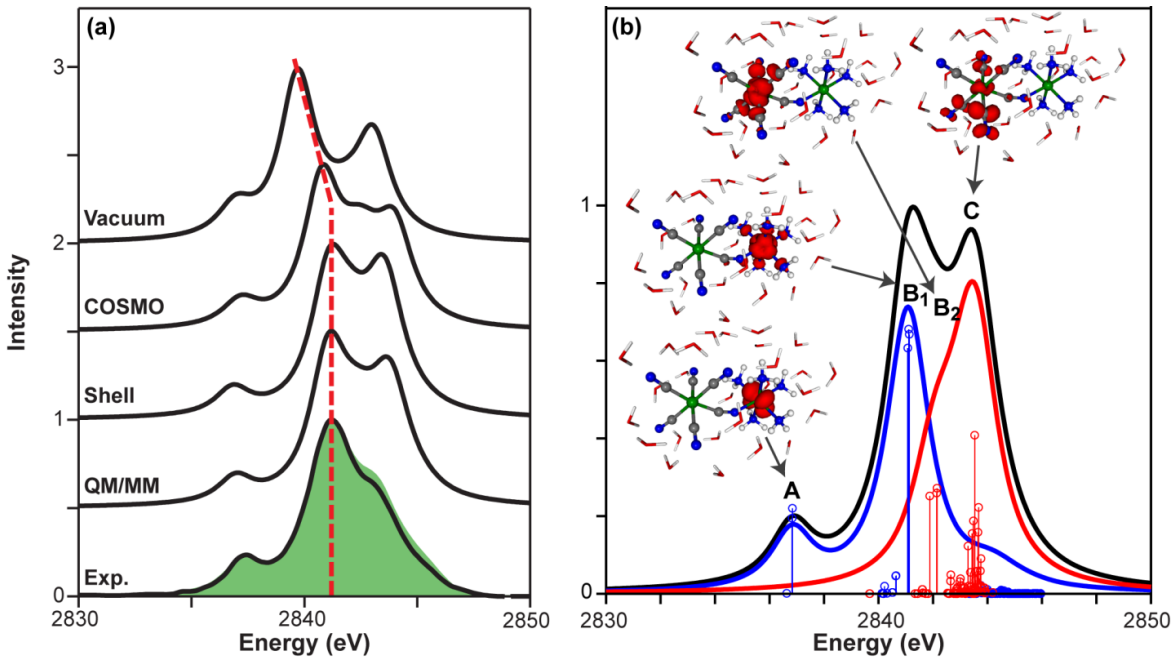

Figure 3.9. (a) Experimental and B3LYP TDDFT Ru L_3-edge XA spectra of $Ru^{II}Ru^{III}$. The experimental spectrum is shown following subtraction of the edge jump. The green shaded region represents the normalized summation of experimental $[Ru(NH_3)_6]^{3+}$ and $[Ru(CN)_6]^{4-}$ spectra. Simulated spectra are shown for vacuum, COSMO, shell, and QM/MM treatments of the solvent environment as described in the main text. The maximum of each spectrum has been normalized to 1.0. Red dotted line is to guide the eye on the position of the most intense feature identified as the $Ru[NH_3]$ 2p $\rightarrow e_g$ transition. (b) B3LYP spectrum of $Ru^{II}Ru^{III}$ using the shell model for the solvent. Individual contributions from the $Ru[NH_3]$ and Ru[CN] fragments are shown as blue and red data, respectively. Difference densities (isovalues of 0.005) identify the contributions to the spectra.

of the important questions in the chemistry of mixed-valence molecules is of electron delocalization.[55] While the formal charges of metals in $Fe^{II}Ru^{III}$ complex suggest d^6 and d^5 ground state electron configurations, electronic coupling between the metal centers can lead to electron delocalization across the cyanide bridge and result in deviations to the formal charges.[55] This has important implications for understanding the MMCT process, since electron

delocalization modifies the charge transfer distance and solvent dipole orientation. The solvent itself has a strong impact on the degree of localization, which is evidenced by the solvatochromism of the MMCT energy in the visible and NIR.[56] Given that Ru L-edge XA spectroscopy is sensitive to the oxidation state of Ru complexes, we use it to measure the degree to which the charges are delocalized in $Fe^{II}Ru^{III}$ and $Ru^{II}Ru^{III}$. Moreover, these complexes provide a useful test case for assessing the level of detail that must be employed to treat solvent effects in computational models for effectively simulating core-level XA spectra.

For modeling the solvent, we have employed both implicit and explicit solvent models and compared these to the gas phase results. For the implicit solvent the COSMO model has been used. For explicit modeling of the solvent, the QM/MM protocol described in Section 3.2 was used. An additional solvent model, which we call the "shell" model, was constructed by extracting the solute and the first solvation shell from the QM/MM simulation box. In this study it includes the twenty-six water molecules nearest to the solute (within ~2.3 Å of the solute). For the shell model, the entire system is treated quantum mechanically, and the rest of the solvent is treated with COSMO. The shell model allows us to calculate the X-ray spectrum with ORCA providing an implementation independent comparison with other results. Regardless of solvent treatment the same geometry from the QM/MM optimization is employed for all X-ray simulations. The octahedra of the two metals are aligned and the molecule is bent so hydrogen bonds form between the cyanide and ammine groups (see Figure 3A.2). These bent structures are qualitatively similar to the crystal structure of a related iron-ruthenium dimer.[57] This geometry is also similar to the bent COSMO optimized geometry reported by Kondov *et al.*[58] Linear geometries that likely exist in solution were also investigated, but little difference was observed between the X-ray spectra of linear and bent species. A future study will investigate

the role of structural heterogeneity on the spectroscopic properties of these molecules. Inspection of the QM/MM geometries show that there are many hydrogen bonds to the cyanide ligands while the NH_3 ligands are not as strongly coordinated by the surrounding solvent.

Figure 3.8 shows the experimental and simulated (using B3LYP) XA spectra of the Ru L_3-edge of $Fe^{II}Ru^{III}$. The spectral positions for the peaks in the experimental and computed XA spectra are listed in Table II. The green shaded area represents the spectrum of $[Ru(NH_3)_6]^{3+}$. The similarity between the $Fe^{II}Ru^{III}$ spectrum and the green shaded area suggests that the Ru atom in $Fe^{II}Ru^{III}$ is in the +3 oxidation with similar character to Ru in $[Ru(NH_3)_6]^{3+}$. The simulated spectra for the gas phase and COSMO models contain only a single feature centered at 2839.7 and 28340.0 eV. The B feature in the simulated $[Ru(NH_3)_6]^{2+}$ spectrum lies at 2839.5 eV suggesting that the gas phase and COSMO results predict that the Ru atom in $Fe^{II}Ru^{III}$ is in the +2 oxidation state. This conclusion is supported by the Mulliken spin populations reported in Table 3.4 confirming presence of the unpaired electron on the Fe atom. Conversely, use of either of the explicit solvent models reproduces the double peaked spectrum observed experimentally, and the spin populations of 0.0 on Fe and 1.0 on Ru confirm the presence a localized unpaired electron on the Ru center. This strongly supports the interpretation of $Fe^{II}Ru^{III}$ valencies with localized d electrons.

As shown previously in Figure 3.2d, the experimental Ru L_3-edge XA spectrum for the $Ru^{II}Ru^{III}$ complex contains three features labeled A, B, and C. The summation of the experimental $[Ru(NH_3)_6]^{3+}$ and $[Ru(CN)_6]^{4-}$ XA spectra is shown as the green shaded area in Figure 3.9a and it does an excellent job of reproducing the experimentally measured $Ru^{II}Ru^{III}$ spectrum (bottom curve). While there are slight differences in intensities of the spectral features between the summed and $Ru^{II}Ru^{III}$ spectra, their positions are not shifted significantly. The

simulated $Ru^{II}Ru^{III}$ spectra shown in Figure 3.9a are broader than the experimental spectra, but show three features in the case of the shell and QM/MM models.

To identify the individual contributions to the spectra, the B3LYP spectrum of $Ru^{II}Ru^{III}$ simulated with the shell model is plotted in Figure 3.9b. The blue and red data show the contributions from the individual fragments, and four contributions to the spectrum are identified. The total spectrum contains excitations from the $Ru[NH_3]$ fragment where core-excited states are characterized by excitation into t_{2g} (A) and e_g (B_1) orbitals and the Ru[CN] fragment with core excitations to e_g (B_2) and CN^- π^* (C) orbitals. Despite containing each contribution observed in the spectra of the model complexes, the spectrum of Ru[CN] shown in red has a different intensity pattern than the spectrum of the model complex where each feature (B and C in Figure 3.2b) has nearly equal intensity. The low intensity of the B_2 feature relative to the C feature could account for the discrepancy between the measured and calculated spectra. It is possible that agreement between experimental and calculated spectra may be improved by sampling more molecular configurations. Future studies will take snapshots from *ab initio*

Table 3.4. Mulliken spin population on each of the metal centers for each solvent treatment used to calculate Ru L_3-edge XA spectra of the mixed valence complexes, $Fe^{II}Ru^{III}$ and $Ru^{II}Ru^{III}$. Ru[CN] and $Ru[NH_3]$ refer to the Ru atom in the $Ru(CN)_6$ and $Ru(NH_3)_5$ moieties, respectively.

	$Fe^{II}Ru^{III}$		$Ru^{II}Ru^{III}$	
	Fe	Ru	Ru[CN]	$Ru[NH_3]$
Vacuum	1.11	-0.01	0.87	0.00
COSMO	1.00	0.11	0.24	0.75
Shell	0.00	1.04	0.00	1.04
QM/MM	0.04	0.97	0.03	0.98

molecular dynamics simulations to determine the degree to which fluctuations in atomic configurations affect the X-ray spectra.

The spectral signature of valence delocalization in the $Ru^{II}Ru^{III}$ complex remains clear following the identification of the low energy edge of the B feature in Figure 3.1d with the e_g feature of $Ru[NH_3]$ fragment (B_1 in Figure 3.9b). With the explicit solvent models the leading edge of the simulated spectrum is well aligned with the experimental data, and the spin populations in Table IV for these models show that the unpaired electron is well localized on the $Ru[NH_3]$ fragment. Use of the implicit solvent model leads to a -0.5 eV shift in B relative to the shell model, which is correlated with spin populations of 0.75 and 0.25 for $Ru[NH_3]$ and Ru[CN], respectively. The spectral shift is attributed to a delocalization of the valence electrons that increases the charge density at the $Ru[NH_3]$ atom. The spectrum also broadens further since the Ru[CN] contribution shifts to higher energy as it oxidizes. In the case of the vacuum simulation, the B feature is further shifted to 2839.7 eV similar to the B feature in $[Ru(NH_3)_6]^{2+}$ at 2839.5 eV. The Mulliken population on the $Ru[NH_3]$ fragment is 0.0 with the majority of the spin population residing on the Ru[CN] atom and CN^- bridging ligand. Consequently, the shift of the leading edge tracked by the red dashed curve in Figure 3.9a monitors the redistribution of electrons between the Ru atoms and over the bridging ligand. The experiments and simulations imply that $Ru^{II}Ru^{III}$ should be viewed as having localized valence electrons, and highlight the role of specific solvent–solute interactions in governing the electronic properties of this complex.

The degree of delocalization in these mixed valence complexes has been previously estimated using parameters derived from electrochemical, UV/Vis, and Stark spectroscopy,[57,59] The electronic spectroscopies are only indirectly sensitive to the delocalization of the valence electrons, and rely on mapping experimental results to a two state model.[57,60] Transition metal

L-edge measurements are directly sensitive to the valence of the metal because the energies of 2p orbitals respond to changes in the electron density at the metal center. The X-ray measurements employed here suggest that the electronic coupling between metal centers is quite weak due to the fact that the mixed-valence spectra are indistinguishable from the monomer spectra. For $Fe^{II}Ru^{III}$, TDDFT predicts that the B feature in the Ru L_3-edge shifts by -1.3 eV as when the electron localizes on the Ru center instead of the Fe center. We expect that a delocalization of 10% indicated by a decrease in the spin population at the Ru center would result in a spectral shift of ~0.1 eV. Given that dimer and monomer spectra are nearly indistinguishable, we conclude that our experimental and explicit solvent results are in good agreement with previous electro-absorption measurements.

3.5. Summary

In this article, we have shown that TDDFT provides a predictive tool for Ru L_3-edge XA spectroscopy. The simulations reproduce each of the features present in experimental spectra and a difference density analysis of the transitions identifies the molecular origin of each of the spectral features. We have concluded that B3LYP is an ideal functional for simulating Ru L_3-edge spectra. After calibration of the energy axis, B3LYP predicts the energy positions of the experimental spectra with a RMSD of 0.26 eV. The B3LYP functional emerges as the best functional for simulating the CT features that arise from the mixing of Ru 4d and ligand orbitals. Our results show that TDDFT has the distinct advantage of being able to treat systems of low-symmetry and we identify ligand-specific CT features in the Ru L_3-edge spectra of $N3^{4-}$. We also demonstrate that TDDFT can successfully simulate Ru L_3-edge XA spectra of systems containing multiple metal centers when explicit solute-solvent interactions are taken into

account. In the case of $Fe^{II}Ru^{III}$ and $Ru^{II}Ru^{III}$ complexes strong hydrogen bonding interactions with the CN ligands stabilize and localize the +2 oxidation state on the metal cyanide moiety, and the +3 oxidation state is observed on the ammine fragment. This study describes in detail how core-level excitations within TDDFT can be computed using many of the most widely used quantum chemistry codes providing a useful and powerful interpretive tool for equilibrium and ultrafast Ru L_3-edge spectroscopy.

REFERENCES

(1) Campagna, S.; Puntoriero, F.; Nastasi, F.; Bergamini, G.; Balzani, V. Photochemistry and Photophysics of Coordination Compounds: Ruthenium. *Top. Curr. Chem.* **2007**, *280*, 117-214.

(2) Grätzel, M. Recent Advances in Sensitized Mesoscopic Solar Cells. *Acc. Chem. Res.* **2009**, *42*, 1788-1798.

(3) Concepcion, J. J.; Jurss, J. W.; Brennaman, M. K.; Hoertz, P. G.; Patrocinio, A. O. T.; Murakami Iha, N. Y.; Templeton, J. L.; Meyer, T. J. Making Oxygen with Ruthenium Complexes. *Acc. Chem. Res.* **2009**, *42*, 1954-1965.

(4) Alperovich, I.; Smolentsev, G.; Moonshiram, D.; Jurss, J. W.; Concepcion, J. J.; Meyer, T. J.; Soldatov, A.; Pushkar, Y. Understanding the Electronic Structure of 4d Metal Complexes: From Molecular Spinors to L-Edge Spectra of a di-Ru Catalyst. *J. Am. Chem. Soc.* **2011**, *133*, 15786-15794.

(5) Shearer, J.; Callan, P. E.; Masitas, C. A.; Grapperhaus, C. A. Influence of Sequential Thiolate Oxidation on a Nitrile Hydratase Mimic Probed by Multiedge X-Ray Absorption Spectroscopy. *Inorg. Chem.* **2012**, *51*, 6032-6045.

(6) Gawelda, W.; Johnson, M.; de Groot, F. M. F.; Abela, R.; Bressler, C.; Chergui, M. Electronic and Molecular Structure of Photoexcited $[Ru^{II}(bpy)_3]^{2+}$ Probed by Picosecond X-Ray Absorption Spectroscopy. *J. Am. Chem. Soc.* **2006**, *128*, 5001-5009.

(7) Van Kuiken, B. E.; Huse, N.; Cho, H.; Strader, M. L.; Lynch, M. S.; Schoenlein, R. W.; Khalil, M. Probing the Electronic Structure of a Photoexcited Solar Cell Dye with Transient X-Ray Absorption Spectroscopy. *J. Phys. Chem. Lett.* **2012**, *3*, 1695-1700.

(8) Saes, M.; Bressler, C.; Abela, R.; Grolimund, D.; Johnson, S. L.; Heimann, P. A.; Chergui, M. Observing Photochemical Transients by Ultrafast X-Ray Absorption Spectroscopy. *Phys. Rev. Lett.* **2003**, *90,* 047403/1-047403/4.

(9) Stavitski, E.; de Groot, F. M. F. The CTM4XAS Program for EELS and XAS Spectral Shape Analysis of Transition Metal L Edges. *Micron* **2010**, *41*, 687-694.

(10) Alperovich, I.; Moonshiram, D.; Soldatov, A.; Pushkar, Y. Ru $L_{2,3}$ Xanes Theoretical Simulation with DFT: A Test of the Core-Hole Treatment. *Solid State Commun.* **2012**, *152*, 1880-1884.

(11) Campbell, L.; Mukamel, S. Simulation of X-Ray Absorption near Edge Spectra of Electronically Excited Ruthenium Tris-2,2'-Bipyridine. *J. Chem. Phys.* **2004**, *121*, 12323-12333.

(12) Ekström, U.; Norman, P.; Carravetta, V. Relativistic Four-Component Static-Exchange Approximation for Core-Excitation Processes in Molecules. *Phys. Rev. A* **2006**, *73*, 022501.

(13) Ikeno, H.; Tanaka, I.; Koyama, Y.; Mizoguchi, T.; Ogasawara, K. First-Principles Multielectron Calculations of Ni $L_{2,3}$ NEXAFS and ELNES for $LiNiO_2$ and Related Compounds. *Phys. Rev. B* **2005**, *72*, 075123/075121-075123/075128.

(14) Wang, F.; Ziegler, T.; van Lenthe, E.; van Gisbergen, S.; Baerends, E. J. The Calculation of Excitation Energies Based on the Relativistic Two-Component Zeroth-Order Regular Approximation and Time-Dependent Density-Functional with Full Use of Symmetry. *J. Chem. Phys.* **2005**, *122*, 204103.

(15) Casarin, M.; Finetti, P.; Vittadini, A.; Wang, F.; Ziegler, T. Spin-Orbit Relativistic Time-Dependent Density Functional Calculations of the Metal and Ligand Pre-Edge XAS Intensities

of Organotitanium Complexes: $TiCl_4$, $Ti(h^5\text{-}C_5H_5)Cl_3$, and $Ti(h^5\text{-}C_5H_5)_2Cl_2$. *J. Phys. Chem. A* **2007**, *111*, 5270-5279.

(16) Bast, R.; Jensen, H. J. A.; Saue, T. Relativistic Adiabatic Time-Dependent Density Functional Theory Using Hybrid Functionals and Noncollinear Spin Magnetization. *Int. J. Quantum Chem.* **2009**, *109*, 2091-2112.

(17) Lopata, K.; Van Kuiken, B. E.; Khalil, M.; Govind, N. Linear-Response and Real-Time Time-Dependent Density Functional Theory Studies of Core-Level Near-Edge X-Ray Absorption. *J. Chem. Theory Comput.* **2012**, *8*, 3284-3292.

(18) Vogler, A.; Kisslinger, J. Photosubstitution of Pentaamminechlororuthenium(III) Hexacyanoruthenate(II) Following Outer-Sphere Intervalence Excitation. *J. Am. Chem. Soc.* **1982**, *104*, 2311-2312.

(19) Neese, F. The Orca Program System. *WIREs: Comput. Mol. Sci.* **2012**, *2*, 73-78.

(20) Becke, A. A New Mixing of Hartree-Fock and Local Density-Functional Theories. *J. Chem. Phys.* **1993**, *98*, 1372.

(21) Stephens, P. J.; Devlin, F. J.; Chabalowski, C. F.; Frisch, M. J. Ab Initio Calculation of Vibrational Absorption and Circular Dichroism Spectra Using Density Functional Force Fields. *J. Phys. Chem.* **1994**, *98*, 11623-11627.

(22) Weigend, F.; Ahlrichs, R. Balanced Basis Sets of Split Valence, Triple Zeta Valence and Quadruple Zeta Valence Quality for H to Rn: Design and Assessment of Accuracy. *Phys. Chem. Chem. Phys.* **2005**, *7*, 3297-3305.

(23) Klamt, A.; Schuurmann, G. Cosmo: A New Approach to Dielectric Screening in Solvents with Explicit Expressions for the Screening Energy and Its Gradient. *J. Chem. Soc.-Perkin Trans. 2* **1993**, 799-805.

(24) Adamo, C.; Barone, V. Toward Reliable Density Functional Methods without Adjustable Parameters: The PBE0 Model. *J. Chem. Phys.* **1999**, *110*, 6158-6170.

(25) Dolg, M.; Wedig, U.; Stoll, H.; Preuss, H. Energy-Adjusted Ab Initio Pseudopotentials for the First Row Transition Elements. *J. Chem. Phys.* **1987**, *86*, 866-872.

(26) Berendsen, H. J. C.; Grigera, J. R.; Straatsma, T. P. The Missing Term in Effective Pair Potentials. *J. Phys. Chem.* **1987**, *91*, 6269-6271.

(27) Berendsen, H. J. C.; Postma, J. P. M.; van Gunsteren, W. F.; DiNola, A.; Haak, J. R. Molecular Dynamics with Coupling to an External Bath. *J. Chem. Phys.* **1984**, *81*, 3684-3690.

(28) Valiev, M.; Bylaska, E. J.; Govind, N.; Kowalski, K.; Straatsma, T. P.; Van Dam, H. J. J.; Wang, D.; Nieplocha, J.; Apra, E.; Windus, T. L.et al. Nwchem: A Comprehensive and Scalable Open-Source Solution for Large Scale Molecular Simulations. *Comput. Phys. Comm.* **2010**, *181*, 1477-1489.

(29) Neese, F. Calculation of Electric-Field Gradients Based on Higher-Order Generalized Douglas-Kroll Transformations. *J. Chem. Phys.* **2005**, *122*, 204107.

(30) Pantazis, D. A.; Chen, X.-Y.; Landis, C. R.; Neese, F. All-Electron Scalar Relativistic Basis Sets for Third-Row Transition Metal Atoms. *J. Chem. Theory Comput.* **2008**, *4*, 908-919.

(31) Noro, T.; Sekiya, M.; Koga, T.; Saito, S. L. Relativistic Contracted Gaussian-Type Basis Functions for Atoms K through Xe. *Chem. Phys. Lett.* **2009**, *481*, 229-233.

(32) Becke, A. D. Density-Functional Exchange-Energy Approximation with Correct Asymptotic Behavior. *Phys. Rev. A* **1988**, *38*, 3098-3100.

(33) Perdew, J. P. Density-Functional Approximation for the Correlation Energy of the Inhomogeneous Electron Gas. *Phys. Rev. B* **1986**, *33*, 8822-8824.

(34) Tao, J.; Perdew, J. P.; Staroverov, V. N.; Scuseria, G. E. Climbing the Density Functional Ladder: Nonempirical Meta–Generalized Gradient Approximation Designed for Molecules and Solids. *Phys. Rev. Lett.* **2003**, *91*, 146401.

(35) Cohen, A. J.; Handy, N. C. Dynamic Correlation. *Mol. Phys.* **2001**, *99*, 607-615.

(36) van Lenthe, E.; Baerends, E. J.; Snijders, J. G. Relativistic Regular Two-Component Hamiltonians. *J. Chem. Phys.* **1993**, *99*, 4597-4610.

(37) Nichols, P.; Govind, N.; Bylaska, E. J.; de Jong, W. A. Gaussian Basis Set and Planewave Relativistic Spin−Orbit Methods in NWChem. *J. Chem. Theory Comput.* **2009**, *5*, 491-499.

(38) de Groot, F. M. F.; Hu, Z. W.; Lopez, M. F.; Kaindl, G.; Guillot, F.; Tronc, M. Differences between L_3 and L_2 X-Ray Absorption Spectra of Transition Metal Compounds. *J. Chem. Phys.* **1994**, *101*, 6570-6576.

(39) Sham, T. K. X-Ray Absorption Spectra of Ruthenium L Edges in $Ru(NH_3)_6Cl_3$. *J. Am. Chem. Soc.* **1983**, *105*, 2269-2273.

(40) Hu, Z.; von Lips, H.; Golden, M. S.; Fink, J.; Kaindl, G.; de Groot, F. M. F.; Ebbinghaus, S.; Reller, A. Multiplet Effects in the Ru L_{23} X-Ray-Absorption Spectra of Ru(IV) and Ru(V) Compounds. *Phys. Rev. B* **2000**, *61*, 5262-5266.

(41) de Groot, F. M. F. Multiplet Effects in X-Ray Spectroscopy. *Coord. Chem. Rev.* **2005**, *249*, 31-63.

(42) Hocking, R. K.; Wasinger, E. C.; de Groot, F. M. F.; Hodgson, K. O.; Hedman, B.; Solomon, E. I. Fe L-Edge XAS Studies of $K_4[Fe(CN)_6]$ and $K_3[Fe(CN)_6]$: A Direct Probe of Back-Bonding. *J. Am. Chem. Soc.* **2006**, *128*, 10442-10451.

(43) DeBeer George, S.; Petrenko, T.; Neese, F. Prediction of Iron K-Edge Absorption Spectra Using Time-Dependent Density Functional Theory. *J. Phys. Chem. A* **2008**, *112*, 12936-12943.

(44) Prendergast, D.; Galli, G. X-Ray Absorption Spectra of Water from First Principles Calculations. *Phys. Rev. Lett.* **2006**, *96*, 215502.

(45) Leetmaa, M.; Ljungberg, M. P.; Lyubartsev, A.; Nilsson, A.; Pettersson, L. G. M. Theoretical Approximations to X-Ray Absorption Spectroscopy of Liquid Water and Ice. *J. Electron Spectrosc. Rel. Phenom.* **2010**, *177*, 135-157.

(46) Sugiura, C.; Kitamura, M.; Muramatsu, S. X-Ray Absorption near-Edge Structure of Complex Compounds $(NH_4)_3RhCl_6$, K_3RuCl_6, and $Ru(NH_3)_6Cl_3$. *J. Chem. Phys.* **1986**, *84*, 4824-4827.

(47) Van Kuiken, B. E.; Khalil, M. Simulating Picosecond Iron K-Edge X-Ray Absorption Spectra by Ab Initio Methods to Study Photoinduced Changes in the Electronic Structure of Fe(II) Spin Crossover Complexes. *J. Phys. Chem. A* **2011**, *115*, 10749-10761.

(48) Roemelt, M.; Beckwith, M. A.; Duboc, C.; Collomb, M.-N.; Neese, F.; DeBeer, S. Manganese K-Edge X-Ray Absorption Spectroscopy as a Probe of the Metal–Ligand Interactions in Coordination Compounds. *Inorg. Chem.* **2011**, *51*, 680-687.

(49) Reid, P. J.; Silva, C.; Barbara, P. F.; Karki, L.; Hupp, J. T. Electronic Coherence, Vibrational Coherence, and Solvent Degrees of Freedom in the Femtosecond Spectroscopy of Mixed-Valence Metal Dimers in H_2O and D_2O. *J. Phys. Chem.* **1995**, *99*, 2609-2616.

(50) Arnett, D. C.; Voehringer, P.; Scherer, N. F. Excitation Dephasing, Product Formation, and Vibrational Coherence in an Intervalence Charge-Transfer Reaction. *J. Am. Chem. Soc.* **1995**, *117*, 12262-12272.

(51) Doorn, S. K.; Dyer, R. B.; Stoutland, P. O.; Woodruff, W. H. Ultrafast Electron Transfer and Coupled Vibrational Dynamics in Cyanide Bridged Mixed-Valence Transition-Metal Dimers. *J. Am. Chem. Soc.* **1993**, *115*, 6398-6405.

(52) Lynch, M. S.; Van Kuiken, B. E.; Daifuku, S. L.; Khalil, M. On the Role of High-Frequency Intramolecular Vibrations in Ultrafast Back-Electron Transfer Reactions. *J. Phys. Chem. Lett.* **2011**, *2*, 2252-2257.

(53) Lynch, M. S.; Slenkamp, K. M.; Khalil, M. Communication: Probing Non-Equilibrium Vibrational Relaxation Pathways of Highly Excited C ≡ N Stretching Modes Following Ultrafast Back-Electron Transfer. *J. Chem. Phys.* **2012**, *136*, 241101-241104.

(54) Wang, C. F.; Mohney, B. K.; Akhremitchev, B. B.; Walker, G. C. Ultrafast Infrared Spectroscopy of Vibrational States Prepared by Photoinduced Electron Transfer in $(CN)_5FeCNRu(NH_3)_5^-$. *J. Phys. Chem. A* **2000**, *104*, 4314-4320.

(55) Demadis, K. D.; Hartshorn, C. M.; Meyer, T. J. The Localized-to-Delocalized Transition in Mixed-Valence Chemistry. *Chem. Rev.* **2001**, *101*, 2655-2686.

(56) Blackbourn, R. L.; Hupp, J. T. Probing the Molecular Basis of Solvent Reorganization in Electron-Transfer Reactions. *J. Phys. Chem.* **1988**, *92*, 2817-2820.

(57) Vance, F. W.; Slone, R. V.; Stern, C. L.; Hupp, J. T. Comparative Absorption, Electroabsorption and Electrochemical Studies of Intervalence Electron Transfer and Electronic Coupling in Cyanide-Bridged Bimetallic Systems: Ancillary Ligand Effects. *Chem. Phys.* **2000**, *253*, 313-322.

(58) Kondov, I.; Vallet, V. r.; Wang, H.; Thoss, M. Ground- and Excited-State Properties of the Mixed-Valence Complex $[(NH_3)_5Ru^{III}NCRu^{II}(CN)_5]^-$ *J. Phys. Chem. A* **2008**, *112*, 5467-5477.

(59) Burewicz, A.; Haim, A. Formation and Properties of the Binuclear Complex (Pentaammineruthenium).m.-Cyanopentacyanoferrate ($^{1-}$). *Inorg. Chem.* **1988**, *27*, 1611-1614.

(60) Vance, F. W.; Karki, L.; Reigle, J. K.; Hupp, J. T.; Ratner, M. A. Aspects of Intervalence Charge Transfer in Cyanide-Bridged Systems: Modulated Electric Field Assessment of Distances, Polarizability Changes, and Anticipated First Hyperpolarizability Characteristics. *J. Phys. Chem. A* **1998**, *102*, 8320-8324.

3.A.1. Difference densities for Ru model complexes

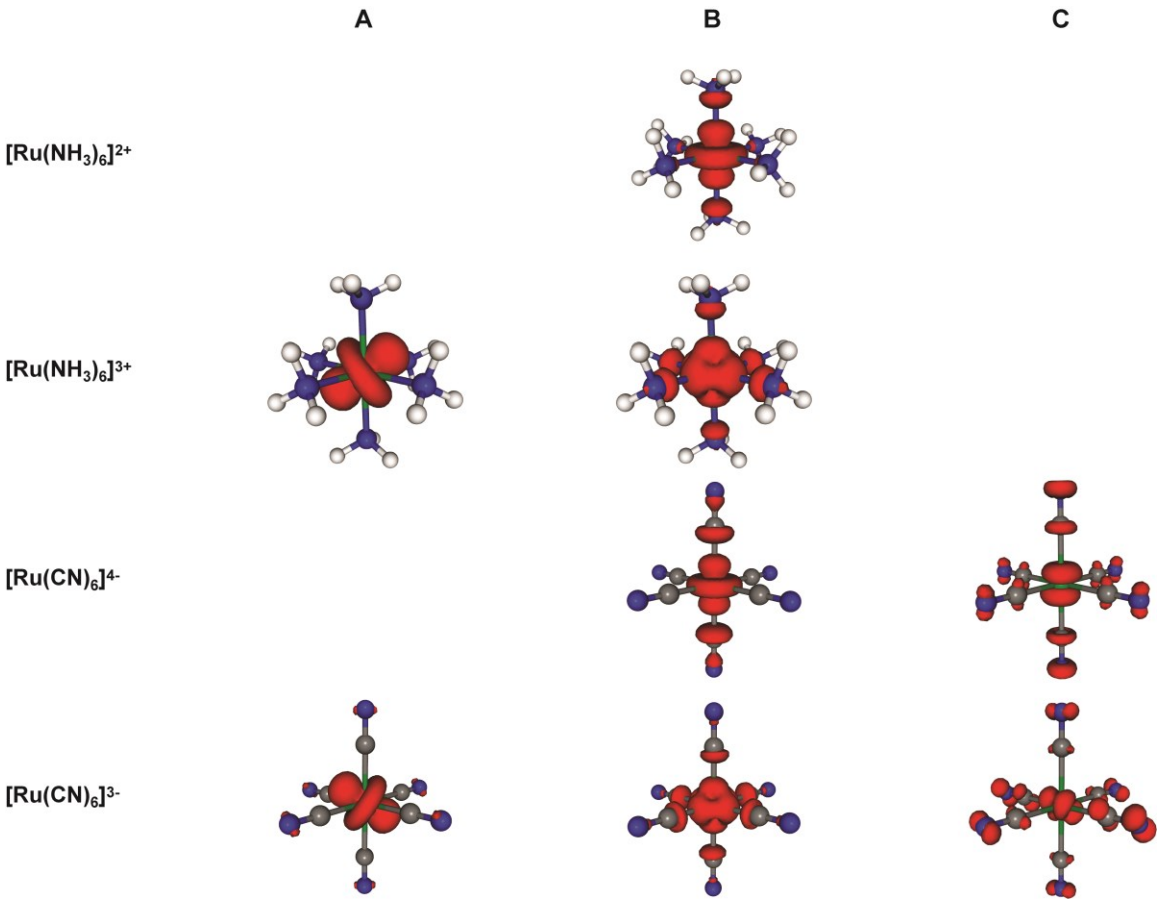

Figure 3.A.1. Difference densities are plotted for features A, B, and C present in the spectra of each of the Ru complexes. All surfaces are plotted with an isovalues of 0.005.

The difference densities allow us to interpret each of the spectral features in Ru L-edge XAS at a molecular level. For example, $[Ru(NH_3)_6]^{3+}$ contains two near-edge features A and B assigned to Ru $2p \rightarrow t_{2g}$ and $2p \rightarrow e_g$ transitions, respectively by ligand field considerations. This interpretation agrees well with the DFT results where the difference density associated with A

feature has nonbonding Ru d character indicative of transitions to t_{2g} orbitals. Similarly, the difference density for the B feature has Ru d character that is distributed along the metal–ligand bonding axes, so it is assigned to the $2p \rightarrow e_g$ transition. Complexes that contain strong π-back bonding ligands exhibit an additional feature labeled C. The difference densities for $[Ru(CN)_6]^{4-}$ confirm that feature C involves a transition to orbitals that are a mixture of CN^- π* and Ru d orbitals.

3.A.2. Structures of mixed-valence metal dimers

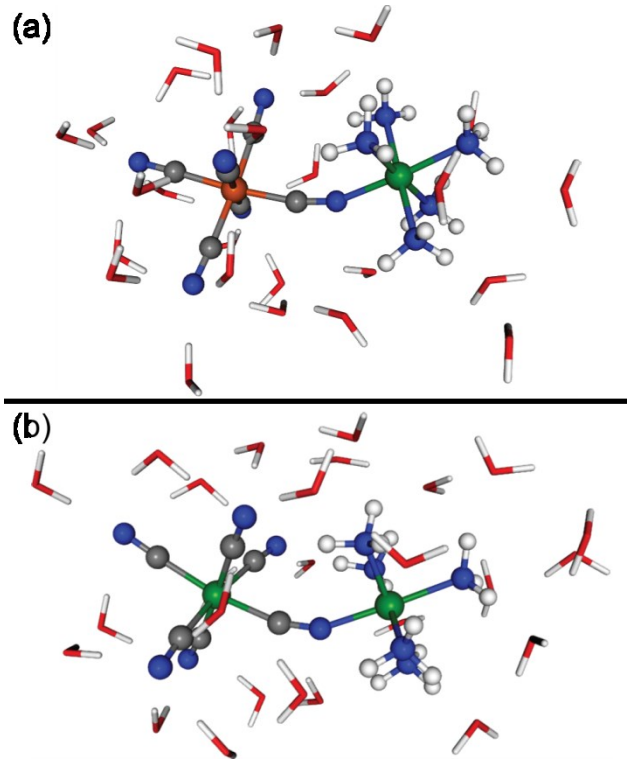

Figure 3.A.2. Structures of mixed-valence transition metal dimers (a) $Fe^{II}Ru^{III}$ and (b) $Ru^{II}Ru^{III}$ including the closest water molecules comprising the "shell" models.

3.A.3. Cartesian coordinates for mixed-valence metal dimers with surrounding water molecules

FeRu Geometry

Fe	-0.233	-0.191	-1.956
C	-0.460	-0.307	-0.082
N	-0.370	-0.321	1.091
C	-0.541	-2.013	-2.205
N	-0.623	-3.168	-2.419
C	-2.013	0.245	-2.398
N	-3.100	0.553	-2.731
C	0.104	1.644	-1.712
N	0.231	2.793	-1.509
C	1.558	-0.627	-1.626
N	2.677	-0.955	-1.475
C	0.165	-0.087	-3.798
N	0.383	-0.099	-4.954
Ru	0.437	0.078	2.880
N	1.411	0.527	4.721
H	1.923	-0.289	5.072
H	2.085	1.289	4.629
H	0.789	0.815	5.493
N	-0.192	-1.746	3.755
H	-0.773	-2.301	3.112
H	0.601	-2.319	4.065
H	-0.782	-1.583	4.579
N	1.067	1.945	2.088
H	2.089	2.055	2.057
H	0.727	2.095	1.136
H	0.686	2.709	2.661
N	2.281	-0.807	2.284
H	2.562	-1.564	2.913
H	2.219	-1.205	1.345
H	3.043	-0.117	2.259
N	-1.350	0.993	3.505
H	-1.767	0.519	4.318
H	-1.170	1.966	3.780
H	-2.065	0.997	2.766

```
O  -2.953 -3.547 -0.938
H  -2.102 -3.452 -1.455
H  -3.719 -3.645 -1.573
O  -2.307 -0.708  5.585
H  -2.125 -0.902  6.549
H  -2.969 -1.368  5.231
O  -3.745  2.031  6.078
H  -3.480  1.067  6.092
H  -4.742  2.104  6.099
O  -0.188  3.483  4.066
H  -1.008  4.024  4.252
H   0.610  3.944  4.454
O   3.954  1.662  1.985
H   4.182  1.537  1.020
H   4.573  2.335  2.390
O   0.757  5.078 -0.042
H   0.650  5.849 -0.669
H   0.605  4.222 -0.537
O   4.280  1.215 -0.708
H   3.789  0.392 -0.994
H   3.863  2.018 -1.132
O   3.362 -3.050  0.064
H   3.998 -2.775  0.785
H   3.160 -2.264 -0.521
O  -1.743 -5.540 -3.217
H  -1.319 -4.709 -2.855
H  -2.034 -5.382 -4.161
O  -3.024  3.053 -4.263
H  -3.076  2.146 -3.846
H  -2.267  3.564 -3.856
O  -3.603  0.890  1.723
H  -4.329  0.490  2.282
H  -3.500  0.361  0.881
O  -2.672  2.890 -1.092
H  -2.986  2.066 -1.564
H  -1.674  2.932 -1.123
O  -2.334 -2.783  2.112
H  -2.453 -3.726  1.802
H  -2.319 -2.170  1.322
O  -5.847  0.732 -2.555
H  -4.868  0.584 -2.696
H  -5.984  1.564 -2.017
O  -0.254 -3.114 -5.141
H  -0.452 -3.163 -4.162
H  -0.045 -2.169 -5.393
O  -0.884  4.782 -3.090
```

```
H  -0.470  4.011 -2.606
H  -0.550  5.640 -2.699
O   2.428 -2.490  4.803
H   3.405 -2.300  4.896
H   2.205 -3.338  5.285
O   0.732  2.288 -6.417
H   0.588  1.503 -5.815
H   0.913  3.103 -5.866
O   2.228 -3.389 -3.162
H   1.247 -3.464 -2.984
H   2.611 -2.646 -2.614
O  -3.774 -1.006 -0.358
H  -3.511 -1.957 -0.520
H  -3.603 -0.467 -1.182
O   2.978  3.344 -1.826
H   3.186  3.613 -2.767
H   2.000  3.153 -1.742
O   1.415 -1.319 -7.159
H   1.943 -2.075 -6.771
H   0.999 -0.789 -6.420
O  -2.481 -0.229 -5.437
H  -1.486 -0.132 -5.404
H  -2.855 -0.149 -4.513
O   0.243  0.961  7.316
H   1.050  0.474  7.651
H  -0.583  0.525  7.673
O   0.782 -4.174 -0.224
H   1.702 -3.787 -0.159
H   0.308 -3.778 -1.010
O   3.262 -0.187 -4.112
H   3.168 -0.425 -3.145
H   2.358 -0.162 -4.539
```

$Ru^{II}Ru^{III}$ Geometry

```
Ru  0.330 -0.449  2.164
C   0.424 -0.632  0.197
N   0.343 -0.447 -0.959
C  -0.175 -2.350  2.597
N  -0.483 -3.430  2.960
C   2.247 -0.938  2.365
N   3.384 -1.247  2.410
```

```
C   0.850  1.427  1.798
N   1.189  2.522  1.528
C  -1.612 -0.056  1.764
N  -2.739  0.096  1.453
C   0.231  0.075  4.119
N   0.212  0.463  5.228
Ru -0.311  0.556 -2.589
N  -1.040  1.658 -4.260
H  -1.904  1.248 -4.637
H  -1.256  2.648 -4.085
H  -0.368  1.656 -5.039
N  -0.768 -1.302 -3.506
H  -0.540 -2.086 -2.875
H  -1.767 -1.396 -3.714
H  -0.244 -1.457 -4.373
N   0.166  2.340 -1.578
H  -0.551  3.074 -1.467
H   0.488  2.151 -0.622
H   0.959  2.804 -2.037
N  -2.247  0.565 -1.738
H  -2.840 -0.175 -2.139
H  -2.242  0.411 -0.722
H  -2.741  1.450 -1.914
N   1.675  0.524 -3.342
H   1.742  0.060 -4.254
H   2.074  1.466 -3.450
H   2.309  0.035 -2.692
O   3.327 -1.838  5.112
H   3.372 -1.537  4.160
H   2.428 -2.236  5.294
O   3.970 -2.669  0.107
H   3.215 -3.324  0.089
H   3.914 -2.118  0.940
O   3.836  1.207  0.934
H   3.836  0.364  1.473
H   2.991  1.714  1.106
O  -1.539 -4.630  0.623
H  -1.161 -5.548  0.738
H  -1.327 -4.077  1.429
O  -2.303  1.644  4.053
H  -2.413  1.132  3.201
H  -1.571  1.233  4.597
O  -3.456  3.031 -2.470
H  -4.305  2.747 -2.915
H  -2.955  3.652 -3.072
O  -3.729 -1.629 -2.924
```

```
H  -3.688 -2.327 -2.208
H  -4.577 -1.734 -3.443
O  -3.485  0.434 -5.216
H  -3.747 -0.530 -5.258
H  -4.202  0.955 -4.751
O  -1.930  4.509 -4.187
H  -1.856  5.274 -3.547
H  -2.082  4.860 -5.111
O  -1.111  4.620 -0.458
H  -1.304  4.547  0.520
H  -0.542  5.425 -0.627
O  -3.663  3.027  0.368
H  -3.452  3.210 -0.592
H  -2.821  3.057  0.907
O   2.441 -4.040  2.609
H   1.449 -3.994  2.729
H   2.819 -3.115  2.600
O   0.858  1.477 -6.363
H   1.743  1.904 -6.550
H   0.966  0.483 -6.335
O  -0.314 -3.213 -1.386
H   0.051 -2.395 -0.941
H  -0.717 -3.815 -0.697
O  -5.202 -1.280  0.658
H  -5.475 -2.107  1.149
H  -4.269 -1.030  0.918
O   0.615 -2.592  5.470
H   0.204 -3.012  4.661
H   0.463 -1.604  5.448
O  -1.459  3.583  2.155
H  -1.818  3.077  2.938
H  -0.514  3.306  1.983
O   1.061  3.489  4.165
H   1.191  3.130  3.241
H   0.943  2.729  4.804
O   0.082  4.210 -6.791
H   0.105  3.210 -6.785
H  -0.869  4.521 -6.783
O   2.655  3.237 -2.892
H   2.682  3.723 -2.018
H   2.661  3.899 -3.642
O   1.282  1.655  7.510
H   1.350  2.638  7.339
H   0.799  1.217  6.751
O   3.728 -0.377 -1.450
H   3.780 -1.289 -1.043
```

```
H   3.786  0.314 -0.730
O   2.266  4.185 -0.338
H   1.736  5.030 -0.416
H   1.950  3.665  0.455
O   1.231 -1.187 -5.740
H   0.680 -1.750 -6.356
H   2.013 -1.718 -5.412
O  -3.074 -2.110  3.280
H  -2.187 -2.573  3.290
H  -3.013 -1.285  2.719
O  -3.157  2.451 -7.093
H  -3.063  2.239 -8.066
H  -3.197  1.600 -6.569
```

3A.4 Sample Input File for Ru XAS

```
# B3LYP TD-DFT
! UKS B3LYP def2-TZVP(-f) COSMO(WATER) DKH
! PAL8 GRID4
%maxcore 2800

%tddft
  OrbWin[0] = 2,4,-1,-1
  OrbWin[1] = 2,4,-1,-1
  NRoots 100
  MaxDim 2400
  tda true
  end

%basis
 NewGTO 44
 # New basis sets are continuously in development
 # Obtain an all-electron Gamess Format basis for Ru from:
 # http://sapporo.center.ims.ac.jp/sapporo/Welcome.do
 End
End

* xyz 3 2
  N      -0.014896     -0.024484      2.123539
  Ru     -0.000030      0.000044     -0.000040
  N      -0.023894      2.124344     -0.013846
  N      -2.126552      0.010192      0.023863
  N       0.023990     -2.124206      0.014390
  N       0.014734      0.024629     -2.123682
  N       2.126629     -0.010494     -0.024340
  H      -0.965894     -0.021940      2.512997
  H       0.454350     -0.840218      2.537319
  H      -2.509928      0.852410      0.472308
  H      -2.539308      0.003016     -0.917829
  H      -0.786435     -2.539479     -0.464809
  H       0.848561     -2.535242     -0.441186
  H      -0.451230      0.842284     -2.537406
  H       0.965577      0.018060     -2.513453
  H       2.546935      0.786956     -0.519023
  H       2.539625     -0.006142      0.917257
  H      -0.848277      2.535422      0.442074
  H       0.786480      2.538994      0.465985
  H      -0.448539     -0.795428     -2.537996
  H      -0.006019      2.521020     -0.961621
  H      -2.546991     -0.785830      0.520743
  H       0.006476     -2.520180      0.962463
  H       2.509806     -0.851287     -0.475595
  H       0.444831      0.797559      2.537886
*
```

Chapter 4

Probing the Electronic Structure of a Photoexcited Solar Cell Dye with Transient X-ray Absorption Spectroscopy

This work has previously been published in the following article:

Van Kuiken, B. E.; Huse, N.; Cho, H.; Strader, M. L.; Lynch, M. S.; Schoenlein, R. W.; Khalil, M. "Probing the Electronic Structure of a Photoexcited Solar Cell Dye with Transient X-ray Absorption Spectroscopy." *J. Phys. Chem. Lett.* **2012**, *3*, 1695.

ABSTRACT. This study uses transient X-ray absorption (XA) spectroscopy and time-dependent density functional theory (TD-DFT) to directly visualize the charge density around the metal atom and the surrounding ligands following an ultrafast metal-to-ligand charge transfer (MLCT) process in the widely used Ru^{II} solar cell dye, $Ru(dcbpy)_2(NCS)_2$ (termed N3). We measure the Ru L-edge XA spectra of the singlet ground ($^1A_1$) and the transient triplet (^{3}MLCT) excited state of $N3^{4-}$ and perform TD-DFT calculations of 2p core-level excitations which identify a unique spectral signature of the electron density on the NCS π* orbitals. We find that the Ru 2*p*, Ru e_g, and NCS π* orbitals are stabilized by 2.0, 1.0, and 0.6 eV, respectively in the transient ^{3}MLCT state of the dye. These results highlight the role of the NCS ligands in governing the oxidation state of the Ru center.

4.1 Introduction

Metal-to-ligand charge transfer (MLCT) states of transition metal complexes are widely used to harness solar energy in dye sensitized solar cells (DSSCs).[1-5] These electronic excited states are generated because absorption of light causes electron transfer from metal *d* orbitals to π^* orbitals of the surrounding ligands. Visualizing the time-evolving electronic and molecular structure of these fleeting MLCT states is crucial for understanding and controlling fundamental photochemical phenomena and for improving the efficiency of light-harvesting devices. The goal of this study is to map the electron density in the ground and the photoexcited ^{3}MLCT state of one of the most efficient solar cell dyes, $Ru(dcbpy)_2(NCS)_2$ (termed N3), using picosecond Ru L-edge X-ray absorption (XA) spectroscopy and time-dependent density functional theory (TD-DFT).

Time-resolved XA spectroscopy is an ideal probe of local changes in electronic and molecular structure following photoexcitation of a molecule in solution and has been used to study a wide range of chemical phenomena in transition metal systems over the past several years.[6-15] Ruthenium L-edge XA spectroscopy involves excitations of Ru 2*p* core electrons to bound valence states and continuum states above the ionization potential. The Ru 2*p* states are split by core spin-orbit coupling into the $2p_{3/2}$ and $2p_{1/2}$ levels giving rise to two main spectral features termed L_3- and L_2-edges, respectively. The spectra are dominated by dipole allowed transitions from the Ru 2*p* levels to the unoccupied Ru 4*d* orbitals. Time-resolved Ru L-edge XA spectroscopy sheds light on how the time-evolving electron density around the Ru atom dictates the course of ultrafast charge transfer processes in solution.

The N3 dye and similar analogues are integral parts of some of the most successful DSSCs to date. Numerous transient absorption studies have shown that excitation with 400 nm light leads

to the formation of a ^{1}MLCT state which undergoes an ultrafast (<50 fs) inter-system crossing to a metastable ^{3}MLCT state with a lifetime of 59 ns.[16-21] It is well known that the electronic structure of the dye molecule critically influences the performance of DSSCs and quantum chemical calculations have been routinely employed to aid in the engineering of new solar cell dyes.[22-24] In this study, we focus on visualizing the time-evolving local electronic structure of free $N3^{4-}$ in solution.

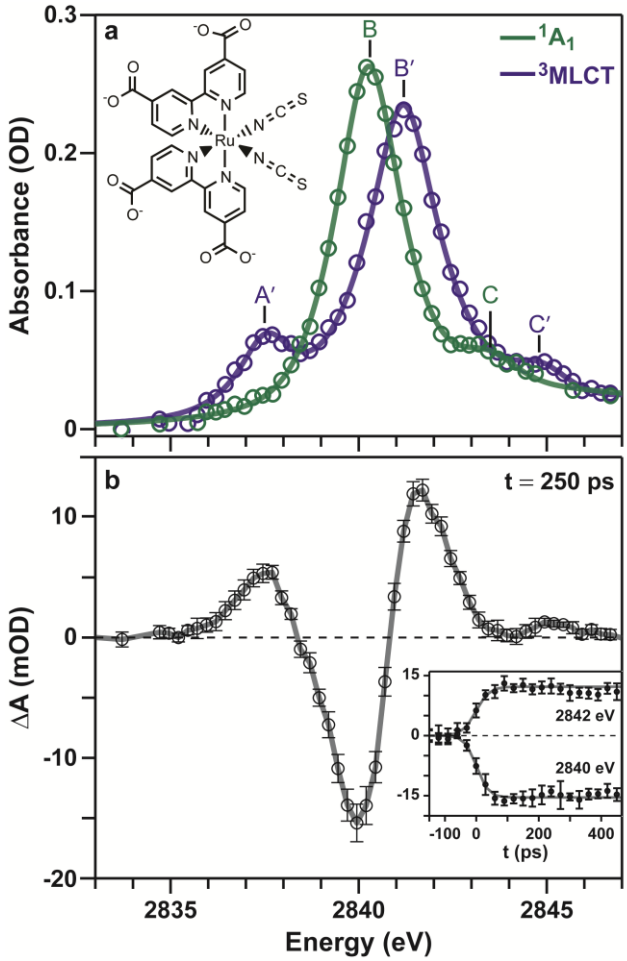

Figure 4.1. (a) Ru L_3-edge XA spectrum of the $^{1}A_1$ ground state (green) and transient ^{3}MLCT excited state (blue) of $[Ru(dcbpy)_2(NCS)_2]^{4-}$ ($N3^{4-}$) where dcbpy= 4,4′-dicarboxylic acid-2,2′-bipyridine in water. The ^{3}MLCT spectrum is constructed from the ground state and the transient difference XA spectrum assuming 18% photoexcitation (see Figure 4.A.2 and associated discussion). The solid line is a fit of the

data to a sum of pseudo-Voigt lineshapes (see Figures 4.A.4 and 4.A.5). The structure of the dye is shown in the inset. (b) The difference XA spectrum at 250 ps following photoexcitation of $N3^{4-}$ with 100 fs 400 nm light pulses. The inset shows the difference XA spectra as a function of pump-probe delay (t) recorded at the specified energies. Grey curves represent sigmoidal fits of the time-resolved XA data revealing an experimental time resolution of ~70 ps given by the X-ray probe pulse width. The error bars correspond to a 95% confidence interval.

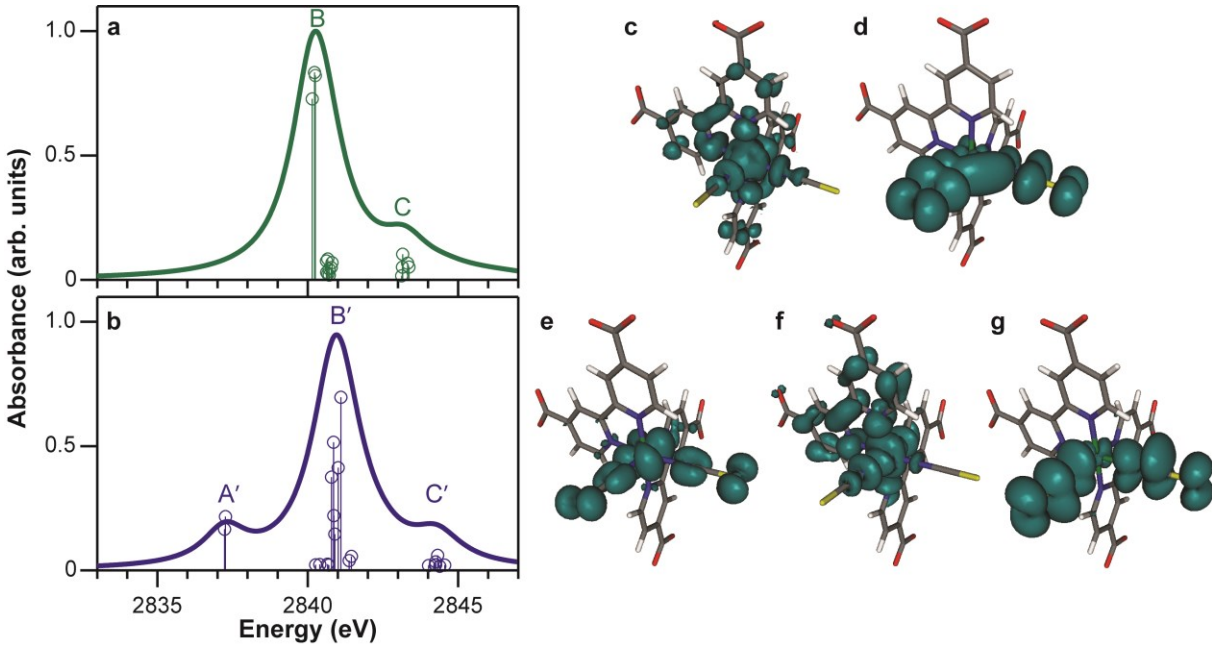

Figure 4.2. TD-DFT simulations of the Ru L_3-edge XA spectra of the (a) ground $^1A_1$ and (b) transient ^{3}MLCT states of $N3^{4-}$. The discrete transitions are displayed as circles for each transition with a non-zero oscillator strength and have been convoluted with a Voigt lineshape consisting of a 1.75 eV Lorentzian width and a 0.4 eV Gaussian broadening to account for the Ru 2p core-hole lifetime and the resolution of the monochrometer, respectively. The calculated spectra are shifted by −2.85 eV to align the feature B of the $^1A_1$ state with the experimental spectrum in Figure 4.1a. (c-g) Positive part of the difference densities are shown for transitions representative of each of the spectral features. The negative portion of the difference density is concentrated at the Ru core and is not visible.

Table 4.1. Peak positions (eV) for peaks in the experimental and calculated XA spectra of the ground and excited state of $N3^{4-}$.[a]

	A(A′)	B(B′)	C(C′)
$^1A_1$		2840.3	2843.5±0.2
$^1A_1$ (DFT)		2840.3	2843.3
^{3}MLCT	2837.5±0.1	2841.3	2844.9±0.2
^{3}MLCT (DFT)	2837.3	2841.0	2844.2

[a] Error bars represent a 95% confidence interval from a least squares fitting of each peak. Only uncertainty values ≥0.1 are listed above.

4.2 Results and Discussion

The Ru L_3-edge XA spectrum of the $^1A_1$ ground state shown in Figure 4.1a reports on $2p_{3/2} \rightarrow 4d$ core transitions and contains two features labeled B and C. The XA difference spectrum in Figure 4.1b encodes the changes in the electronic structure at 250 ps following the ultrafast charge transfer from the Ru atom to a dcbpy ligand with 400 nm light. These changes result in the XA spectrum of the transient ^{3}MLCT state (Figure 4.1a) displaying (i) a new feature A′ at 2837.5 eV, (ii) the main spectral feature B′ shifted to +1.0 eV, and (iii) the feature C′ shifted by +1.4 eV with respect to the ground state. The peak positions of all the spectral features are listed in Table 4.1. The time-evolution of the difference XA spectrum is shown in the inset of Figure 4.1b and confirms that the ^{3}MLCT state of $N3^{4-}$ forms within the 70 ps time resolution of the experiment. The XA spectra of the $^1A_1$ and ^{3}MLCT electronic states of $N3^{4-}$ at the Ru L_2-edge, reporting on $2p_{1/2} \rightarrow 4d$ core transitions, mirror the changes observed at the L_3-edge and are shown in Figure 4A.3 of Appendix 4A.

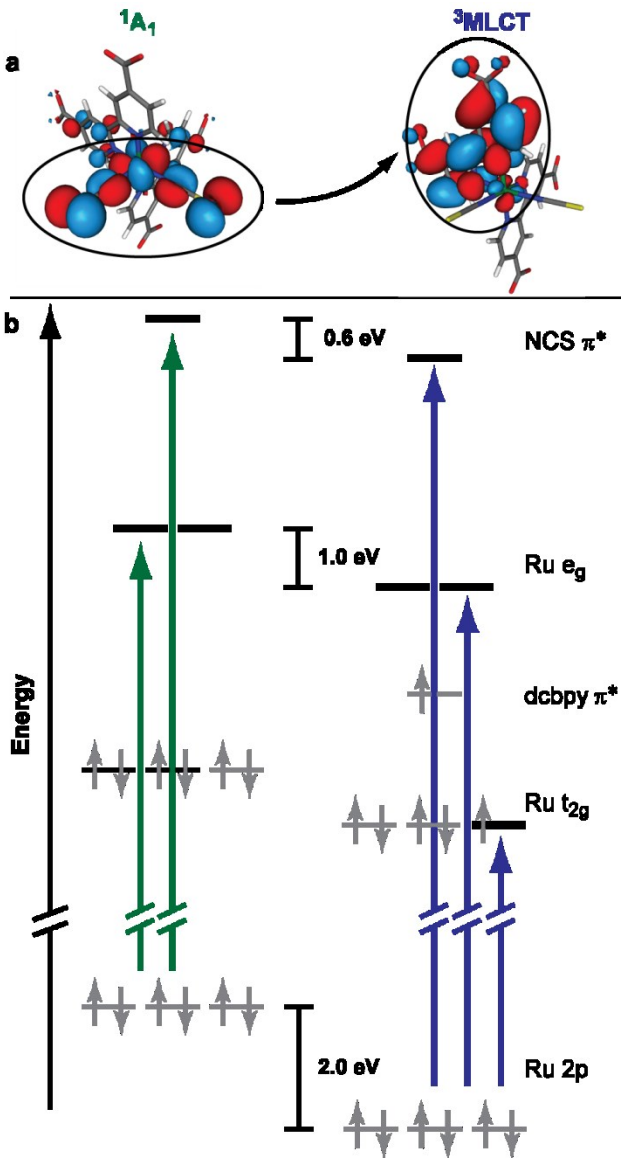

Figure 4.3. Electronic structure of $N3^{4-}$ in its $^1A_1$ (left) and ^{3}MLCT (right) states as revealed by time-resolved Ru L_3-edge XA spectroscopy and quantum chemical calculations. (a) HOMO orbitals of $N3^{4-}$ in the singlet and triplet states. The HOMO in the ground state is a mixture Ru 4*d* and NCS π* orbitals. The HOMO in the triplet state is localized on the one of the dcbpy ligands. (b) Orbital structure of $N3^{4-}$ probed by Ru L_3-edge XA spectroscopy assuming octahedral symmetry. Orbitals that give rise to peaks in the XA spectra are shown in bold with green transitions for the singlet and blue transitions for the triplet state. The energetic shifts in the orbitals derived from time-evolving spectral features are shown in the center column.

The main features in the L-edge XA spectra of d^6 Ru^{II} and d^5 Ru^{III} complexes are commonly

assigned using ligand field theory.[25,26] If we approximate the symmetry of the $N3^{4-}$ molecule as octahedral, the 4*d* orbitals would be split into the familiar triply-degenerate t_{2g} and doubly-degenerate e_g orbitals separated by the ligand-field splitting energy, Δ_o. In the $^1A_1$ ground state, the six electrons assume a low-spin configuration occupying the t_{2g} orbitals. As a result, the peak B in the Ru L_3-edge XA spectrum is assigned to transitions from the $2p_{3/2}$ orbitals to the vacant e_g orbitals. In the ^{3}MLCT state of $N3^{4-}$, one of the Ru 4*d* electrons is transferred to a dcbpy ligand. The resultant transient Ru^{III} d^5 complex has a vacancy in the t_{2g} orbitals and we observe a new low-energy peak A′ which is assigned to $2p \rightarrow t_{2g}$ transitions. The peak B′ is the $2p \rightarrow e_g$ transitions in the ^{3}MLCT state. Based on these assignments, the separation of the A′ and B′ peaks provides a direct measure of a ~3.8 eV ligand-field splitting energy in the ^{3}MLCT state of $N3^{4-}$. The clear pre-edge C(C′) feature has not been discussed extensively in previously published Ru L-edge spectra and does not have a simple "atomic" interpretation as we discuss below.

With the goal of achieving a detailed molecular-level understanding of the MLCT process in $N3^{4-}$, we simulated the Ru L_3-edge XA spectra of the $^1A_1$ and ^{3}MLCT states using TD-DFT as shown in Figure 4.2. TD-DFT calculations were carried out using ORCA and employed the B3LYP functional, the def2-SVP basis set (Sapporo-DK3-TZP for Ru), COSMO for solvation effects, and DKH for scalar relativistic effects.[27-32] Further details are given in 4.A. Each spectral feature in the calculated XA spectrum is comprised of multiple transitions tabulated in Tables 4A.2 and 4A.3. We note that the calculated XA spectra are able to reproduce all the experimentally observed trends in terms of relative peak positions (see Table 4.1), amplitudes and shapes. The *ab initio* calculation of the Ru L_3-edge XA spectrum generates maps of the difference densities for each of the core transitions resulting in the experimentally observed

spectral features. The positive part of the difference densities plotted in Figures 4.2c-g maps the spatial distribution of the core-excited electron for representative transitions. The surfaces plotted in Figures 4.2c and 4.2f show significant electron density at the Ru center and along the metal-ligand bond axes confirming the e_g character of the orbitals contributing to the final state probed by feature B (B′). The difference density in Figure 4.2e reveals that the A′ spectral feature probes the t_{2g} orbitals of the Ru atom which are strongly mixed with the NCS ligand orbitals. Finally, the difference electron densities plotted in Figures 4.2d and 4.2g show that the spectral features C (C′) are direct probes of the NCS π^* orbitals in the ground and excited states of $N3^{4-}$.

The combination of time-resolved XA measurements and TD-DFT simulations of the Ru L_3-edge provide a detailed description of the electronic and molecular structure of $^1A_1$ ground and transient ^{3}MLCT excited states of $N3^{4-}$ as detailed in Figure 4.3. Figure 4.3a shows the highest occupied molecular orbital (HOMO) for the $^1A_1$ and ^{3}MLCT states of $N3^{4-}$. Exciting the $^1A_1$ state with a 400 nm photon depopulates the HOMO orbital containing Ru t_{2g} and NCS π^* character. Following ultrafast intersystem crossing, the excited electron density resides in the HOMO of the ^{3}MLCT state localized on one dcbpy ligand as shown in Figure 4.3a. The ultrafast photoexcitation process leaves a vacancy in the Ru t_{2g} orbitals giving rise to the new peak A′ in the ^{3}MLCT L_3-edge spectrum (Figure 4.1a). A comparison of the difference density plotted in Figure 4.2c and the HOMO of the $^1A_1$ state in Figure 4.3a reveals that the A′ feature is a probe of the HOMO vacated on MLCT excitation. The observation of strong orbital mixing in the HOMO suggests that the ^{3}MLCT state of $N3^{4-}$ is not a pure Ru^{III} state as the MLCT excitation removes electron density from both metal and NCS ligand orbitals. Our TD-DFT results reveal that the molecular orbital contributing most significantly to the intensity of the A′ transition in

the calculated XA spectrum has Mulliken populations of 0.6 and 0.2 for Ru and NCS, respectively (See MO 177β in Figure 4.A.7) and calculated Mulliken charges confirm the loss of electron density on the NCS ligands following the formation of the ^{3}MLCT state (Table 4.A.1). The mixing between the Ru and NCS orbitals observed in this study agrees with photoelectron spectroscopy of the ground state of N3 and confirms previous theoretical predictions.[33-34]

It is important to note that the experimentally measured spectral shifts in features B and C following 400 nm photoexcitation can originate from changes in the binding energies of the 2*p* electrons and/or shifts in the valence orbital energies between the $^1A_1$ ground and transient ^{3}MLCT excited states of $N3^{4-}$. By fitting the absorption edge, we determined that the Ru 2*p* ionization energy increases by 2.0 eV for the ^{3}MLCT state. This agrees well with our DFT calculations where the average orbital energy for Ru 2*p* electrons in the ^{3}MLCT state lies 1.5 eV below its ground state value. The stabilization of the 2*p* orbitals in the triplet state relative to the singlet ground state results from a decrease in shielding concomitant with the decrease in electron density at the Ru atom and is shown schematically in Figure 4.3b.

We measure a +1.0 eV shift in the transition energy of the B (B′) feature following photoexcitation which is attributed to a -2.0 eV shift in the 2*p* core levels and a 1.0 eV decrease in the energy of the Ru e_g orbitals in the ^{3}MLCT state of $N3^{4-}$. The shift in energy of the Ru e_g orbitals is a complex function of electrostatic and geometric factors. The 400 nm MLCT transition removes electron density at the Ru atom decreasing the shielding of the e_g orbitals from the nuclear charge and reducing electron-electron repulsion. While these stabilizing electrostatic effects dominate, the MLCT excitation also results in a 0.04 Å decrease of the average Ru-N_{NCS} distance which should slightly destabilize the Ru e_g orbitals. We measure a +1.4 eV shift in the transition energy of the C (C′) feature following photoexcitation and attribute

it to a 0.6 eV relaxation of the NCS π^* orbitals in the ^{3}MLCT state of $N3^{4-}$ after accounting for the 2*p* core level shift. As discussed earlier, the 400 nm MLCT excitation removes electron density from both metal and NCS ligand orbitals. The subsequent decrease in the anionic character of the NCS ligands stabilizes their π^* orbitals as shown in Figure 4.3b. Our results show how the C (C′) spectral feature in the Ru L_3 edge XA spectrum of $N3^{4-}$ tracks the charge depletion and rearrangement of electron density on the NCS ligands during the MLCT excitation.

It is instructive to compare our time-resolved Ru L_3-edge XA spectroscopy results on the solar cell dye N3 to similar measurements on $[Ru(bpy)_3]^{2+}$ performed by Chergui and co-workers.[35] Notably, the Ru L_3-edge spectra of $[Ru(bpy)_3]^{2+}$ do not show the spectral feature C (C′) which arises from transitions to the π^* orbitals of the NCS ligands in N3. We note that the feature labeled C in Reference 35 is a post-edge feature arising from multiple scattering effects, not to be confused with the pre-edge feature labeled C in Figure 4.1a. The stabilization of the 2*p* core-levels in the ^{3}MLCT state of $[Ru(bpy)_3]^{2+}$ by 1.8 eV is similar to the 2.0 eV value measured for $N3^{4-}$ in this study. Ru L-edge spectroscopy of $[Ru(bpy)_3]^{2+}$ predicted a ~0.03 Å decrease in the Ru-N bond distances for the ^{3}MLCT state. This differs from the case of $N3^{4-}$ where the DFT calculations predict no change in the Ru-N_{dcbpy} bond lengths upon photoexcitation. Recently Zhang et al. performed a complementary time-resolved XA experiment at the Ru K-edge on N3 adsorbed on TiO_2 nanoparticles.[8] They reported a 0.06 Å decrease in the Ru-N_{NCS} bond distances and little change in the Ru-N_{dcbpy} bond distances in the $N3^+$ complex following photoinduced charge injection into TiO_2. Although the ^{3}MLCT state of $N3^{4-}$ probed in our experiment is different from the $N3^+$ complex, the geometry changes upon photoexcitation predicted by our DFT simulations agree closely with the results from the Ru K-edge experiment.

The success of TD-DFT to qualitatively reproduce the equilibrium and transient XA spectra of $N3^{4-}$ in solution builds on recent theoretical studies which have employed methods rooted in Kohn-Sham DFT for simulating Ru L-edge XA spectra.[36,37] The choice of TD-DFT for calculating L-edge XA spectra of second row transition metal complexes requires careful consideration of multiplet and spin-orbit effects and warrants some discussion. The energetic and spatial separation between the 2*p* and 4*d* orbitals of the second row transition metals substantially weakens the *p*-*d* exchange interaction and the L-edge spectra are not dominated by transitions arising from multiplet effects.[38] Campbell *et al.* applied spin-free DFT using the Z+1 approximation to interpret the time-resolved Ru L_3-edge XA spectra of $[Ru(bpy)_3]^{2+}$.[36] More recently, ground state orbitals from two-component relativistic calculations were used to construct initial and core-excited states by Koopman-style excitations to simulate and interpret the $L_{2,3}$-edges for several Ru^{II} and Ru^{III} complexes.[37] Both of these approaches were able to reproduce the experimentally observed features suggesting that multiplet effects in Ru $L_{2,3}$-edge spectra are weak. Our simulations also neglect 4*d* spin-orbit coupling, but ligand-field multiplet calculations have shown that inclusion of 4*d* spin-orbit coupling has a very slight effect on peak amplitudes and positions in the Ru L_3-edge spectrum.[39] In the case of the d^5 molecule, $[Ru(NH_3)_6]Cl_3$, 4*d* spin-orbit coupling affects only the partially occupied t_{2g} orbitals shifting the transition energy by +0.13 eV relative to the spin-free value.[25] Since this energy shift is well below the resolution of our experiment, neglect of spin-orbit coupling has little impact on the interpretation of our experimental spectra using TD-DFT simulations. This is evident from the excellent agreement of our experimental and calculated L_3-edge XA spectra (see Figures 4.1a, 4.2a-b and Table 4.1).

4.3 Conclusions

Our ability to design molecules and materials for solar energy capture and conversion relies on the development of new quantitative experimental tools which can track time-evolving electron density at high spatial and temporal resolution. In this study, the combination of ultrafast X-ray absorption spectroscopy and TD-DFT provides a detailed understanding of the time-evolving electron density and molecular structure of the transient ^{3}MLCT state in the widely used solar cell dye molecule, $N3^{4-}$, in solution. In summary, core-level transitions of the Ru 2*p* electrons to the Ru 4*d* orbitals probe the mixing of the metal and the NCS ligand orbitals. Following the 400 nm ultrafast MLCT excitation of $N3^{4-}$, the dye relaxes to a ^{3}MLCT state indicated by the appearance of the A' feature in the XA spectrum. The ultrafast transfer of electron density from the Ru atom and the NCS ligands to one of the dcbpy ligands leads to a 2.0 and 1.0 eV stabilization of the Ru 2*p* and e_g orbitals, respectively. The TD-DFT simulation of the Ru L_3-edge XA spectrum identifies the molecular origin of spectral feature C (C′), which directly tracks the loss of electron density from the NCS ligands during the ultrafast MLCT process. This investigation yields important new insights on the influence of the NCS ligand on charge transfer and dye regeneration efficiencies in DSSCs. The multi-electron transfer mechanism by which the dye is regenerated with the I^-/I_3 redox couple in a solar cell is still unclear.[40-42] Our results demonstrate that the charge density on the NCS ligands modulates the oxidation state of the N3 dye, which provides a microscopic explanation for the superior efficiency of Ru^{II} dyes containing the NCS ligands. We identify the spectral feature C (C′) in the Ru L-edge XA spectrum as a sensitive NCS ligand specific probe, which can be used to monitor transient structural dynamics of the dye regeneration process and aid in the design and engineering of new DSSCs at the molecular level.

REFERENCES

(1) Grätzel, M. Solar Energy Conversion by Dye-Sensitized Photovoltaic Cells. *Inorg. Chem.* **2005**, *44*, 6841-6851.

(2) Grätzel, M. Recent Advances in Sensitized Mesoscopic Solar Cells. *Acc. Chem. Res.* **2009**, *42*, 1788-1798.

(3) Anderson, N. A.; Lian, T. Ultrafast Electron Transfer at the Molecule-Semiconductor Nanoparticle Interface. *Annu. Rev. Phys. Chem.* **2005**, *56*, 491-519.

(4) Ardo, S.; Meyer, G. J. Photodriven Heterogeneous Charge Transfer with Transition-Metal Compounds Anchored to TiO_2 Semiconductor Surfaces. *Chem. Soc. Rev.* **2009**, *38*, 115-164.

(5) Hagfeldt, A.; Boschloo, G.; Sun, L.; Kloo, L.; Pettersson, H. Dye-Sensitized Solar Cells. *Chem. Rev.* **2010**, *110*, 6595-6663.

(6) Chen, L. X. Probing Transient Molecular Structures in Photochemical Processes Using Laser-Initiated Time-Resolved X-Ray Absorption Spectroscopy. *Annu. Rev. Phys. Chem.* **2005**, *56*, 221-254.

(7) Chen, L. X.; Zhang, X.; Wasinger, E. C.; Lockard, J. V.; Stickrath, A. B.; Mara, M. W.; Attenkofer, K.; Jennings, G.; Smolentsev, G.; Soldatov, A. X-Ray Snapshots for Metalloporphyrin Axial Ligation. *Chem. Sci.* **2010**, *1*, 642-650.

(8) Zhang, X.-Y.; Smolentsev, G.; Guo, J.-C.; Attenkofer, K.; Kurtz, C.; Jennings, G.; Lockard, J. V.; Stickrath, A. B.; Chen, L.-X. Visualizing Interfacial Charge Transfer in Ru-Dye-Sensitized TiO_2 Nanoparticles Using X-Ray Transient Absorption Spectroscopy. *J. Phys. Chem. Lett.* **2011**, *2*, 628-632.

(9) Chergui, M. Picosecond and Femtosecond X-Ray Absorption Spectroscopy of Molecular Systems. *Acta Crystallogr., Sect. A: Found. Crystallogr.* **2010**, *A66*, 229-239.

(10) Bressler, C.; Chergui, M. Molecular Structural Dynamics Probed by Ultrafast X-Ray Absorption Spectroscopy. *Annu. Rev. Phys. Chem.* **2010**, *61*, 263-282.

(11) Khalil, M.; Marcus, M. A.; Smeigh, A. L.; McCusker, J. K.; Chong, H. H. W.; Schoenlein, R. W. Picosecond X-Ray Absorption Spectroscopy of a Photoinduced Iron(II) Spin Crossover Reaction in Solution. *J. Phys. Chem. A* **2006**, *110*, 38-44.

(12) Huse, N.; Cho, H.; Hong, K.; Jamula, L.; de Groot, F. M. F.; Kim, T. K.; McCusker, J. K.; Schoenlein, R. W. Femtosecond Soft X-Ray Spectroscopy of Solvated Transition-Metal Complexes: Deciphering the Interplay of Electronic and Structural Dynamics. *J. Phys. Chem. Lett.* **2011**, *2*, 880-884.

(13) Huse, N.; Kim, T. K.; Jamula, L.; McCusker, J. K.; de Groot, F. M. F.; Schoenlein, R. W. Photo-Induced Spin-State Conversion in Solvated Transition Metal Complexes Probed Via Time-Resolved Soft X-Ray Spectroscopy. *J. Am. Chem. Soc.* **2010**, *132*, 6809-6816.

(14) Lee, T.; Jiang, Y.; Rose-Petruck, C. G.; Benesch, F. Ultrafast Tabletop Laser-Pump-X-Ray Probe Measurement of Solvated $Fe(CN)_6^{4-}$. *J. Chem. Phys.* **2005**, *122*, 084501-084508.

(15) Chen, J.; Rentzepis, P. M. Evolution of Transient Structures in Solids and Liquids by Means of Time Resolved X-Ray Diffraction and X-Ray Absorption Fine Structure. *Adv. Multi-Photon Processes Spectrosc.* **2010**, *19*, 117-183.

(16) Benkö, G.; Kallioinen, J.; Korppi-Tommola, J. E. I.; Yartsev, A. P.; Sundström, V. Photoinduced Ultrafast Dye-to-Semiconductor Electron Injection from Nonthermalized and Thermalized Donor States. *J. Am. Chem. Soc.* **2001**, *124*, 489-493.

(17) Asbury, J. B.; Ellingson, R. J.; Ghosh, H. N.; Ferrere, S.; Nozik, A. J.; Lian, T. Femtosecond IR Study of Excited-State Relaxation and Electron-Injection Dynamics of $Ru(dcbpy)_2(NCS)_2$ in Solution and on Nanocrystalline TiO_2 and Al_2O_3 Thin Films. *J. Phys. Chem. B* **1999**, *103*, 3110-3119.

(18) Tachibana, Y.; Moser, J. E.; Grätzel, M.; Klug, D. R.; Durrant, J. R. Subpicosecond Interfacial Charge Separation in Dye-Sensitized Nanocrystalline Titanium Dioxide Films. *J. Phys. Chem.* **1996**, *100*, 20056-20062.

(19) Bräm, O.; Messina, F.; El-Zohry, A. M.; Cannizzo, A.; Chergui, M. Polychromatic Femtosecond Fluorescence Studies of Metal–Polypyridine Complexes in Solution. *Chem. Phys.* **2012**, *393*, 51-57.

(20) Bhasikuttan, A. C.; Okada, T. Excited-State Relaxation Dynamics of $Ru(dcbpy)_2(NCS)_2$, Studied by Fluorescence Upconversion Spectroscopy. *J. Phys. Chem. B* **2004**, *108*, 12629-12632.

(21) Nazeeruddin, M. K.; Kay, A.; Rodicio, I.; Humphry-Baker, R.; Mueller, E.; Liska, P.; Vlachopoulos, N.; Graetzel, M. Conversion of Light to Electricity by Cis-X2bis(2,2'-Bipyridyl-4,4'-Dicarboxylate)Ruthenium(II) Charge-Transfer Sensitizers (X = Cl^-, Br^-, I^-, CN^-, and SCN^-) on Nanocrystalline Titanium Dioxide Electrodes. *J. Amer. Chem. Soc.* **1993**, *115*, 6382-6390.

(22) Fantacci, S.; De, A. F. A Computational Approach to the Electronic and Optical Properties of Ru(II) and Ir(III) Polypyridyl Complexes: Applications to DSC, OLED and NLO. *Coord. Chem. Rev.* **2011**, *255*, 2704-2726.

(23) Barolo, C.; Nazeeruddin, M. K.; Fantacci, S.; Di, C. D.; Comte, P.; Liska, P.; Viscardi, G.; Quagliotto, P.; De, A. F.; Ito, S.et al. Synthesis, Characterization, and DFT-TDDFT Computational Study of a Ruthenium Complex Containing a Functionalized Tetradentate Ligand. *Inorg. Chem.* **2006**, *45*, 4642-4653.

(24) Nazeeruddin, M. K.; De Angelis, F.; Fantacci, S.; Selloni, A.; Viscardi, G.; Liska, P.; Ito, S.; Takeru, B.; Graetzel, M. Combined Experimental and DFT-TDDFT Computational Study of Photoelectrochemical Cell Ruthenium Sensitizers. *J. Amer. Chem. Soc.* **2005**, *127*, 16835-16847.

(25) Sham, T. K. X-Ray Absorption Spectra of Ruthenium L Edges in Hexaammineruthenium Trichloride. *J. Amer. Chem. Soc.* **1983**, *105*, 2269-2273.

(26) de Groot, F.; Kotani, A. *Core Level Spectroscopy of Solids*; CRC Press: Boca Raton, 2008.

(27) Neese, F. The Orca Program System. *WIREs Comput Mol Sci.* **2012**, *2*, 73-78.

(28) Becke, A. A New Mixing of Hartree-Fock and Local Density Functional Theories. *J. Chem. Phys.* **1993**, *98*, 1372-1377.

(29) Weigend, F.; Ahlrichs, R. Balanced Basis Sets of Split Valence, Triple Zeta Valence and Quadruple Zeta Valence Quality for H to Rn: Design and Assessment of Accuracy. *Phys. Chem. Chem. Phys.* **2005**, *7*, 3297-3305.

(30) Klamt, A.; Schueuermann, G. Cosmo: A New Approach to Dielectric Screening in Solvents with Explicit Expressions for the Screening Energy and Its Gradient. *J. Chem. Soc., Perkin Trans. 2* **1993**, 799-805.

(31) Noro, T.; Sekiya, M.; Koga, T.; Saito, S. L. Relativistic Contracted Gaussian-Type Basis Functions for Atoms K through Xe. *Chem. Phys. Lett.* **2009**, *481*, 229-233.

(32) Neese, F. Calculation of Electric-Field Gradients Based on Higher-Order Generalized Douglas-Kroll Transformations. *J. Chem. Phys.* **2005**, *122*, 204107-204116.

(33) Rensmo, H.; Södergren, S.; Patthey, L.; Westermark, K.; Vayssieres, L.; Kohle, O.; Brühwiler, P. A.; Hagfeldt, A.; Siegbahn, H. The Electronic Structure of the Cis-Bis(4,4′-Dicarboxy-2,2′-Bipyridine)-Bis(Isothiocyanato)Ruthenium(Ii) Complex and Its Ligand 2,2′-

Bipyridyl-4,4′-Dicarboxylic Acid Studied with Electron Spectroscopy. *Chem. Phys. Lett.* **1997**, *274*, 51-57.

(34) De Angelis, F.; Fantacci, S.; Selloni, A. Time-Dependent Density Functional Theory Study of the Absorption Spectrum of [Ru(4,4'-COOH-2,2'-bpy)$_2$(NCS)$_2$] in Water Solution: Influence of the pH. *Chem. Phys. Lett.* **2004**, *389*, 204-208.

(35) Gawelda, W.; Johnson, M.; de, G. F. M. F.; Abela, R.; Bressler, C.; Chergui, M. Electronic and Molecular Structure of Photoexcited [$Ru^{II}(bpy)_3]^{2+}$ Probed by Picosecond X-Ray Absorption Spectroscopy. *J. Am. Chem. Soc.* **2006**, *128*, 5001-5009.

(36) Campbell, L.; Mukamel, S. Simulation of X-Ray Absorption near Edge Spectra of Electronically Excited Ruthenium Tris-2,2'-Bipyridine. *J. Chem. Phys.* **2004**, *121*, 12323-12333.

(37) Alperovich, I.; Smolentsev, G.; Moonshiram, D.; Jurss, J. W.; Concepcion, J. J.; Meyer, T. J.; Soldatov, A.; Pushkar, Y. Understanding the Electronic Structure of 4d Metal Complexes: From Molecular Spinors to L-Edge Spectra of a Di-Ru Catalyst. *J. Amer. Chem. Soc.* **2011**, *133*, 15786-15794.

(38) de Groot, F. High-Resolution X-Ray Emission and X-Ray Absorption Spectroscopy. *Chem. Rev.* **2001**, *101*, 1779-1808.

(39) de Groot, F. M. F. Differences between L_3 and L_2 X-Ray Absorption Spectra of Transition Metal Compounds. *J. Chem. Phys.* **1994**, *101*, 6570-6576.

(40) Nyhlen, J.; Boschloo, G.; Hagfeldt, A.; Kloo, L.; Privalov, T. Regeneration of Oxidized Organic Photo-Sensitizers in Grätzel Solar Cells: Quantum-Chemical Portrait of a General Mechanism. *ChemPhysChem* **2010**, *11*, 1858-1862.

(41) Privalov, T.; Boschloo, G.; Hagfeldt, A.; Svensson, P. H.; Kloo, L. A Study of the Interactions between I^-/I_3^- Redox Mediators and Organometallic Sensitizing Dyes in Solar Cells. *J. Phys. Chem. C* **2008**, *113*, 783-790.

(42) Schiffmann, F.; VandeVondele, J.; Hutter, J.; Urakawa, A.; Wirz, R.; Baiker, A. An Atomistic Picture of the Regeneration Process in Dye Sensitized Solar Cells. *Proc. Nat. Acad. Sci.* **2010**, *107*, 4830-4833.

4.A.1 Materials

The N3 dye was obtained from Sigma-Aldrich and used without further purification. The dye was put in an aqueous 0.3 M NaOH solution (pH ≈ 13) to solvate the initially neutral complex by deprotonating the carboxyl groups and generating $N3^{4-}$. Equilibrium and transient XA spectra at the Ru L-edge were collected with 50 and 80 mM samples, respectively. A sapphire nozzle was used to generate a 50 μm thick sample jet and it was continuously refreshed from a sample reservoir.

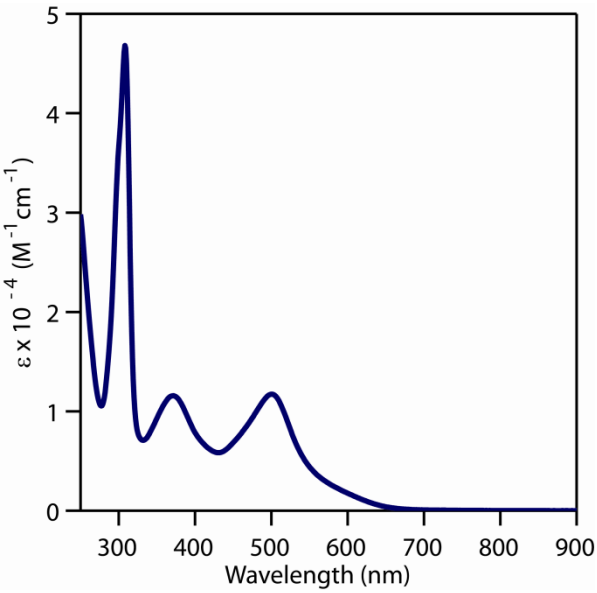

Figure 4.A.1. Visible absorption spectrum of N3 dissolved in basic (pH ~13) aqueous solution.

4.A.2 X-ray Absorption Measurements.

All XA measurements were performed at the ultrafast hard X-ray beamline (6.0.1) at the Advanced Light Source. The experimental setup combines an undulator-based beamline with a femtosecond Ti:Sapphire laser system. The equilibrium and transient XA spectra were obtained by scanning the energy of a monochromatic X-ray beam derived from a double crystal (Si/Ge)

monochrometer (~0.4 eV resolution). All X-ray measurements were performed in transmission mode.

For the transient XA measurements the 100 fs, 400 nm laser pump pulse was obtained by generating the second harmonic of the 800 nm output from a 2 kHz Ti:Sapphire laser system. The 400 nm pump beam was focused to a diameter of 450 μm at the sample with an energy of 150 μJ/pulse. As previously described,[1] the 70 ps X-ray probe pulse is derived from the synchrotron's "camshaft" bunch, which is an electron bunch residing in a 100 ns window. The temporal overlap of the laser and X-ray pulses is experimentally determined to within 20 ps. Spatial overlap of the X-ray and laser pulses is obtained by aligning each beam on a pinhole placed in the sample plane. The difference XA spectrum is constructed by recording the X-ray transmission at 4 kHz. We collect the transmitted X-ray intensity with (I_{ex}) and without 400 nm excitation (I_0). The transient XA spectrum is given by: $\Delta A = -\log_{10}\left(1+\frac{I_{ex}-I_0}{I_0}\right)$. The excited state XA spectrum (A_{ex}) is constructed using the following relation: $A_{ex} = \frac{\Delta A}{f} + A_{gr}$, where A_{gr} is the equilibrium XA spectrum and f is the photoexcitation yield of 18%. The yield was determined by simultaneously fitting the A', B', and C' features of the L_3-edge and the value of the photolysis to the difference spectrum. Figure S2 shows the measured Ru L_3-edge difference spectrum with the fitted difference spectrum generated from $\Delta A = f(A_{ex} - A_{gr})$ with f = 18%. The fitted spectrum faithfully reproduces the measured data within the experimental error bars, and the 95% confidence margin from fitting f was $\pm$1%. Finally, we note that small changes in photoexcitation yield have a noticeable impact on the relative peak intensities but little impact on

peak positions. Changes in *f* of ~3% induce shifts in the features at L_3-edge of ~0.2 eV from values reported in the main text.

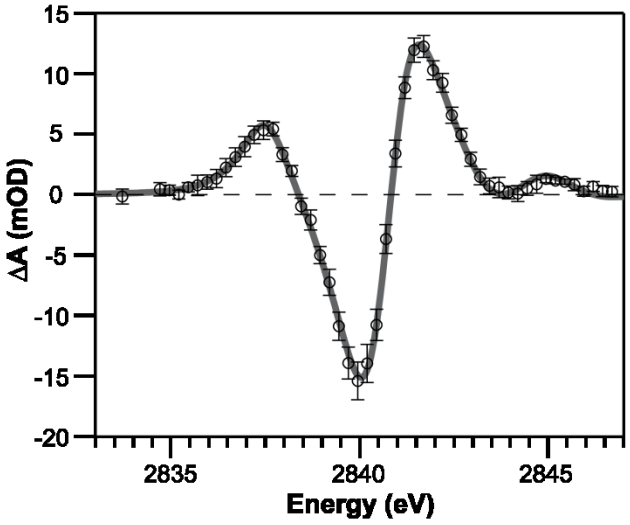

Figure 4.A.2. Comparison of measured (open black circles) and fitted (solid grey line) Ru L_3-edge difference spectrum for photoexcitation yield, *f*, of 18%. The error bars on the measured data represent the 95% confidence interval.

4.A.3 DFT Calculations

The $^1A_1$ ground state and the lowest lying triplet state of $N3^{4-}$ were optimized using density functional theory with the def2-SVP basis set,[3] associated electronic core potential (ECP) for Ru,[4] and the B3LYP exchange—correlation functional.[5] A polarizable continuum model for water was used to stabilize the anions.[6] Frequencies were calculated to verify that structures were at minima on their potential energy surfaces. Optimizations and frequency calculations were performed with Gaussian 09.[7] The TD-DFT calculations were performed with ORCA.[8] The B3LYP functional was used and scalar relativistic effects were taken into account using the second order Douglas-Kroll-Hess (DKH2) method as implemented in ORCA.[9] All atoms except Ru were described by the relativistically contracted SARC basis set derived from the def2-SVP

basis.[10] The Ru atom was described by the all-electron relativistically contracted Sapporo-DK3-TZP basis set.[11] The conductor-like screening model (COSMO) for water was used to stabilize the anions.[12] Excited states were solved by only including trial vectors in the Davidson algorithm that involve single particle excitations from the Ru 2*p* orbitals as described by Debeer and coworkers. The Tamm-Dancoff approximation was used, and 100 (150) excitations were calculated for the singlet (triplet) state.

4.A.4 Transient Ru L_2-edge X-ray absorption spectra of $N3^{4-}$

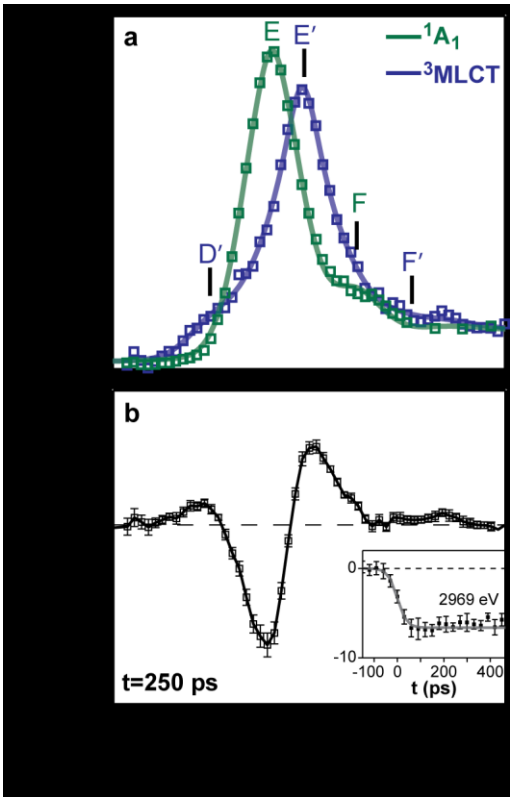

Figure 4.A.3. (a) Ru L_2-edge XA spectrum of the $^1A_1$ ground state (green) and transient ^{3}MLCT excited state (blue) of $N3^{4-}$. The ^{3}MLCT spectrum is constructed from the ground state and the transient difference XA spectrum assuming 20% photoexcitation yield. The solid line is a fit of the data to a sum of pseudo-Voigt lineshapes. The ground state spectrum contains two features labeled E and F at 2868.7 and 2971.7 eV, respectively. The ^{3}MLCT spectrum contains three features labeled D′, E′, and F′ at 2966.4, 2969.8, and 2973.8 eV, respectively. (b) The difference XA spectrum at 250 ps following photoexcitation of $N3^{4-}$ with 400 nm light. The inset shows the difference XA spectra as a function of pump-probe delay (t) recorded at 2969 eV. The error bars correspond to a 95% confidence interval.

4.A.5 Fits of L_3-edge X-ray absorption spectra of $N3^{4-}$

The peak positions from the experimental XA data were extracted by fitting each spectral feature to a sum of a Gaussian and a Lorentzian function. The edge was fit by a sigmoidal function.

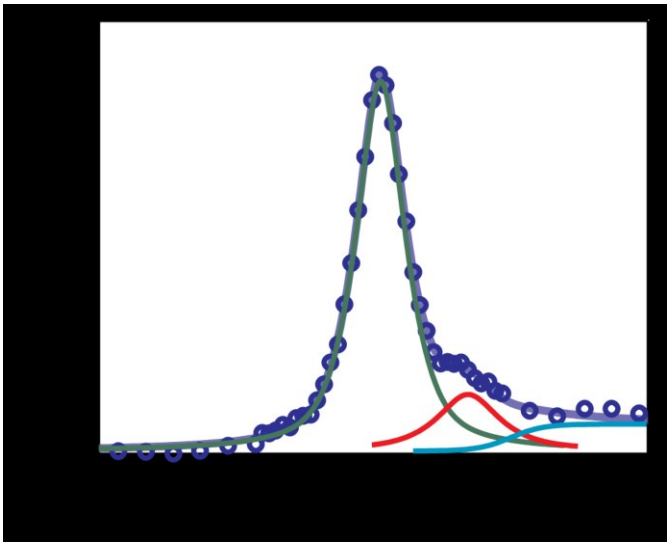

Figure 4.A.4. Ru L_3-edge XA spectrum of the ground $^1A_1$ state of $N3^{4-}$ showing the data in blue circles and the composite fit in a blue solid line. The individual components of the fit are shown as green (2840.3 eV, B), red (2843.5, C), and cyan (2845.0, ionization potential) curves.

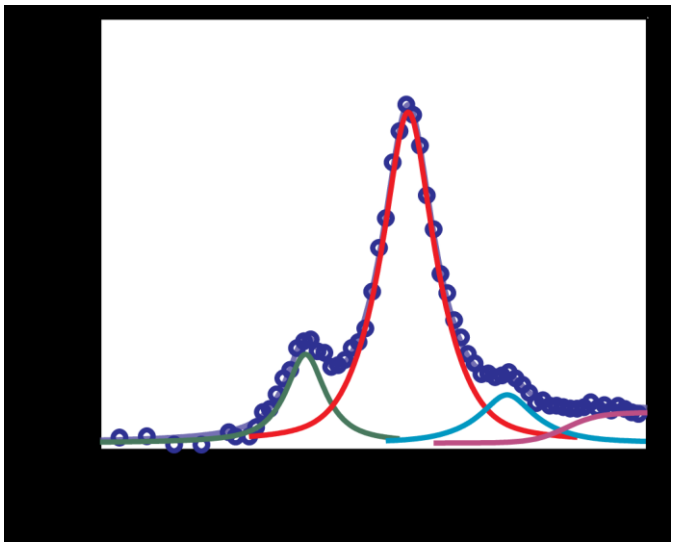

Figure 4.A.5. Ru L_3-edge XA spectrum of the transient ^{3}MLCT excited state of $N3^{4-}$ showing the data in blue circles and the composite fit in a blue solid line. The individual components of

the fit are shown as opaque green (2837.5 eV, A′), red (2841.3 eV, B′), cyan (2844.9 eV, C′), and magenta (2847.0, ionization potential) curves.

4.A.6 Mulliken charges on $N3^{4-}$

Table 4.A.1. Mulliken charges on Ru and each NCS ligand for ground $^1A_1$ state and excited ^{3}MLCT state. The numbering scheme 1 and 2 in the table refers to atoms in the NCS ligands adjacent and opposite to the $(dcbpy)^-$ ligand, respectively in the ^{3}MLCT state.

	$^1A_1$	^{3}MLCT
Ru	0.41	0.51
N (1)	0.02	0.01
C (1)	-0.21	-0.17
S (1)	-0.46	-0.37
N (2)	0.02	0.03
C (2)	-0.20	-0.17
S (2)	-0.46	-0.36

4.A.7 Atomic coordinates (in (Å)) from the geometry optimized structures of $^1A_1$ and ^{3}MLCT states of $N3^{4-}$ used to simulate the XA spectra

B3LYP/def2-SVP $^1A_1$ Ground State

```
C      2.187311   -0.966074    0.922113
C      0.254214   -2.198687    1.345696
C      2.897519   -1.734620    1.850359
C      2.778576    0.152307    0.163713
C      0.910859   -2.988964    2.282486
H     -0.800210   -2.356522    1.115003
C      2.267235   -2.765804    2.548531
```

H	3.952153	-1.551364	2.053815
C	4.112119	0.557464	0.285266
H	0.385886	-3.783987	2.813117
C	2.378806	1.842228	-1.392974
C	4.592876	1.640100	-0.453459
H	4.804451	0.045910	0.953139
C	3.692993	2.289901	-1.307477
H	1.650667	2.318776	-2.051101
H	4.036819	3.139610	-1.898407
C	-2.778422	-0.152158	0.163807
C	-2.378544	-1.843137	-1.391712
C	-4.111955	-0.557299	0.285616
C	-2.187215	0.966730	0.921524
C	-3.692689	-2.290849	-1.305872
H	-1.650395	-2.320056	-2.049551
C	-4.592629	-1.640495	-0.452326
H	-4.804314	-0.045268	0.953087
C	-2.897447	1.735735	1.849388
H	-4.036450	-3.141039	-1.896149
C	-0.254200	2.199750	1.344377
C	-2.267208	2.767355	2.546966
H	-3.952062	1.552576	2.053031
C	-0.910865	2.990498	2.280742
H	0.800190	2.357563	1.113494
H	-0.385947	3.785886	2.810886
N	-0.868403	1.207674	0.670314
N	0.868470	-1.207047	0.671040
N	-1.921518	-0.798272	-0.674967
N	1.921717	0.797907	-0.675490
N	-0.681030	1.292163	-2.224386
C	-1.081428	2.028460	-3.054462
S	-1.626789	3.057829	-4.212385
Ru	0.000028	-0.000133	-0.773394
N	0.680964	-1.293331	-2.223702
C	1.081017	-2.030227	-3.053409
S	1.625906	-3.060455	-4.210792
C	-3.043583	3.625789	3.572261
C	-6.064131	-2.099584	-0.326195
C	3.043550	-3.623774	3.574265
C	6.064425	2.099168	-0.327669
O	6.775367	1.433621	0.459226
O	6.386006	3.086728	-1.025516
O	2.379007	-4.514307	4.149667
O	4.253393	-3.334706	3.717307
O	-6.775098	-1.433554	0.460267
O	-6.385693	-3.087576	-1.023440

```
O      -4.253623    3.337299    3.714813
O      -2.378908    4.516151    4.147773
```

B3LYP/def2-SVP ^{3}MLCT State

C	-2.169391	0.900984	-0.941644
C	-0.175726	1.352763	-2.155490
C	-2.836323	1.883281	-1.720100
C	-2.768691	0.137927	0.104628
C	-0.794016	2.315063	-2.921501
H	0.879193	1.110686	-2.301999
C	-2.181382	2.595853	-2.704003
H	-3.891858	2.099661	-1.552607
C	-4.125829	0.239633	0.514875
H	-0.248895	2.863801	-3.688504
C	-2.430478	-1.534809	1.744538
C	-4.629770	-0.540370	1.536741
H	-4.801066	0.941307	0.024495
C	-3.742587	-1.460095	2.170722
H	-1.723945	-2.228737	2.204618
H	-4.110016	-2.090441	2.979912
C	2.776573	0.140463	-0.125033
C	2.467268	-1.496099	-1.759192
C	4.122933	0.266088	-0.479418
C	2.133627	0.932236	0.942605
C	3.798304	-1.409857	-2.156185
H	1.769469	-2.184611	-2.238168
C	4.655567	-0.513319	-1.508650
H	4.786688	0.964868	0.028557
C	2.796421	1.905278	1.695204
H	4.186476	-2.031050	-2.963991
C	0.146500	1.354187	2.103295
C	2.112900	2.621811	2.680305
H	3.850354	2.132167	1.538423
C	0.757815	2.333007	2.878516
H	-0.905837	1.095740	2.228277
H	0.200466	2.879777	3.639418
N	0.816330	0.667515	1.160465
N	-0.816820	0.644440	-1.191169
N	1.963230	-0.738657	-0.769801
N	-1.930610	-0.764675	0.752128
N	0.673554	-2.212172	1.310344
C	1.092722	-2.963136	2.123517
S	1.655246	-4.001820	3.240204
Ru	-0.003491	-0.840614	-0.026132
N	-0.648473	-2.231963	-1.324342
C	-1.049921	-3.025450	-2.105144
S	-1.585733	-4.121300	-3.178769
C	2.839199	3.701027	3.522094

C	6.144882	-0.383601	-1.912855
C	-2.916664	3.657861	-3.538216
C	-6.100750	-0.423451	1.976332
O	-6.806976	0.408838	1.356258
O	-6.454266	-1.174995	2.917729
O	-2.227434	4.249092	-4.405657
O	-4.132126	3.834103	-3.276102
O	6.810554	0.448583	-1.257334
O	6.515678	-1.124384	-2.849258
O	4.048678	3.869568	3.251207
O	2.134744	4.280282	4.376831

4.A.8 TD-DFT Transitions and Orbital contributions

Table 4.A.2. Transition energies, dipole intensities and unoccupied orbital contributions to core-excited states for the $^1A_1$ state's XA spectrum. Only transitions with dipole intensity greater than 0.05 are listed.

Energy (eV)	Dipole Intensity (arb. units)	MOs contributing to the core-excited state	Contribution (%)
2840.1	0.73	186	69
		187	16
2840.2	0.83	186	29
		187	51
2840.2	0.82	186	20
		187	60
2840.6	0.08	181	82
2840.7	0.08	181	82
2840.8	0.05	183	90
2840.8	0.07	183	86
2843.1	0.05	190	73
		194	15
2843.2	0.10	190	74
		194	13
2843.3	0.07	192	91
2843.4	0.05	192	93

Figure 4.A.6. Molecular orbitals of the $^1A_1$ state which make significant contributions to transitions observed in the XA spectrum at the Ru L_3-edge.

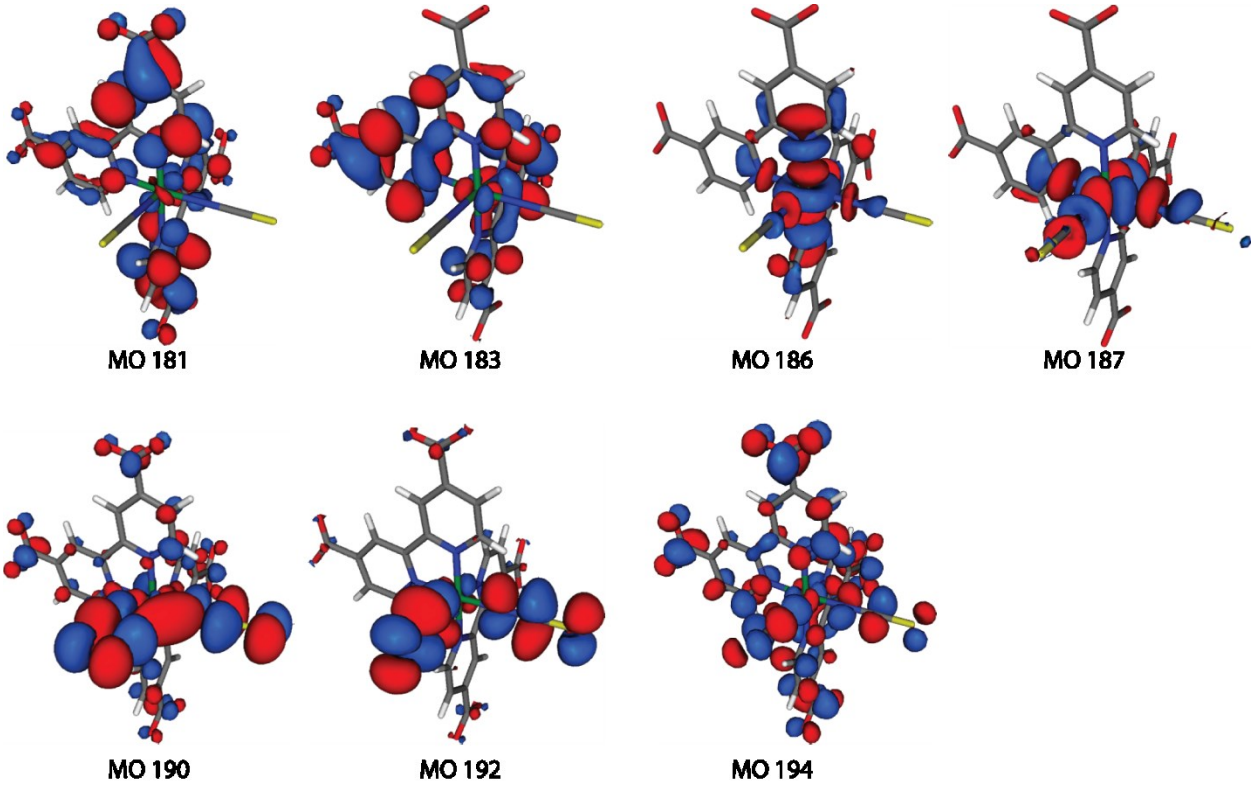

Table 4.A.3. Transition energies, dipole intensities and unoccupied orbital contributions to core-excited states for the ^{3}MLCT state's XA spectrum. Only transitions with dipole intensity greater than 0.05 are listed.

Energy (eV)	Dipole Intensity (arb. units)	MOs contributing to the core-excited state	Contribution (%)
2837.2	0.17	177β	88
2837.3	0.22	177β	86
2840.8	0.37	184α	22
		178β	38
		185β	24
2840.9	0.51	184α	17
		178β	28
		185β	18
		186β	21
2840.9	0.22	179α	45
		178β	22
2840.9	0.15	179α	77
2841.0	0.41	179α	56
		186β	15
2841.1	0.70	179α	22
		185α	21
		186β	30
2841.4	0.06	179β	93
2844.3	0.06	190α	11
		192α	30
		189β	20
		191β	17

Figure 4.A.7. Molecular orbitals of ^{3}MLCT state that make significant contributions to transitions observed in XA spectrum at the Ru L_3-edge.

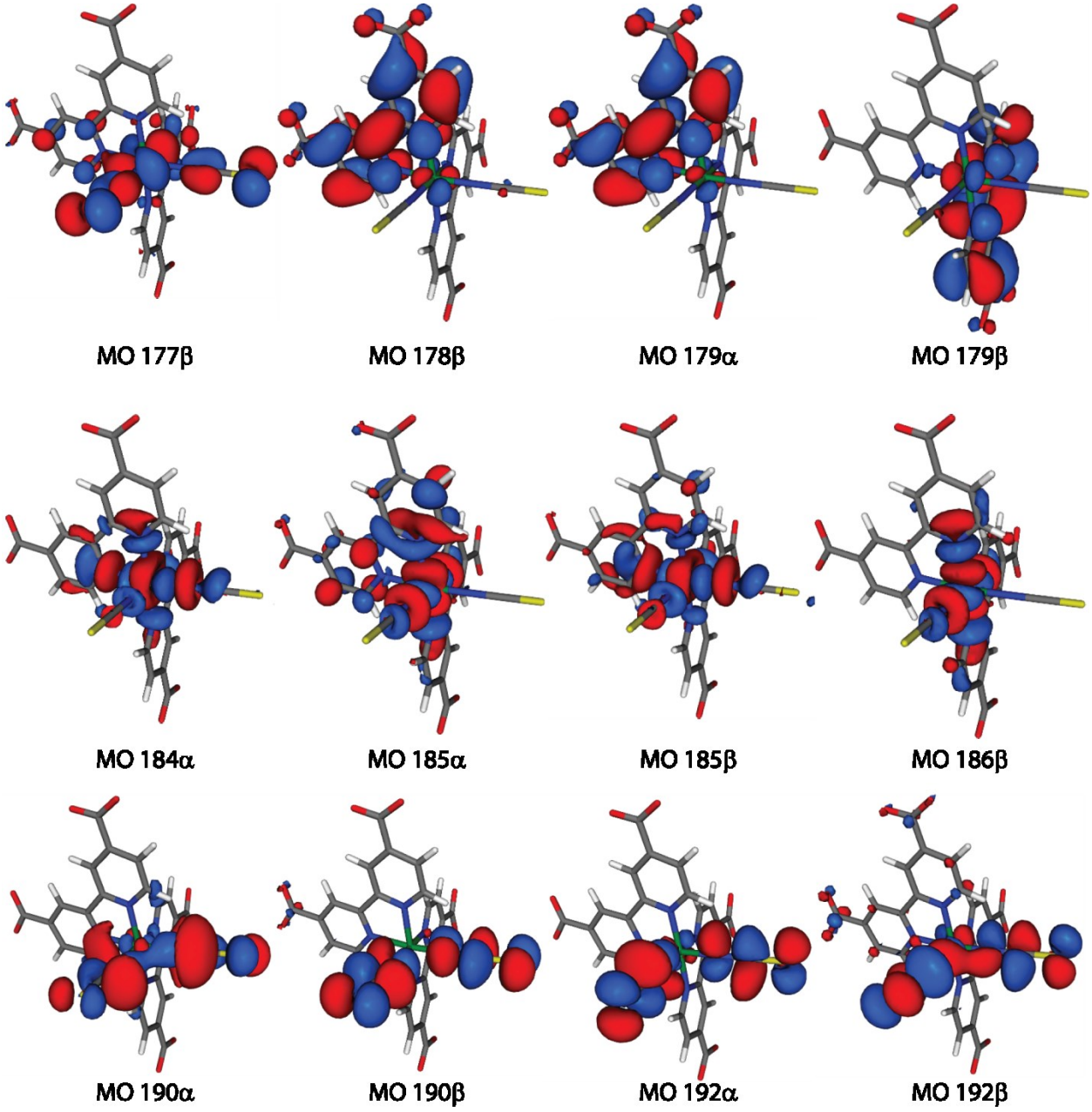

REFERENCES

(1) Huse, N.; Kim, T. K.; Jamula, L.; McCusker, J. K.; de Groot, F. M. F.; Schoenlein, R. W. Photo-Induced Spin-State Conversion in Solvated Transition Metal Complexes Probed Via Time-Resolved Soft X-Ray Spectroscopy. *J. Am. Chem. Soc.* **2010**, *132*, 6809.

(2) Saes, M. Picosecond X-Ray Absorption Spectroscopy : Application to Coordination Chemistry Compounds in Solution, École polytechnique fédérale de Lausanne EPFL, 2004.

(3) Weigend, F.; Ahlrichs, R. Balanced Basis Sets of Split Valence, Triple Zeta Valence and Quadruple Zeta Valence Quality for H to Rn: Design and Assessment of Accuracy. *Phys. Chem. Chem. Phys.* **2005**, *7*, 3297.

(4) Andrae, D.; Häußermann, U.; Dolg, M.; Stoll, H.; Preuß, H. Energy-Adjusted≪I≫Ab Initio Pseudopotentials for the Second and Third Row Transition Elements. *Theoretical Chemistry Accounts: Theory, Computation, and Modeling (Theoretica Chimica Acta)* **1990**, *77*, 123.

(5) Becke, A. A New Mixing of Hartree-Fock and Local Density-Functional Theories. *J. Chem. Phys.* **1993**, *98*, 1372.

(6) Tomasi, J.; Mennucci, B.; Cammi, R. Quantum Mechanical Continuum Solvation Models. *Chem. Rev.* **2005**, *105*, 2999.

(7) Frisch, M. J.; Trucks, G. W.; Schlegel, H. B.; Scuseria, G. E.; Robb, M. A.; Cheeseman, J. R.; Scalmani, G.; Barone, V.; Mennucci, B.; Petersson, G. A.et al. Gaussian 09, Revision B.01. **2009**.

(8) Neese, F. The Orca Program System. *Wiley Interdisciplinary Reviews: Computational Molecular Science* **2012**, *2*, 73.

(9) Neese, F. Calculation of Electric-Field Gradients Based on Higher-Order Generalized Douglas-Kroll Transformations. *J. Chem. Phys.* **2005**, *122*, 204107.

(10) Pantazis, D. A.; Chen, X.-Y.; Landis, C. R.; Neese, F. All-Electron Scalar Relativistic Basis Sets for Third-Row Transition Metal Atoms. *Journal of Chemical Theory and Computation* **2008**, *4*, 908.

(11) Noro, T.; Sekiya, M.; Koga, T.; Saito, S. L. Relativistic Contracted Gaussian-Type Basis Functions for Atoms K through Xe. *Chemical Physics Letters* **2009**, *481*, 229.

(12) Klamt, A.; Schueuermann, G. Cosmo: A New Approach to Dielectric Screening in Solvents with Explicit Expressions for the Screening Energy and Its Gradient. *Journal of the Chemical Society, Perkin Transactions 2: Physical Organic Chemistry (1972-1999)* **1993**, 799.

Chapter 5

Photochemistry of 2-Thiopyridine from Transient Sulfur K-edge X-ray Absorption Spectroscopy

5.1 Introduction

Sulfur containing molecules play a very important role in biological systems, and an understanding of the photochemistry and reactivity is critical for understanding a broad range to biological processes. With the goal of extending transient X-ray absorption (XA) spectroscopy to study the S K-edge, the transient sulfur K-edge XA spectra of 2-thiopyridine (2TP) is reported in this chapter. 2TP has been studied extensively because it exhibits a solvent dependent tautomerism to 2-mercaptopyridine (2MP) shown in Figure 5.1. In nonpolar solvents at low concentrations the 2MP tautomer is dominant, but 2TP is the dominant species in polar solvents such as water.[1-3] We study the photochemistry of 2TP in acetonitrile (ACN).

It has previously been reported that 2TP in H_2O undergoes excited state proton transfer to form 2MP following excitation with 266 nm light.[4] This study used Raman spectroscopy to identify the proton transfer state, but the techniques in this study were not able to identify

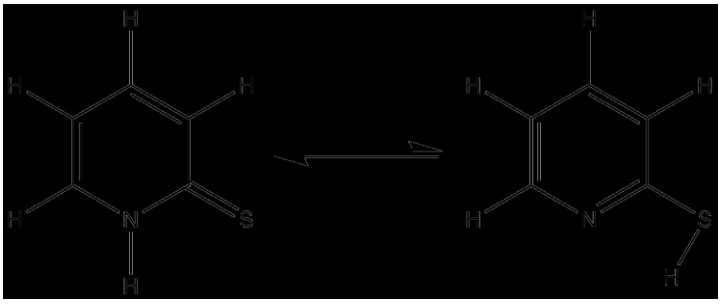

Figure 5.1 The tautomeric equilibrium of 2TP (left) and 2MP (right).

timescales of product formation. Additionally, this study did not consider other photochemical reactions. In a separate study, electron spin resonance (ESR) trapping was used to confirm that radicals were formed upon irradiation of 2TP in H_2O.[5] Given the specificity of X-ray spectroscopy for the bonding environment of the absorbing atom, S K-edge XA measurements are an ideal candidate for exploring the photochemistry of 2TP. Experimental results presented in this chapter show the S K-edge XA spectroscopy is sensitive to the formation of multiple photoproducts following excitation of 2TP with 400 nm light.

5.2 Methods

All chemicals were purchased from Sigma Aldrich and used without further purification. Samples were dissolved in ACN (120 mM) for static and transient measurements. Aqueous samples were prepared at a concentration of 70 mM. The sample was continuously replenished to avoid damage from lasers and X-rays by continuously flowing it using 50 μm sapphire nozzle.

All 2TP All static and transient X-ray absorption spectra were collected at beamline 6.0.1

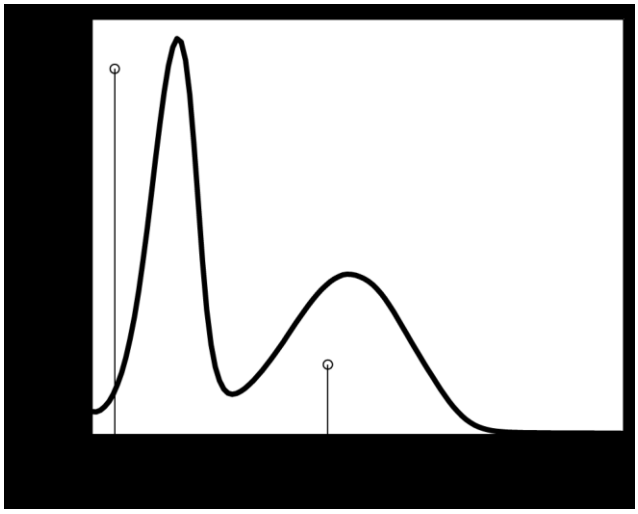

Figure 5.2 Absorption spectrum of 2TP in ACN. Sticks represent bright transitions from the TDDFT simulation of visible spectrum.

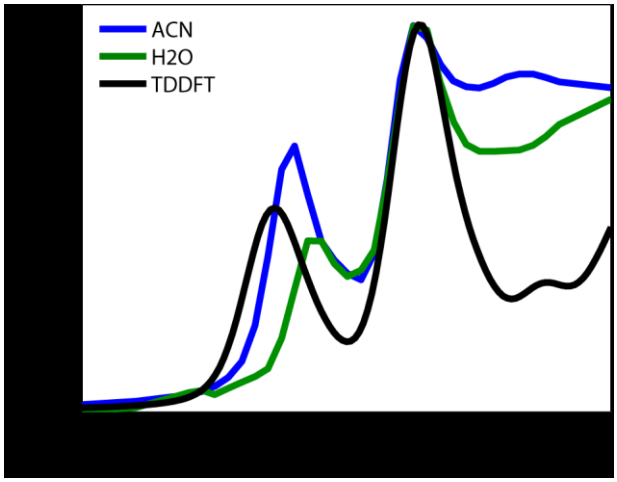

Figure 5.3 Sulfur K-edge XA spectra of 2TP in ACN and H_2O collected as the total fluorescence yield and presented with the TDDFT S K-edge spectrum of 2TP. All spectra have been normalized to 1.0 at the feature that peaks at 2473.4 eV.

at the Advanced Light Source. This beamline combines an undulator-based beamline with a ultrafast Ti:Sapphire laser system. The beamline is equipped with a double crystal Si(111) monochromator which yields ~0.4 eV resolution at the sulfur K-edge. All spectra were calibrated using aqueous sodium thiosulfate where the white line feature was assumed to be located at 2472.02 eV. Static measurements of the sulfur K-edge spectra were collected via total fluorescence yield measurements. Time-resolved measurements were made in transmission mode. All measurements were performed in a helium atmosphere to maximize X-ray flux at the sample.

Transient XA measurements were performed as previously described.[6] Briefly, the 800 nm output of the Ti:Sapphire laser system is frequency doubled to generate the 400 nm "pump" pulse. This is overlapped spatially with the X-ray beam and the delay between the X-rays and lasers . This generates a ~70 ps x-ray probe pulse that defines the time resolution of the experiment. The X-ray intensity is collected at 4 kHz while the laser system operates at 2 kHz.

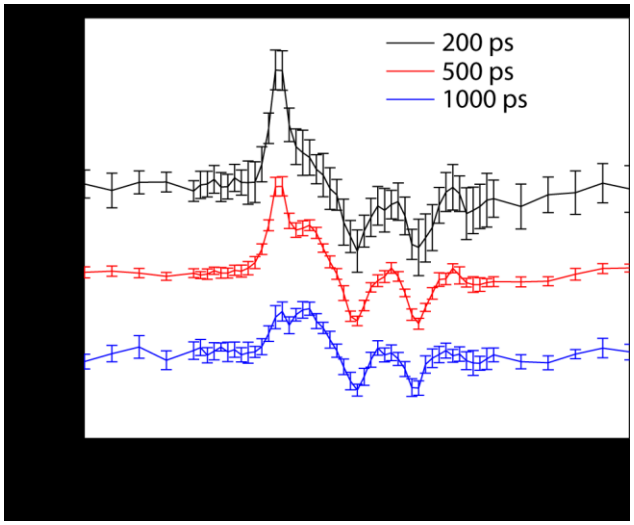

Figure 5.4 Transient XA spectra of 2TP in ACN for pump-probe delay times of 200, 500, and 1000 ps. Error bars show the 95% confidence interval based on the variation in 11 or more independently measured spectra.

This allows for collection of the X-ray transmission with (I_{on}) and without (I_{off}) laser excitation of the sample. The final XA difference spectrum is produced as $\Delta A = -\mathrm{Log}_{10}\left(1 + \frac{I_{on} - I_{off}}{I_{off}}\right)$.

All quantum chemical calculations utilized the density functional formalism. For both 2TP and 2MP singlet and triplet states were optimized using the B3LYP[7,8] functional and the def2-TZVP(-f) basis set. Frequencies were calculated for all structure to confirm that minima had been found. All calculations employed the COSMO model (ε = 36.6, n = 1.344) to mimic the effects of the acetonitrile solvent.[9] Spectra were simulated using the linear response formalism of time-dependent density functional theory (TDDFT). In order to calculate the X-ray spectra, the restricted energy window (REW) TDDFT approach was used to only allow excitations from the sulfur 1s orbitals to the unoccupied space.[10] For spectral simulations the zero-order regular approximation was used to account for scalar relativistic effects. The ORCA quantum chemistry program was used for all calculations.[11]

5.3 Results and Discussion

Given the long history of the solvent dependence of the tautomeric equilibrium for 2-mercaptopyridine, 2-oxypyridine and related molecules, it is necessary The UV-Vis spectrum of 2TP shown in Figure 5.2 exhibits two features that have maxima at 370 nm and 290 nm. Previous studies on the 2TP/2MP system have identified the feature ~370 nm with the 2TP tautomer, which is the dominant species in polar solvents. The sticks are the predicted wavelengths of the first bright transitions transition predicted by TDDFT. While the calculated transitions overestimate the excitation energies, intensities and splittings are well reproduced. These transitions correspond to the HOMO → LUMO and HOMO → LUMO+1. The transient S K-edge measurements discussed below utilize a 400 nm "pump" to excite 2TP in ACN. This wavelength resides on the low energy shoulder of the visible spectrum, but there is still

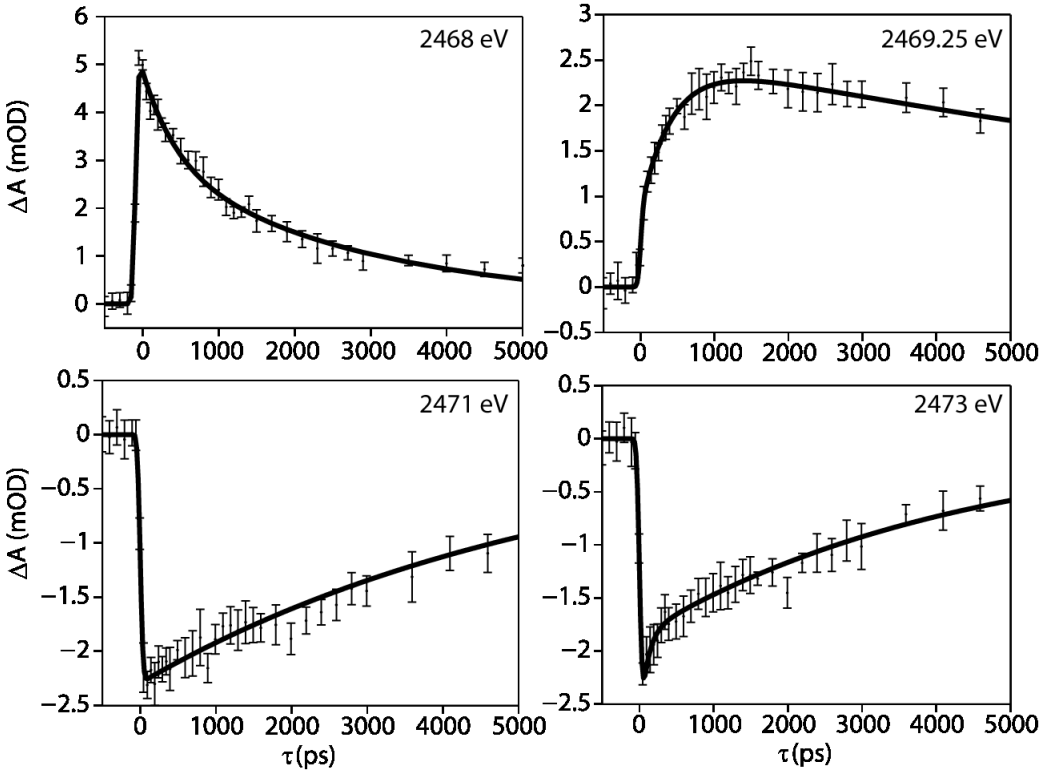

Figure 5.5 Timescans of 2TP at indicated energies. Experimental data has been fit to exponential functions convoluted with Gaussians to account for the instrument response time of our spectrometer.

appreciable absorbance at this wavelength with an optical density ~7000 cm^{-1} M^{-1}.

In Figure 5.3, we present the equilibrium S K-edge of XA spectrum of 2TP measured in ACN and H_2O along with the simulated spectrum. In both solvents the S K-edge exhibits two feature prior to the shape resonances that exist above 2474 eV. The first feature in the 2TP static spectra reach is a maximum at 2472.0 and 2472.4 eV in ACN and H_20, respectively. The second feature appears at the same energy of 2473.4 eV in both solvents. The similarity in the number and relative amplitudes of features in the spectra provide additional evidence that the molecule exists in the 2TP form in both ACN and H_2O. The differences in energy and peak amplitude of the first feature suggests that specific solute—solvent interactions play a role in modulating the energetics of the frontier orbitals of 2TP in solution. The 2TP spectrum simulated by TDDFT is also presented. The TDDFT spectrum has been shifted by +40.9 eV to align the maximum of the experimental spectrum with the simulation. Despite overestimating the splitting between the two spectral features, the calculated result reproduces all spectral features with reasonable peak amplitude ratios.

The time resolved S K-edge spectrum of 2TP in ACN is shown in Figure 5.4 for waiting times of 200, 500, and 1000 ps. The spectra exhibit 4 distinct transient features located at 2468,

Table 5.1 Parameters for biexponential fits of the time dependent change in absorbance of 2TP in ACN. Fit functions consist of two exponentials convoluted with a Gaussian function with width of 70 ps accounting for the experimental response.

Energy (eV)	A_1	$\tau_{1\ (ps)}$	A_2	$\tau_{2\ (ps)}$
2468	0.0028 ± 0.0007	2832 ± 837	0.0023 ± 0.0007	441 ± 223
2469.25	-0.0017 ± 0.0002	432 ± 100	0.0026 ± 0.0002	14778 ± 4628
2471	-0.0023 ± 0	5629 ± 579		
2473	-0.0017 ± 0	4317 ± 536	-0.0009 ± 0.0003	97 ± 59

2469.25, 2471, and 2473 eV. The two higher energy features correspond to a bleaching of the ground state absorbance while the higher energy features provide the signatures of excited state species. Comparing the difference spectra at different waiting times makes it clear that components of the difference spectrum are growing in decaying at different rates. At 200 ps the feature at 2469.25 eV is only visible as a shoulder of the feature at 2468 eV, but at 1000 ps its magnitude equals that of the initially intense feature at 2468 eV.

To further investigate the excited state dynamics in 2TP the time dependence of the transient absorption signal is plotted in Figure 5.4. Time scans have been measured for each feature identified in the difference spectra. The data has been fit to a single exponential or biexponential. In each case the exponential functions have been convoluted with a Gaussian to account for the 70 ps time resolution of the instrument according to the procedure previously utilized by our group.[12] The coefficients and time constants for each of the fits are listed in Table 5.1. For the time traces at 2468, 2471, and 2473 eV the transient absorption signal reaches is maximum within the time resolution of the experiment. Moreover, these transients decay within a few (3-6) nanoseconds. The time trace at 2469.25 eV exhibits different character. It grows in the timescale of ~400 ps, and it has a significantly longer lifetime (~15 ns) than the other transient signals. The different timescales for the dynamics of the four features clearly signify that multiple photoproducts are being formed.

5.4 Summary

Transient S K-edge XA spectra of 2TP have been measured revealing multiple transient species that evolve on distribution of timescales. Full characterization of these transient species will be accomplished using TDDFT to simulate each possible photoproduct. In addition to the

possibility of excited state proton transfer, a range of oxidation products will be considered. This study highlights the sensitivity of XA spectroscopy in being able to distinguish between multiple transients. To the best of my knowledge this constitutes the first successful transient S K-edge XA measurement. Accessing the sulfur K-edge by with time-resolved spectroscopy should allow spectroscopists to access a more of chemically and biological important systems.

References

(1) Beak, P. *Acc. Chem. Res.* **1977**, *10*, 186.

(2) Beak, P.; Covington, J. B.; Smith, S. G. *J. Am. Chem. Soc.* **1976**, *98*, 8284.

(3) Moran, D.; Sukcharoenphon, K.; Puchta, R.; Schaefer, H. F.; Schleyer, P. v. R.; Hoff, C. D. *J. Org. Chem.* **2002**, *67*, 9061.

(4) Du, R.; Liu, C.; Zhao, Y.; Pei, K.-M.; Wang, H.-G.; Zheng, X.; Li, M.; Xue, J.-D.; Phillips, D. L. *J. Phys. Chem. B* **2011**, *115*, 8266.

(5) Reszka, K. J.; Chignell, C. F. *Photochem. Photobiol.* **1994**, *60*, 442.

(6) Van Kuiken, B. E.; Huse, N.; Cho, H.; Strader, M. L.; Lynch, M. S.; Schoenlein, R. W.; Khalil, M. *J. Phys. Chem. Lett.* **2012**, *3*, 1695.

(7) Becke, A. *J. Chem. Phys.* **1993**, *98*, 1372.

(8) Stephens, P. J.; Devlin, F. J.; Chabalowski, C. F.; Frisch, M. J. *J. Phys. Chem.* **1994**, *98*, 11623.

(9) Klamt, A.; Schuurmann, G. *Journal of the Chemical Society-Perkin Transactions 2* **1993**, 799.

(10) Lopata, K.; Van Kuiken, B. E.; Khalil, M.; Govind, N. *J. Chem. Theory Comput.* **2012**.

(11) Neese, F. *Wiley Interdisciplinary Reviews: Computational Molecular Science* **2012**, *2*, 73.

(12) Lynch, M. S.; Van Kuiken, B. E.; Daifuku, S. L.; Khalil, M. *J. Phys. Chem. Lett.* **2011**, *2*, 2252.